In Vivo Two-Dimensional NMR Correlation Spectroscopy

by

Robert A. Kraft

B.S. Engineering Physics
Rensselaer Polytechnic Institute, 1992

SUBMITTED TO THE DEPARTMENT OF NUCLEAR ENGINEERING IN PARTIAL FULFILLMENT OF THE REQUIREMENTS FOR THE DEGREE OF

DOCTOR OF PHILOSOPHY IN NUCLEAR ENGINEERING
AT THE
MASSACHUSETTS INSTITUTE OF TECHNOLOGY

FEBRUARY 1999

Signature of Author: _____
Department of Nuclear Engineering
November 17, 1998

Certified by: _____
Daniel S. Williamson
Instructor of Radiology, Harvard Medical School
Thesis Supervisor

Accepted by: _____
Larry Lidsky
Professor of Nuclear Engineering
Chairman, Department Committee for Graduate Students

In Vivo Two-Dimensional NMR Correlation Spectroscopy

Submitted to the Department of Nuclear Engineering
on November 17, 1998 in Partial Fulfillment of the
Requirements for the Degree of Doctor of Philosophy in
Nuclear Engineering

Abstract

The poor resolution of *in-vivo* one-dimensional nuclear magnetic resonance spectroscopy (NMR) has limited its clinical potential. Currently, only the large singlet methyl resonances arising from N-acetyl aspartate (NAA), choline, and creatine are quantitated in a clinical setting. Other metabolites such as myo-inositol, glutamine, glutamate, lactate, and γ-amino butyric acid (GABA) are of clinical interest but quantitation is difficult due to the overlapping resonances and limited spectral resolution.

To improve the spectral resolution and distinguish between overlapping resonances, a series of two-dimensional chemical shift correlation spectroscopy experiments were developed for a 1.5 Tesla clinical imaging magnet. Two-dimensional methods are attractive for *in vivo* spectroscopy due to their ability to unravel overlapping resonances with the second dimension, simplifying the interpretation and quantitation of low field NMR spectra. Two-dimensional experiments acquired with mix-mode line shape negate the advantages of the second dimension. For this reason, a new experiment, REVOLT, was developed to achieve absorptive mode line shape in both dimensions. Absorptive mode experiments were compared to mixed mode experiments with respect to sensitivity, resolution, and water suppression. Detailed theoretical and experimental calculations of the optimum spin lock and radio frequency power deposition were performed. Two-dimensional spectra were acquired from human bone marrow and human brain tissue. The human brain tissue spectra clearly reveal correlations among the coupled spins of NAA, glutamine, glutamate, lactate, GABA, aspartate and myo-inositol obtained from a single experiment of 23 minutes from a volume of 59 mL.

Thesis Supervisor: Daniel S. Williamson
Title: Instructor of Radiology, Harvard Medical School

Acknowledgements

I would like to thank Dr. Thomas Apple for introducing me to NMR at Rensselaer Polytechnic Institute. His enthusiasm for the subject and his unique ability to express that enthusiasm in his teaching is the reason that I chose to pursue NMR as a career.

Three classmates, in particular, have helped me survive MIT: Joelle Dennie, Stead Kiger, and Kent Riley. Their help and encouragement, not only in class, but also in preparation for the qualifiers has been invaluable and will always be remembered.

I would like to thank Dr. John Bernard and Professor Jacquelyn Yanch for preparing me for the qualifiers. Dr. Bernard's qualifier review class, by now, has probably achieved legendary status within the department. I have never understood why Dr. Bernard holds these review sessions. I am only thankful that he does and that he does it so well. Professor Yanch was gracious enough to help me prepare for the oral qualifiers. She once told me that as a professor in the department it was her job to prepare students for the qualifying exam. While this certainly is true, the amount of time and effort she spent in preparing me for the oral qualifiers, as far as I am concerned, was beyond her job description.

I would like to thank Prof. Cory, who through out my career at MIT, continued to teach me about NMR. He was always very patient while answering my questions even when he had to explain the answer to me several times. I would also like to thank him for graciously "adopting" me as one of his own students by helping me with final thesis preparations.

I owe the greatest debt, at least professionally, to my thesis advisor, Dr. Daniel Williamson. Over the last four years he has been a very patient, understanding, and supportive mentor. Without his encouragement, both professionally and personally, I never would have obtained my degree.

I have mentioned the people that have helped me professionally but I never would have achieved my dream with out the love and support of my parents. They were always there to encourage me when I needed it the most. I would also like to thank my wife, who has made many sacrifices. She endured my strange schedule, celebrated my successes, and encouraged me after my failures. She put her dreams on hold so that I could achieve mine and for that I will always be eternally grateful.

As a final comment, I hope that this thesis may someday be used as circumstantial evidence to prove that I am indeed **"a lot smarter than I appear."**

Table of Contents

List of Figures

List of Tables

Chapter 1 : Background

1.1 Significance and Purpose of the Investigation

In vivo proton Nuclear Magnetic Resonance (NMR) spectroscopy, while promising, has failed to achieve wide acceptance as a clinical diagnostic tool as a result of its inherent poor sensitivity and limited resolution. Poor sensitivity and limited resolution have largely restricted quantitation efforts to the large singlet methyl resonances arising from N-acetyl aspartate (NAA), choline, and creatine (1). Other metabolites such as inositol, glutamine, glutamate, lactate, and γ-amino butyric acid (GABA) may also be detected, but quantitation is difficult due to the poor sensitivity, limited spectral resolution, and overlapping resonances (2).

A recent proton NMR study of pediatric brain (3) and an associated commentary (4), point out the difficulty of assigning and quantitating resonances *in vivo*. For instance, two new unassigned resonances in the spectrum of a child with Sanfillipo syndrome were seen but no attempt was made to assign them due to a lack of spectral detail. In addition, the point is made that inositol and glutamate have overlapping chemical shifts at 1.5 Tesla, making a quantitation of either difficult (4). The inability to assign peaks directly in *in vivo* proton NMR spectra, results from the limited chemical shift dispersion at low fields (< 2 Tesla), line broadening due to magnetic field susceptibility, and overlapping chemical shifts. If clinical inroads are to be made with proton NMR spectroscopy, the information contained in the spectra must be increased.

The problem of overlapping resonance was also encountered in high field NMR as larger and more complex molecules were studied. The problem of overlapping resonances was circumvented with three different approaches. The first approach is to increase the main magnetic field, since the chemical shift frequency is directly proportional to the magnetic field strength. The second approach is spectral editing (5). Spectral editing techniques selectively excite and detect only the resonances of interest. The third approach is multi-dimensional NMR spectroscopy, which was introduced by Jeener in 1971 (6). Multi-dimensional NMR spectroscopy creates correlations between

resonances based upon a variety of interactions such as scalar coupling or chemical exchange. These correlations simplify spectral interpretation by providing additional information, which may distinguish overlapping resonances.

In vivo Magnetic Resonance Spectroscopy (MRS), due to its inherent poor sensitivity, is capable of detecting molecules in millimolar concentrations or greater. These molecules, if detected separately, yield simple spectra that are easily interpreted with 1D spectroscopy. However, MRS observes resonances from many molecules simultaneously, yielding a complex overlapping 1D spectrum. The problem of overlapping resonances is further exacerbated by line broadening due to variations in magnetic susceptibility throughout the heterogeneous tissue. In order to circumvent the problem of overlapping resonances and limited resolution, we adapted and extended multi-dimensional high-field NMR spectroscopy techniques to a low field (1.5 Tesla) clinical imaging system.

1.2 Challenges of I*n Vivo* 2D Spectroscopy

The development of multi-dimensional high field NMR spectroscopy techniques on a clinical Magnetic Resonance Imaging (MRI) system presents several challenges:

- acquisition times must remain short to insure a patient's comfort
- water suppression must be implemented to overcome the limited dynamic range of the Analog to Digital converter
- volume localization is necessary to restrict the signal to the volume of interest.

The difficulty of overcoming these challenges is further increased by the limitations imposed by current clinical hardware:

- clinical magnetic field strengths of 1.5 Tesla limit sensitivity
- radio frequency (RF) inhomogeneity results in improper flip angles over the volume of interest
- limited gradient amplitudes and slew rates lead to sensitivity losses as a result of relaxation.

All of these challenges must be addressed while adhering to the Food and Drug Administration's (FDA) guidelines with respect to magnetic field strength, gradient switching time, and radio frequency power deposition.

The amount of time available for *in vivo* multi-dimensional MRS is limited by the patient's ability to remain motionless throughout the exam, which is typically less than an hour. Since an MRS exam will be in addition to a normal MRI exam, the acquisition time available for an MRS exam is expected to be less than half an hour.

Short acquisition times limit the amount of signal averaging. Limitations on signal averaging and the inherent poor sensitivity of MRS require that *in vivo* multi-dimensional MRS experiments be as sensitive as possible. Maximizing the sensitivity per repetition time provides theoretical guidelines as to the type of useful *in vivo* multi-dimensional NMR experiments; for example, **TO**tal **C**orrelation **S**pectroscop**Y** (TOCSY) has the advantage of higher sensitivity compared to **CO**rrelation **S**pectroscop**Y** (COSY) (7). Short acquisition times also limit the use of many of the techniques used in high-field multi-dimensional NMR spectroscopy; for example, phase cycling is commonly used in high-field NMR spectroscopy experiments as a means of eliminating unwanted signals. Extensive phase cycling dramatically increases the overall acquisition time and may result in acquisitions lasting several hours, which is unacceptable for *in vivo* experiments.

Water suppression is absolutely necessary for MRS experiments with the possible exception of lipid spectroscopy of bone marrow and fatty tumors. The concentration of water in tissue is on the order of 110 Molar, while the metabolites of interest exist in millimolar concentrations. Suppressing the water by three orders of magnitude is acceptable for 1D MRS experiments. However, this degree of water suppression is inadequate for 2D MRS experiments. Instabilities during the experiment result in fluctuations in the degree of water suppression. Stability of the water suppression in 1D MRS experiments is not as critical as in 2D MRS since the fluctuations are averaged together. In 2D MRS, however, unstable water suppression results in substantial t_1 noise, which can obscure the cross peaks of interest. For this reason, 2D MRS experiments need to suppress the water by at least four orders of magnitude.

Volume localization is the third and final reason why 2D MRS is difficult to implement on a clinical scanner. While surface coils are often used for volume localization, they have some inherent disadvantages. Large surface coils have poor RF field inhomogeneity that results in a spread of flip angles over the excited volume. Small

surface coils have difficulty exciting volumes of interest deep below the skin's surface. Volume coils are the preferred method for *in vivo* volume localization, since they are able to uniformly excite volumes of interest deep below the skin's surface. However, the use of volume coils introduces a new challenge. Since 2D MRS experiments use a combination of slice selective pulses for volume localization and hard pulses for spin preparation, great care must be taken to avoid the refocusing of unwanted echoes and outer volume signals.

1.3 *In Vivo* 2D Spectroscopy

Many forms of 2D NMR spectroscopy exist, however, currently only proton homonuclear experiments provide the sensitivity and spectral information necessary for *in vivo* applications. There are two approaches to create a chemical shift correlation: in-phase coherence transfer methods, TOCSY, and anti-phase coherence transfer methods, COSY. As previously mentioned, TOCSY has a theoretical sensitivity advantage over COSY. However, a recent publication, has reported observing similar sensitivity for TOCSY and COSY in human bone marrow (8). We will explore this unexpected result in detail in Chapter 2. To help resolve this counter intuitive observation, three pulse sequences will be used: VOSY-HOHAHA and VOSY-COSY, which were published by Brereton et al. (8), and a new sequence, VOLT, **VO**lume **L**ocalized **T**OCSY developed as part of this thesis work. Comparing the sensitivity of these three experiments both *in vitro* and *in vivo* provides an explanation for the counter intuitive observation.

All three of the above experiments rely on gradients to select a specific coherence pathway while simultaneously achieving volume localization. This results in spectra that can only be displayed in magnitude mode, which severely reduces resolution and sensitivity. Chapter 3 presents REVOLT, **RE**focused **V**olume **L**ocalized **T**OCSY, a new pulse sequence developed as part of this thesis. REVOLT relies on in-phase coherence transfer and acquires both coherence pathways while simultaneously achieving volume localization. The acquisition of both coherence pathways allows the spectra to be displayed in absorptive mode, resulting in increased resolution and sensitivity. The

improvement in resolution and sensitivity achieved with REVOLT will be demonstrated both *in vitro* and *in vivo* with spectra obtained from bone marrow brain tissue.

A challenge of in-phase coherence transfer is to keep the RF power deposited into the patient to less than 3 Watts per kilogram of tissue (9). In Chapter 4 we will show both theoretically and empirically that the in-phase coherence transfer method developed in this thesis does not exceed the FDA guidelines for RF power deposition.

The holy grail of proton MRS has been to obtain spectra from cerebral tissue. Cebral tissue and tumors contain a variety of metabolites that have potential clinical significance: N-acetyl aspartate (NAA), choline (Cho), creatine (Cre), glutamine (Gln), glutamate (Glu), lactate (Lac), γ-amino butyric acid (GABA). The resonances arising from the methyl groups on NAA, Cho, and Cre are the easiest to detect *in vivo* and therefore have been the focus of many MRS studies. An excellent literature review of developments and applications of *in vivo* magnetic resonance spectroscopy has been written by Cox (2).

Chapter 2 : Mixed Mode Correlation Spectroscopy

2.1 Introduction

There are two common approaches to 2D chemical shift correlation spectroscopy: COSY (10,11), and TOCSY (12,13). These approaches differ in their method of coherence transfer. COSY uses anti-phase coherence transfer while TOCSY and HOHAHA use in-phase coherence transfer. The method of coherence transfer, whether anti-phase or in-phase, describes the resulting multiplet structure. As recently pointed out (14), the use of in-phase coherence transfer for 2D NMR has significant sensitivity advantages when compared to anti-phase methods. This is due to the propensity for destructive interference of anti-phase multiplets in the presence of line broadening. TOCSY based experiments with their in-phase cross peaks, makes them attractive for *in vivo* studies, since the in-phase multiplets will constructively interfere in the presence of line broadening.

Brereton, et al (8), have recently demonstrated **ST**imulated **E**cho **A**cquisition **M**ode (STEAM) (15) based COSY and HOHAHA experiments and compared their relative sensitivity *in vivo* in human bone marrow. These experiments have been named VOSY-COSY and VOSY-HOHAHA to indicate volume localization, where VOSY is an acronym for **VO**lume **S**pectroscop**Y**. Somewhat unexpectedly, VOSY-COSY performed comparably to VOSY-HOHAHA. As part of this thesis, this counterintuitive result will be shown to result from the apodization function applied to the 2D data sets prior to Fourier transformation (FT) to remove the dispersive line shape contribution. In addition, a new version of **VO**lume **L**ocalized **T**OCSY, VOLT, was developed as part of this thesis that achieves a higher sensitivity than a similarly performed COSY experiment prior to the application of an apodization function.

The VOLT experiment is a modified DRY-STEAM (16) experiment. DRY-STEAM provides a convenient method of volume localization and superior water suppression when compared to STEAM. To improve the water suppression of the

original VOSY-COSY and VOSY-HOHAHA by an order of magnitude, additional water suppression pulses of DRY-STEAM were incorporated into both experiments. An unfortunate side effect of both STEAM and DRY-STEAM is the requirement of acquiring mixed mode line shape due to the acquisition of single shot phase modulated data in f_1. This results from the coherence transfer selection gradients also serving as outer volume crushers. In order to obtain useful 2-D spectra with minimal baseline distortion, severe echo shaped weighting functions must be applied to remove the dispersive component of the line shape. Since this type of apodization resembles a matched filter for anti-phase data, maximum sensitivity enhancement is achieved. The in-phase cross peaks, however, are attenuated by an echo shaped apodization function. The severe apodization required to remove the dispersive component is the source of the relatively poor performance of in-phase coherence transfer methods with mixed mode line shape.

While all three yield comparable spectra in human bone marrow, the application of water suppression for human brain spectroscopy reveals differences in stability among the three experiments. VOLT, which mixes longitudinal polarization, allows for more efficient suppression of outer volume and water signal due to the residence of the spins residing along z both before and after isotropic mixing. Despite the single shot nature of all three experiments, a four-step phase cycle is required to remove signal generated from unwanted echoes (Section 2.5.3).

2.2 Experimental Design

The VOSY-HOHAHA, VOSY-COSY and VOLT pulse sequences are shown in Figure 2-1. Crusher gradients are applied to allow dephasing of spins outside the localized volume during the DRY-STEAM portion of the sequences. Since these are 2D experiments, coherence transfer pathway selection must be performed either by phase cycling, a spectral difference method, or through the use of gradients. Gradient based coherence transfer selection methods are convenient since the RF inhomogeneity of the mixing scheme generates a moderate amount of unwanted outer volume excitation. These coherence transfer selection gradients must be placed on either side of the

coherence transfer pulse in any 2D experiment. Here, the coherence transfer pulse is either the isotropic mixing scheme in VOLT or VOSY-HOHAHA or the final hard $\pi/2$ pulse in the VOSY-COSY experiment.

The VOSY based experiments place the volume localization scheme prior to the coherence transfer portion of the experiments. The gradients for the localization scheme are identical to those used in any DRY-STEAM experiment, and the timing is such that the stimulated echo forms at the onset of the first coherence transfer selection gradient. The mixing pulse is either a hard $\pi/2$ pulse for VOSY-COSY or an MLEV-17 hard pulse spin lock for VOSY-HOHAHA. The net rotation of MLEV-17 is π radians which leads to less unwanted outer volume signal than the hard $\pi/2$ pulse of VOSY-COSY. The unwanted signal of both experiments is removed by applying a crusher gradient after the mixing pulse. An identical crusher gradient was applied prior to mixing to allow the signal of interest to be refocused. This balanced pair serves to select the coherence transfer pathway of interest in the usual fashion (17).

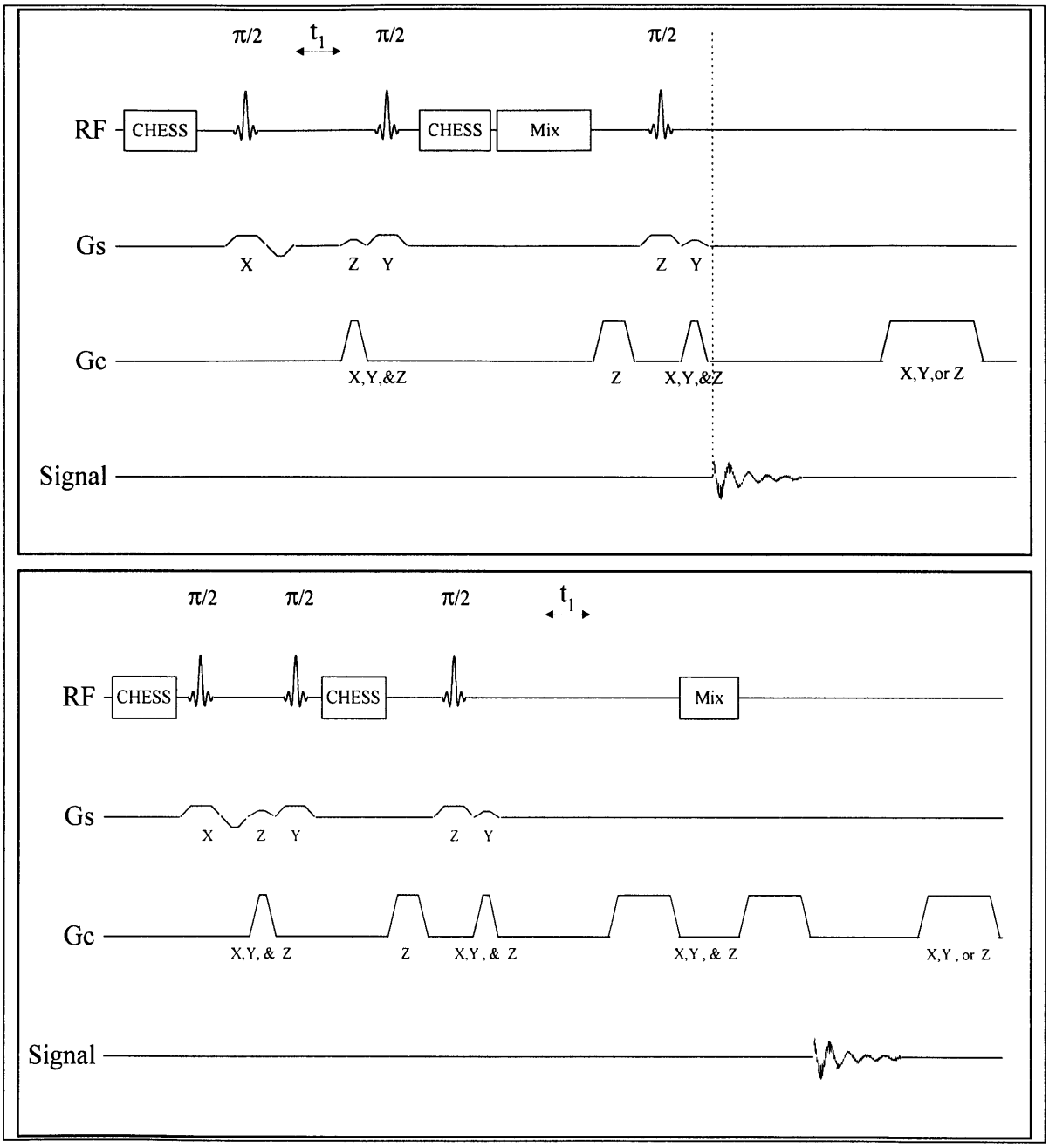

Figure 2-1: VOLT, VOSY-HOHAHA, and VOSY-COSY pulse diagrams.
Pulse sequence diagram for VOLT (upper figure) and VOSY-HOHAHA and VOSY-COSY (lower figure). Coherence transfer is achieved by MIX pulse. The MIX pulse is an isotropic mixing pulse for VOLT and VOSY-HOHAHAH. For VOSY-COSY the MIX pulse is a hard π/2 pulse. Slice select gradients are drawn on the Gs channel. Gradients on the Gc channel crush the outer volume signal as well as signal arising from the P-coherence pathway

In the VOSY experiments, the finite duration of the gradients require that the stimulated echo form at the onset of the first coherence transfer selection gradient. This introduces unavoidable phase errors. These phase errors are easily removed with a magnitude calculation at the expense of resolution. Small to moderate deviations from pure in-phase multiplet structure are also encountered due to J evolution during the delay following the final $\pi/2$ pulse of the DRY-STEAM sequence. Any J evolution during the first interpulse delay is removed by the z-filter behavior of the DRY-STEAM sequence.

The approach taken in the VOLT experiment is to combine the volume localization and coherence transfer selection gradients, reducing the time spent in the transverse plane and, hence, the deleterious effects of T_2 relaxation. This is possible because the form of the DRY-STEAM localization scheme allows easy integration into a z-filtered TOCSY experiment such as those described by Rance (18) and Bazzo and Campbell (19). This approach mixes longitudinal polarization instead of transverse coherence. Since the spins of interest relax by T_1 before and after the isotropic mixing scheme in VOLT, more time is available for application of crusher gradients to manage outer volume signal generated by the mixing scheme.

Water suppression is achieved in all three experiments with two **CHE**mical-**S**hift-**S**elective pulse packets (20). A CHESS packet consists of three frequency selective excitation pulses with unbalanced gradients as shown in Figure 2-2. Three pulses are used instead of one to compensate for imperfect flip angles over the entire volume. The flip angle of the third pulse is adjusted to minimize the water signal and compensate for relaxation prior to acquisition. The gradients are unbalanced with respect to their orientation and duration to avoid the formation of gradient echoes of the water resonance. The gradient durations are in the ratio 5:3:1 with respect to a common duration.

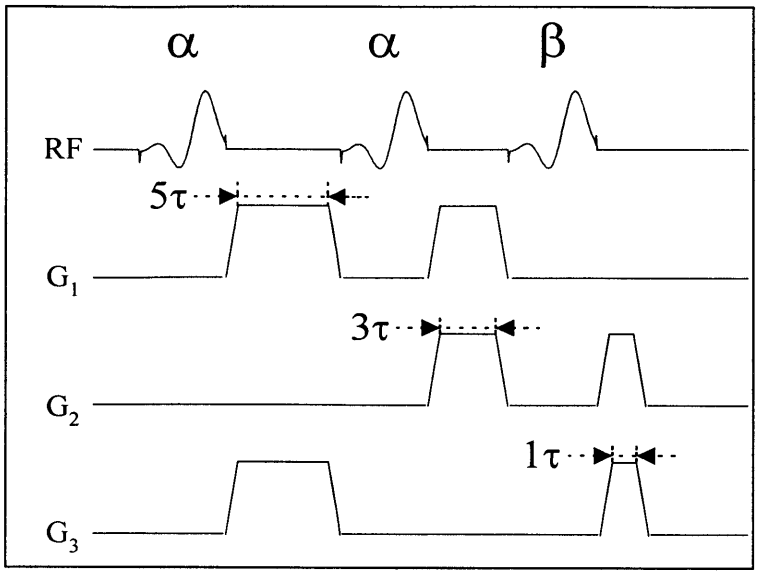

Figure 2-2: A CHESS Pulse diagram.
The durations of the crusher gradients are staggered in the ratio 5:3:1 to avoid the refocusing of water signal. The flip angle of the last pulse of the second CHESS packet is manually adjusted while observing the residual water signal until the water signal at the onset of acquisition is a minimum. The second CHESS packet rotates the orientation of the gradients with respect to the first CHESS packet such that (G_{13},G_{12},G_{23}) rotates to (G_{23},G_{13},G_{12}).

Superior water suppression is achieved when time between the last CHESS pulse and the onset of acquisition is constant for every t_1 increment. The placement of the evolution delay between the first and second $\pi/2$ pulse results in phase errors that can not be removed with simple post processing methods. To remove potential phase errors, a magnitude calculation is performed on the VOLT data in a similar fashion to the VOSY experiments. If absorptive mode data is desired, large non-linear phase corrections may be used during post-processing. However, such a simple approach results in severe baseline distortion.

For all three pulse sequences, the size, shape, and location of the voxel of interest were determined with a series of imaging experiments acquired without water suppression. These imaging experiments used the same pulse sequences shown in Figure 2-1 except a gradient is turned on during acquisition and the receiver bandwidth is set to 16 kHz. This allows a projection of the voxel of interest to be acquired along the axis of

the applied gradient. By measuring the projection along three orthogonal axes, the size, shape, and location of the voxel of interest can be determined. A rewinder gradient must be inserted prior to the read out gradient so the gradient echo will form at the center of the acquisition window. An additional delay is added between the final volume localization pulse and the onset of the first coherence transfer selection gradient to allow for simultaneous formation of the inhomogeneity and imaging gradient echoes.

2.3 Theory

Examining the evolution of a simple AX spin system during VOLT illustrates how the outer volume crusher gradients of a DRY-STEAM experiment also serve as coherence selection gradients. The evolution of an AX spin system may be described with product operators, as described by Sorenson, et al, (21). For illustration purposes, the product operators become intractable after a few rotations. For this reason, only the operators arising from spin 1 are traced through VOLT. An exchange of spin labels generates the corresponding expression for spin 2. Assuming that spin 1 is at equilibrium, the first $\pi/2_x$ pulse rotates the spins into the transverse plane,

$$\sigma_1 = -I_{1y} = \frac{i}{2}\left(I_{1+} - I_{1-}\right). \qquad \textbf{2.1}$$

The spins evolve under their chemical shifts and scalar couplings during the evolution period, t_1. In addition, the spins experience a coherence selection gradient with area, G, before the second $\pi/2_x$ pulse:

$$\begin{aligned}\sigma_3 = & -\frac{i}{2}e^{-i(\gamma Gr+t_1\Omega_1)}\cos(\pi J t_1) I_{1-} + e^{-i(\gamma Gr+t_1\Omega_1)}\sin(\pi J t_1) I_{1-}I_{2z} + \\ & \frac{i}{2}e^{+i(\gamma Gr+t_1\Omega_1)}\cos(\pi J t_1) I_{1+} + e^{i(\gamma Gr+t_1\Omega_1)}\sin(\pi J t_1) I_{1+}I_{2z}\end{aligned} \qquad \textbf{2.2}$$

where γ is gyromagnetic ratio, r is proton's location, and Ω_n is the chemical shift frequency of spin n. After the second $\pi/2$ pulse, σ_3 will be transformed to longitudinal polarization, zero order coherence, first order coherence, and second order coherence,

$$\sigma_3 \rightarrow \sigma_4 \propto \left\{ \begin{array}{l} \{I_{1z}\}, \\ \{I_{1-}I_{2+}, I_{1+}I_{2-}\} \\ \{I_{1-}, I_{1+}, I_{1z}I_{2-}, I_{1z}I_{2+}\}, \\ \{I_{1-}I_{2-}, I_{1+}I_{2+}\} \end{array} \right\}. \qquad \textbf{2.3}$$

The terms of interest are the longitudinal polarization terms I_{1z}. By application of crusher gradients after the mixing scheme for time Δ, the anti-phase terms and double-quantum components of the two-spin coherence terms are dephased. Only the longitudinal polarization terms and the zero-quantum component of the two-spin coherence terms remain. If the mixing scheme generates the isotropic mixing Hamiltonian, the longitudinal polarization is transformed to (22):

$$\begin{aligned} I_{1z} \rightarrow -\frac{1}{2}\Big[& I_{1z}\left(1+\cos(2\pi J \tau_{mix})\right) \\ & + I_{2z}\left(1-\cos(2\pi J \tau_{mix})\right) \\ & + \Big(\underbrace{I_{1+}I_{2-}}_{3} - \underbrace{I_{1-}I_{2+}}_{4}\Big)\sin(2\pi J \tau_{mix})\Big] \end{aligned} \qquad \textbf{2.4}$$

Since π/2 pulses are inefficient at exciting zero-quantum coherence, terms 3 and 4 of Equation 2.4, representing anti-phase zero-quantum coherence, are ignored in future calculations. (Terms 3 and 4 of Equation 2.4 have been labeled with the corresponding number below a horizontal curly bracket.) Following the isotropic mixing scheme, the density operator has the following form,

$$\begin{aligned} \sigma_4 = \frac{1}{2}\left(\frac{e^{-i(\gamma G r + t_1\Omega_1)} + e^{+i(\gamma G r + t_1\Omega_1)}}{2}\right)\cos(\pi J t_1) \\ \left(I_{1z}\left(1+\cos(2\pi J \tau_{mix})\right) + I_{2z}\left(1-\cos(2\pi J \tau_{mix})\right)\right). \end{aligned} \qquad \textbf{2.5}$$

Application of the third $\pi/2_x$ pulse yields:

$$\sigma_5 = \frac{1}{2}\left(\frac{e^{-i(\gamma Gr+t_1\Omega_1)}+e^{+i(\gamma Gr+t_1\Omega_1)}}{2}\right)\cos(\pi J t_1)$$
$$\left(\left(\frac{i}{2}(I_{1+}-I_{1-})\right)(1+\cos(2\pi J\tau_{mix}))+\left(\frac{i}{2}(I_{2+}-I_{2-})\right)(1-\cos(2\pi J\tau_{mix}))\right). \quad \textbf{2.6}$$

The spins experience the second coherence selection gradient and evolve under their current coherence order,

$$\begin{aligned}\sigma_6 = & \frac{i}{4}\left(\frac{e^{-it_1\Omega_1}+e^{+i(2\gamma Gr+t_1\Omega_1)}}{2}\right)\cos(\pi J t_1)(1+\cos(2\pi J\tau_{mix}))I_{1+} \\ & -\frac{i}{4}\left(\frac{e^{-i(2\gamma Gr+t_1\Omega_1)}+e^{+it_1\Omega_1}}{2}\right)\cos(\pi J t_1)(1+\cos(2\pi J\tau_{mix}))I_{1-} \\ & +\frac{i}{4}\left(\frac{e^{-it_1\Omega_1}+e^{+i(2\gamma Gr+t_1\Omega_1)}}{2}\right)\cos(\pi J t_1)(1-\cos(2\pi J\tau_{mix}))I_{2+} \\ & -\frac{i}{4}\left(\frac{e^{-i(2\gamma Gr+t_1\Omega_1)}+e^{+it_1\Omega_1}}{2}\right)\cos(\pi J t_1)(1-\cos(2\pi J\tau_{mix}))I_{2-}.\end{aligned} \quad \textbf{2.7}$$

Because of the difference in coherence order, the gradient only refocuses half of the available magnetization, i.e. the terms that are independent of G. Discarding half of the magnetization is one of the well-known disadvantages of STEAM based experiments. Discarding half of the available signal has severe repercussions concerning the resolution of the resulting 2D spectrum. Illustrating the effect of maintaining one coherence pathway on the spectrum's resolution is postponed momentarily until the final expression for the density operators is generated. The spins evolve under their chemical shifts and scalar couplings during the detection period, t_2, resulting in:

$$\begin{aligned}\sigma_6 = & \frac{1}{8}e^{+it_1\Omega_1}\cos(\pi J t_1)(1+\cos(2\pi J\tau_{mix}))\left(e^{-it_2\Omega_1}\left(\underbrace{\cos(\pi J t_2)I_{1-}}_{1}+\underbrace{2\sin(\pi J t_2)I_{1-}I_{2z}}_{2}\right)\right) \\ & +\frac{1}{8}e^{+it_1\Omega_1}\cos(\pi J t_1)(1-\cos(2\pi J\tau_{mix}))\left(e^{-it_2\Omega_2}\left(\underbrace{\cos(\pi J t_2)I_{2-}}_{3}+\underbrace{2\sin(\pi J t_2)I_{2-}I_{1z}}_{4}\right)\right)\end{aligned} \quad \textbf{2.8}$$

where only the terms involving I. are detectable due to the demodulation of the signal at the time of acquisition and the phase of the receiver has been adjusted to remove a factor

of -i. (The terms of Equation 2.8 have been labeled with the corresponding number below a horizontal curly bracket.) Here, the third term represents in-phase coherence of spin 2 that precessed at the chemical shift of spin 1 during the evolution delay. These terms will contribute to in-phase cross peaks in the 2D spectrum. Since the onset of acquisition is not instantaneous due to the gradient rise and fall times and the selective pulse lengths, some, albeit small, anti-phase evolution will occur following the third $\pi/2$ pulse prior to onset of acquisition.

From the final expression for the density operator, σ_6, the effect of maintaining only one coherence pathway on the spectral line shape is now illustrated. The fundamental problem is the well known mixing of absorptive and dispersive line shapes when phase modulation of the signal occurs in f_1. This problem is identical for coupled and uncoupled spins. For simplicity, the problem is illustrated for an uncoupled spin by setting the scalar coupling constant equal to zero. This simplifies Equation 2.8 to

$$s(t_1,t_2)=\frac{1}{4}e^{+it_1\Omega_1-it_2\Omega_1}\,r(t_1,t_2), \qquad \textbf{2.9}$$

where $s(t_1,t_2)$ is the detected signal of an uncoupled spin, and relaxation, which up until now has been ignored, has been reintroduced with the decay function $r(t_1,t_2)$. All subsequent calculations assume that the decay function is a monotonically decaying exponential in both dimensions with a transverse relaxation time of T_2. A complex Fourier transform in both dimensions yields,

$$S(\omega_1,\omega_2)=\frac{1}{4}\left(A(\omega_1,\Omega_1)+i\,D(\omega_1,\Omega_1)\right)\left(A(\omega_2,\Omega_2)+i\,D(\omega_2,\Omega_2)\right), \qquad \textbf{2.10}$$

where A is the absorptive component of a Lorentzian line shape,

$$A(\omega_n,\Omega_n)=\frac{\left(\pi/T_2\right)}{\left(\pi/T_2\right)^2+\left(2\pi(\omega_n-\Omega_n)\right)^2}, \qquad \textbf{2.11}$$

the imaginary component is the corresponding dispersive component,

$$D(\omega_n,\Omega_n)=\frac{2\pi(\omega_n-\Omega_n)}{\left(\pi/T_2\right)^2+\left(2\pi(\omega_n-\Omega_n)\right)^2}. \qquad \textbf{2.12}$$

Expanding Equation 2.10 yields,

$$S(\omega_1,\omega_2)=\frac{1}{4}\left((A_1A_2-D_1D_2)+i(A_1D_2+D_1A_2)\right). \qquad \textbf{2.13}$$

The notation has been simplified for clarity. The line shapes have equal contributions of both absorptive and dispersive components that can not be separated by phasing. For this reason, spectra that are phase modulated in the indirect dimension are often displayed after a magnitude calculation. This severely diminishes the resolution of the spectrum.

Looking at a 1D Lorentzian line reveals that a spectrum's resolution is severely degraded by the mixing of absorptive and dispersive line shapes. The full width half maximum (FWHM) for the absorptive component alone is

$$\upsilon_{A,\frac{1}{2}}=\frac{1}{2\pi T_2}. \qquad \textbf{2.14}$$

If the spectrum is displayed in magnitude mode, the FWHM for the magnitude peak is

$$\upsilon_{A,\frac{1}{2}}=\frac{\sqrt{3}}{2\pi T_2}. \qquad \textbf{2.15}$$

The increase in the FWHM is a result of including the long tails of the dispersive component in the spectrum. The loss of spectral resolution is further exacerbated at lower maximums as is illustrated in Table 2-1. The inclusion of the dispersive component decreases the spectral resolution. This loss of spectral resolution is extremely important for *in vivo* applications. *In vivo* cross peaks have very small intensities compared to the large diagonal peaks. If the dispersive component is retained in the spectrum, the tails of the larger diagonal resonances often obscure the smaller cross peaks.

Amplitude	Absorptive	Magnitude	Ratio
1 / 2	1.00	1.73	1.73
1 / 4	1.73	3.87	2.24
1 / 8	2.65	7.94	2.99

Table 2-1: Line width comparison.
The relative line width of the absorptive and magnitude components of a damped exponential sinusoid to the FWHM of the absorptive component. The Ratio column is the ratio of the magnitude component to the absorptive component. The Full Width Half Maximum (Amplitude = 1/2), Full Width Quarter Maximum (Amplitude = 1/4), and Full Width Eighth Maximum (Amplitude = 1/8) are in the first, second, and third rows respectively.

The dispersive component results in severe broadening of spectral lines. This broadening may obscure correlation peaks, and therefore, must be removed prior to FT. The dispersive component may be removed by weighting the data with a function in the time domain such that the data envelope resembles an echo. Applying an echo shaped apodization function such as the pseudo-echo (23,24), the Lorentz to Gauss transformation (25), or shifted $\sin^2$ bell transformation (26) results in severe attenuation of the cosine modulated diagonal peaks. These same apodization functions have less pronounced effect on the sine modulated correlation peaks since they resemble a matched filter. These echo shaped apodization functions are routinely applied to COSY data since the correlation peaks are sine-modulated by J during both acquisition times. In TOCSY experiments, the diagonal and cross peaks both exhibit a cosine modulation by J during evolution, and therefore, are attenuated by an echo shaped apodization function.

The Results section in this chapter will show that the raw signal-to-noise ratio of isotropic mixing based experiments is indeed higher than VOSY-COSY but that the apodization function negates this advantage. The signal loss observed in VOLT and VOSY-HOHAHA is due to poor pulse sequence design. The full SNR may be recovered by directly avoiding the detection of the dispersive component. This new approach is introduced in detail in Chapter 3.

2.4 Methods

All NMR experiments for this thesis were performed on a 1.5 Tesla General Electric Signa imaging system. The described pulse sequence was incorporated into the version 5.4 PROBE® spectroscopy software package. This package allows for placement of an arbitrary voxel over the region of interest via a graphical prescription interface. The voxels were prescribed from 2 cm thick single axial images (256 x 128) obtained with a single gradient recalled echo sequence TR 100 ms, TE 3 ms and 1 shot per phase encode. All localized voxels were 59 mL in volume (5.2 x 4.2 x 2.7 cm). Manual shimming was performed with linear gradients. Imaging, voxel localization, shimming and parameter optimization typically requires 15 minutes. The standard linear extremity coil was used for the corn oil and bone marrow studies, and the standard quadrature head coil was used for the water-suppressed studies. In both cases, the coils were used for both transmission and reception. The transmitter was placed in the center of the spectrum for mixing and acquisition, avoiding the need for linear phase modulation of the mixing scheme. All dephasing gradients were applied at 0.9 G/cm. Processing and data acquisition parameters are given in the figure legends.

All pulse sequences presented in this thesis were evaluated in four different samples: a 2 liter bottle of corn oil, human bone marrow, a 3 liter spherical 17 mM NAA phantom, and human brain tissue. Corn oil is commonly used as the model for human fat and yields similar spectra to that of human bone marrow. Lipid spectroscopy on corn oil and human bone marrow was done to test the sequences without the complications associated with water suppression. The NAA phantom was used to test and optimize the sequences with water suppression. Spectra acquired from human brain tissue tested the sequences' sensitivity and resolution under *in vivo* conditions.

The mixing scheme consisted of six WALTZ-4 cycles in the VOLT and two MLEV-17 cycles in the VOSY-HOHAHA experiments, respectively. Both utilized an RF

field strength of 463 Hz for a total mixing time of 71.3 ms for VOSY-HOHAHA and 64.8 ms for VOLT. All experiments utilized 96 t_1 increments in the indirect dimension allowing the coherence transfer echo to be adequately sampled in the VOSY-COSY experiments. The spectral width was 750 Hz for all studies allowing for an optimal acquisition time of approximately 1/J for the VOSY-COSY experiment. The phase of the first $\pi/2$ pulse and receiver were incremented by 180 degrees with every t_1 increment to force the axial peaks to the edge of the spectra in the indirect dimension (27).

2.5 Results

2.5.1 Corn Oil Experiments

Volume localization is achieved by the intersection of three orthogonal slice selective pulses in all three experiments: VOLT, VOSY-HOHAHA, and VOSY-COSY. In VOSY-HOHAHA and VOSY-COSY, volume localization is placed prior to the coherence transfer and is independent of the coherence selection gradients. The coherence selection gradients of VOLT are also used for outer volume suppression. This forces VOLT to acquire only the N-coherence pathway.

All three experiments obtained projections of the voxel of interest from the corn oil phantom without phase cycling along all three axes. This was done to ensure that the acquired signal was arising from the voxel of interest and not from the outer volume. These projections were normalized after Fourier Transform and displayed in Figure 2-3. All three methods yield single shot volume localization as is evident from the lack of outer volume signal in the identical profiles.

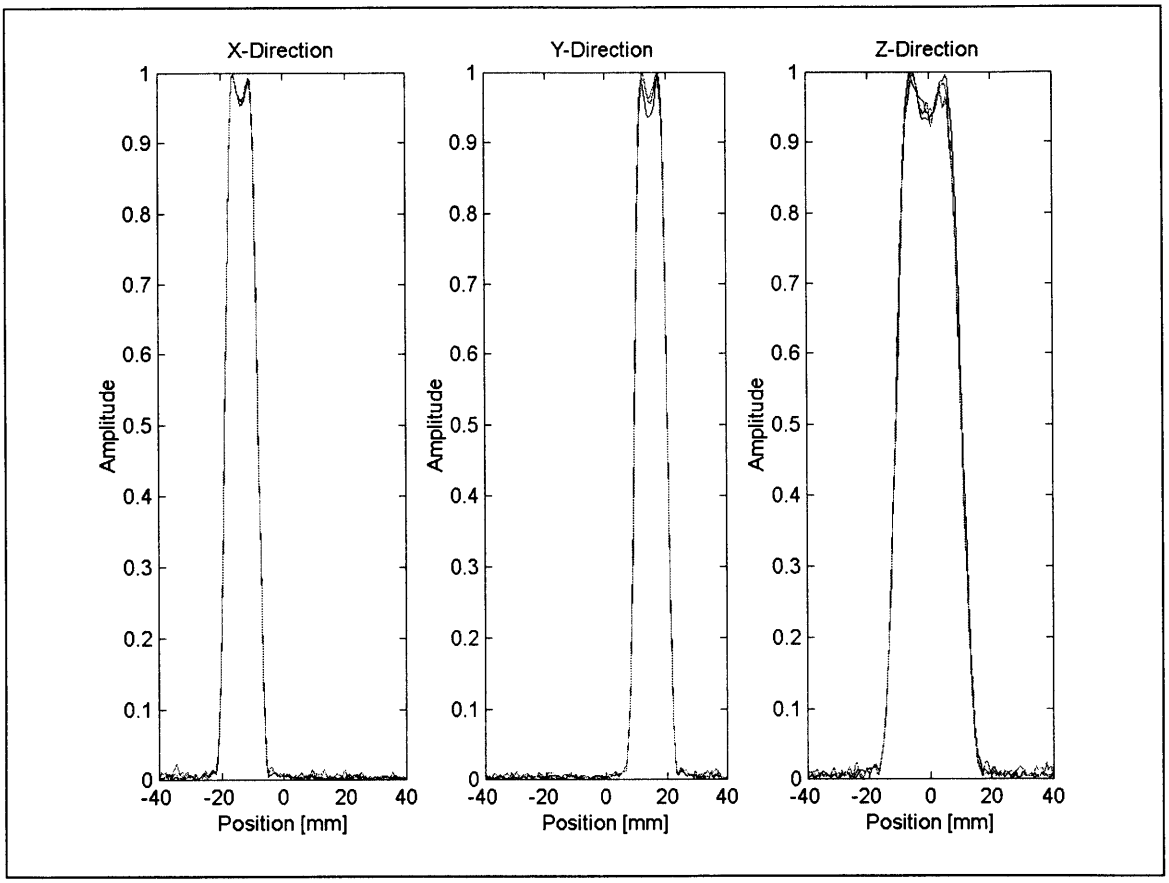

Figure 2-3: Volume localization experiments.
Overlapping projections of the voxel of interest obtained with VOLT, VOSY-HOHAHA, and VOSY-COSY in a corn oil phantom. There is no distinquishable difference between the projections obtained with the three experiments. Volume localization is achieved with three orthogonal $\pi/2$ pulses, which are identical in all three experiments. Projections along X, Y, and Z were 1.2, 1.2, and 2.3 centimeters respectively.

Figure 2-4 normalizes the projections along a particular axis with respect to the VOLT projection and plots them separately. The amplitudes of these projections provide some insight into the available signal contained in the voxel for each experiment. The VOSY-COSY projections have the largest amplitudes among the three pulse sequences because VOSY-COSY has the shortest time between the first $\pi/2$ pulse and acquisition. VOSY-COSY has the largest available signal despite the fact that half of the available magnetization is discarded with the mixing pulse. The signal available with VOLT is less than that of COSY. This is due to the fact that the spins relax during the isotropic mixing scheme. The VOSY-HOHAHA experiment provides the least amount of signal for spectroscopy. Volume localization in VOSY-HOHAHA requires the same amount of time as the VOSY-COSY experiment, the additional loss of signal in VOSY-HOHAHA occurs during the isotropic mixing scheme.

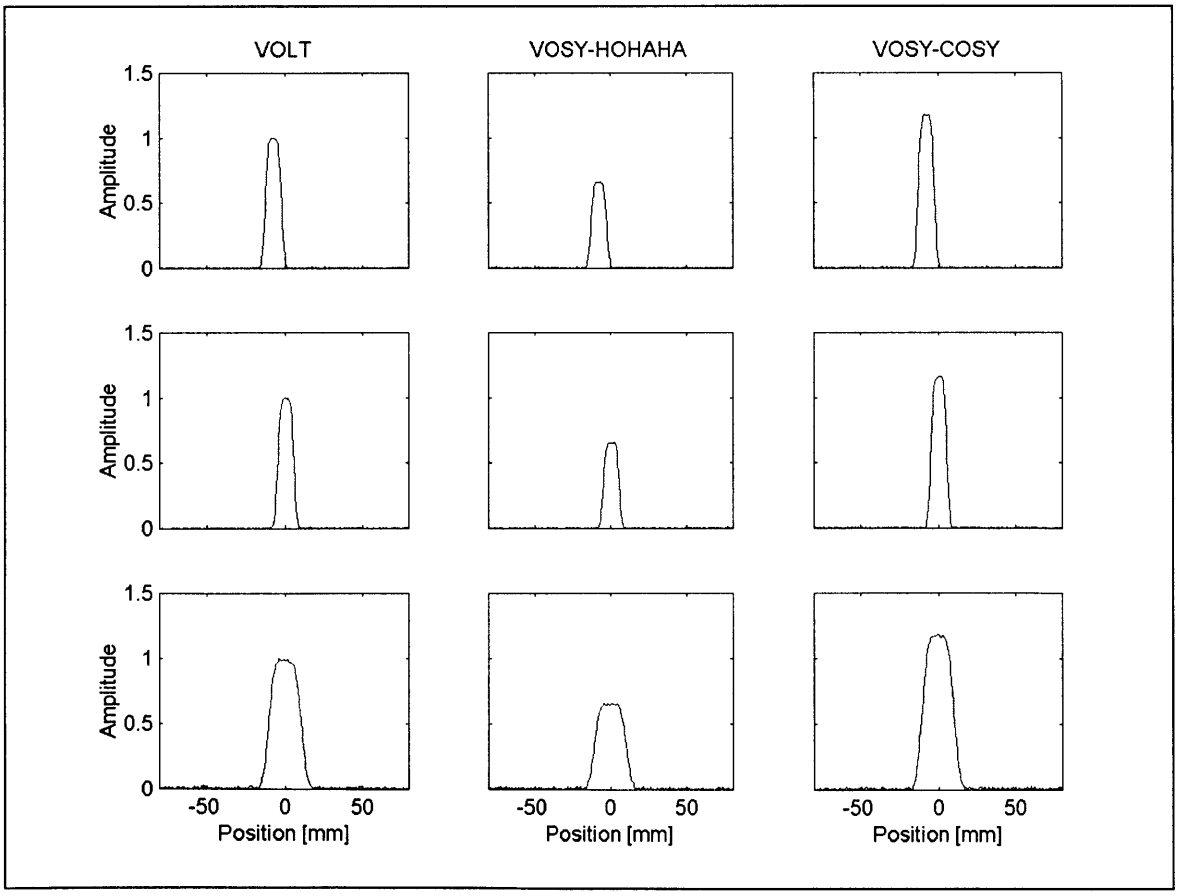

Figure 2-4: Normalized projections of VOLT, VOSY-HOHAHA, & VOSY-COSY. Normalized magnitude projections of VOLT (first column), VOSY-HOHAHA (second column), and VOSY-COSY (third column) are plotted. Voxel projections were obtained along X (first row), Y (second row), and Z (third row) directions. These projections each were acquired without phase cycling.

To confirm that the signal lost during VOLT and VOSY-HOHAHA is a result of relaxation, the isotropic mixing scheme in both experiments was replaced with a 480 μs delay and a 480μs hard π pulse, respectively. Figure 2-5 shows the normalized projections with respect to the VOLT projections. With the long isotropic mixing schemes removed, VOLT has the shortest time between excitation and acquisition. This results in the VOLT projections being slightly greater than VOSY-HOHAHA. The available signal with VOSY-HOHAHA is greater than the VOSY-COSY experiment by a factor of two. VOSY-COSY uses a hard π/2 pulse in order to transfer coherence. Therefore, the coherence selection gradients on either side of this pulse eliminates half of

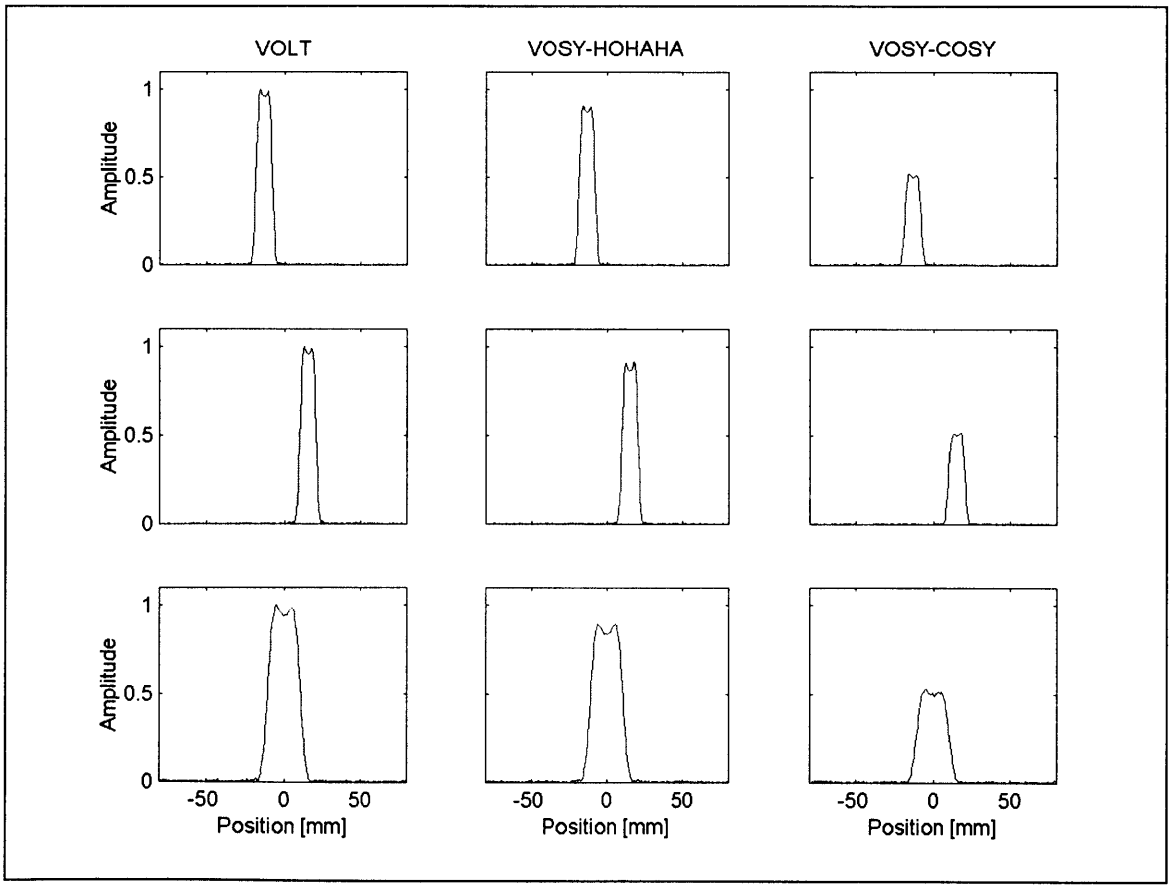

Figure 2-5: Normalized projections without isotropic mixing.
Magnitude projections of VOLT (first column), VOSY-HOHAHA (second column), and VOSY-COSY (third column) are plotted. Voxel projections were obtained along X (first row), Y (second row), and Z (third row) directions. All projections were scaled in relation to the normalized VOLT projections. Each projection was acquired without phase cycling. Isotropic mixing in VOLT and VOSY-HOHAHA was replaced with a 480 microsecond delay and a hard 480 microsecond π pulse, respectively.

the available signal.

The projections of the voxel of interest reveal that all three experiments achieve single shot volume localization, which is essential for *in vivo* spectroscopy experiments (Section 3.5.3). In addition, the projections reveal that all three experiments excite the same voxel with respect to shape and location. The amplitudes of the projections differ among the three experiments as a result of relaxation due to differences in timing. VOSY-COSY has superior sensitivity in imaging mode compared to the other two experiments because it has the shortest time between excitation and acquisition. However, this sensitivity advantage is not realized in spectroscopy mode because the VOSY-COSY anti-phase cross peaks destructively interfere with each other.

For reference, Figure 2-6 shows a schematic diagram of a triglyceride molecule above a 1D spectrum of the corn oil phantom used for the *in vitro* studies. The proton assignments are provided.

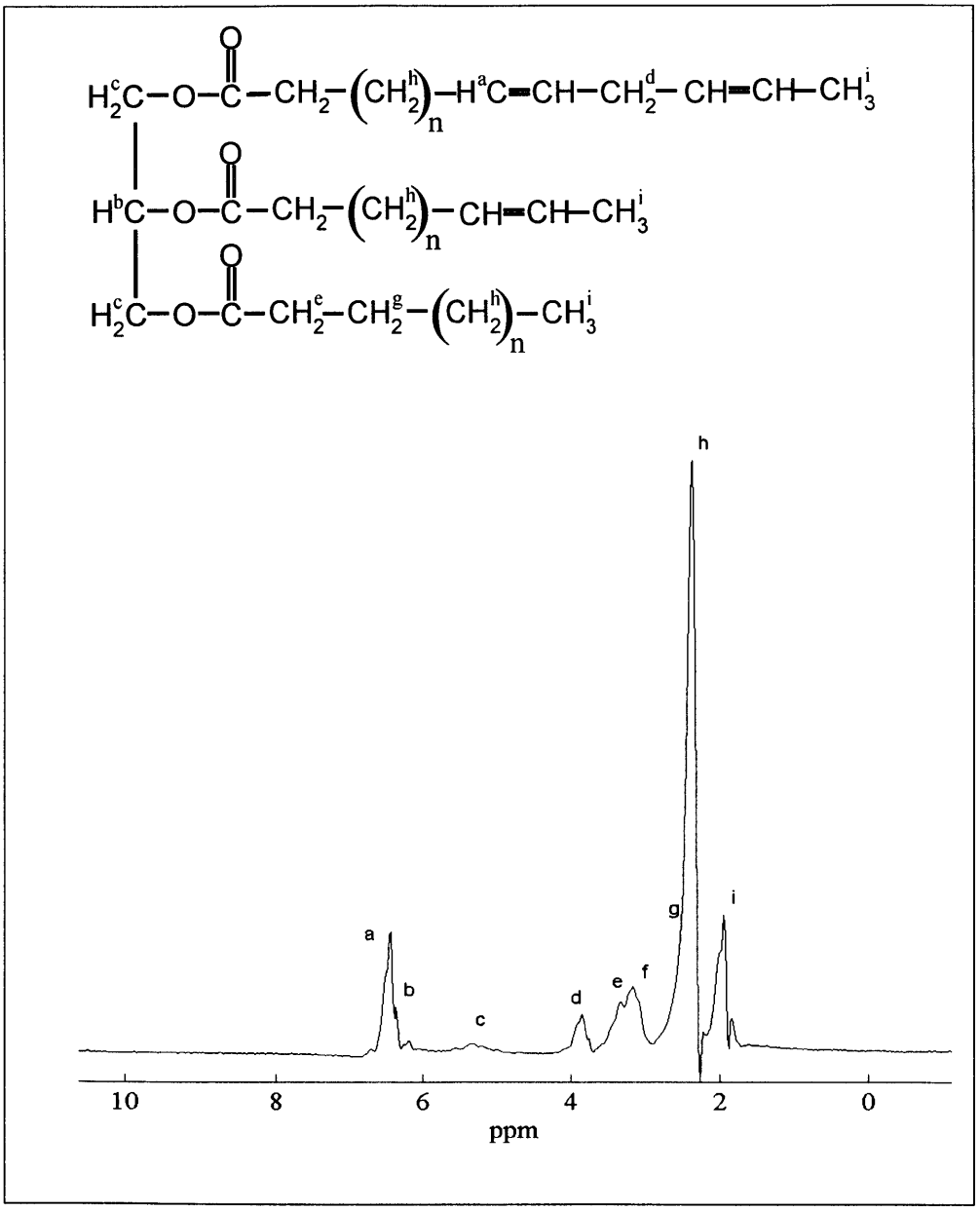

Figure 2-6: 1D Corn Oil Spectrum
A schematic molecule of triglyceride is shown above a single voxel 1D spectrum of the corn oil phantom. The upper side chain is diunsaturated, the central side chain is mono-unsaturated and the lowest is fully saturated. The resonance assignments in the 1D spectrum reflect the labeling of the proton sites given in the molecular schematic.

To illustrate the removal of the dispersive wings by an apodization function, 2D spectra were acquired from corn oil with VOLT, VOSY-HOHAHA, and VOSY-COSY. The left column of Figure 2-7 shows a direct comparison of VOLT, VOSY-HOHAHA and VOSY-COSY applied to a phantom of corn oil. The 2D data are the result of 2D FT following zero filling from 96 x 192 to 512 x 512 complex points. No apodization was applied and all spectra are magnitude calculated. The traces along the top are taken parallel to F_2 at the location indicated in the 2D spectra below by a dashed line. Several cross peaks appear at appropriate locations, consistent with previously published proton assignments (28). It is apparent that the signal-to-noise ratio (SNR) of the three experiments is similar in the favorable susceptibility environment of the oil phantom.

The right column of Figure 2-7 shows the same spectra following apodization with non-shifted sine^2 bell functions in t_1 and in t_2. Marked improvement in the 2D spectral quality is achieved by minimization of the dispersive contribution to the line shape, but at the expense of the cross peak SNR in the VOLT and VOSY-HOHAHA experiments. Even though the cross peaks intensity of all three experiments were comparable in the unweighted data, the cross peak intensities of the apodized spectra show that the sensitivity of VOSY-COSY is approximately twice that of VOLT and VOSY-HOHAHA, confirming that the sensitivity loss is due to the apodization function.

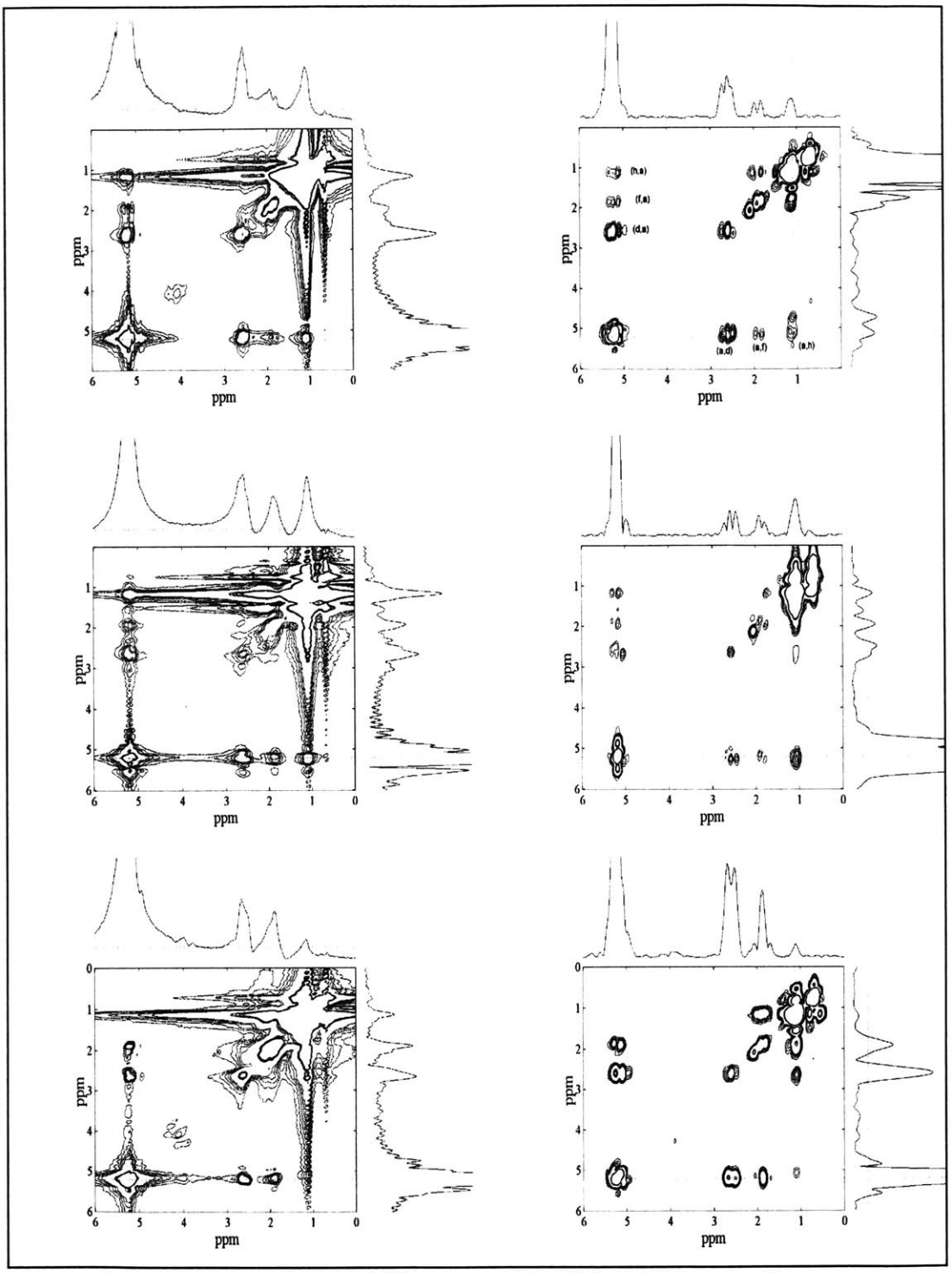

Figure 2-7: VOLT, VOSY-HOHAHA, and VOSY-COSY corn oil spectra.
VOLT, VOSY-HOHAHA, and VOSY-COSY corn oil spectra are shown in the first, second, and third rows, respectively. The left column is the raw data of each spectrum, which was zero filled to 512 in both dimensions followed by 2D Fourier transform. The right column shows the apodized spectra. Apodization function consisted of a 0-degree shifted sine squared bell which was applied in both dimensions prior to zero filling and Fourier transform. Contour levels were drawn the same for all three experiments. The contour levels in the right column are drawn 8 times lower than the contour levels in the left.

Axial peaks in a 2D spectrum should be minimized in order to avoid contamination of the peaks of interest. This is primarily accomplished by minimizing the time between first excitation and acquisition. Figure 2-8 compares VOLT, VOSY-HOHAHA, and VOSY-COSY with and without phase cycling as a means of comparing the intensity of the axial peaks. The spectra in the left column were acquired without phase cycling and the spectra in the right column were acquired with a two-step phase cycle by phase alternation of the first $\pi/2$ pulse. Axial peaks are clearly seen at the edges of the indirect dimension of the spectra acquired without phase cycling. The axial peaks could be further suppressed by increasing the final coherence selection gradient. However, this would result in sensitivity loss for the signal of interest as a result of additional relaxation.

VOLT and VOSY-COSY have the smallest and largest contribution of axial peaks, respectively. The axial peaks in VOSY-HOHAHA and VOSY-COSY are larger than VOLT because of the additional delay to acquisition. VOSY-COSY has larger axial peaks than VOSY-HOHAHA because the $\pi/2$ mixing pulse excites additional signal that does not see the first $\pi/2$ pulse.

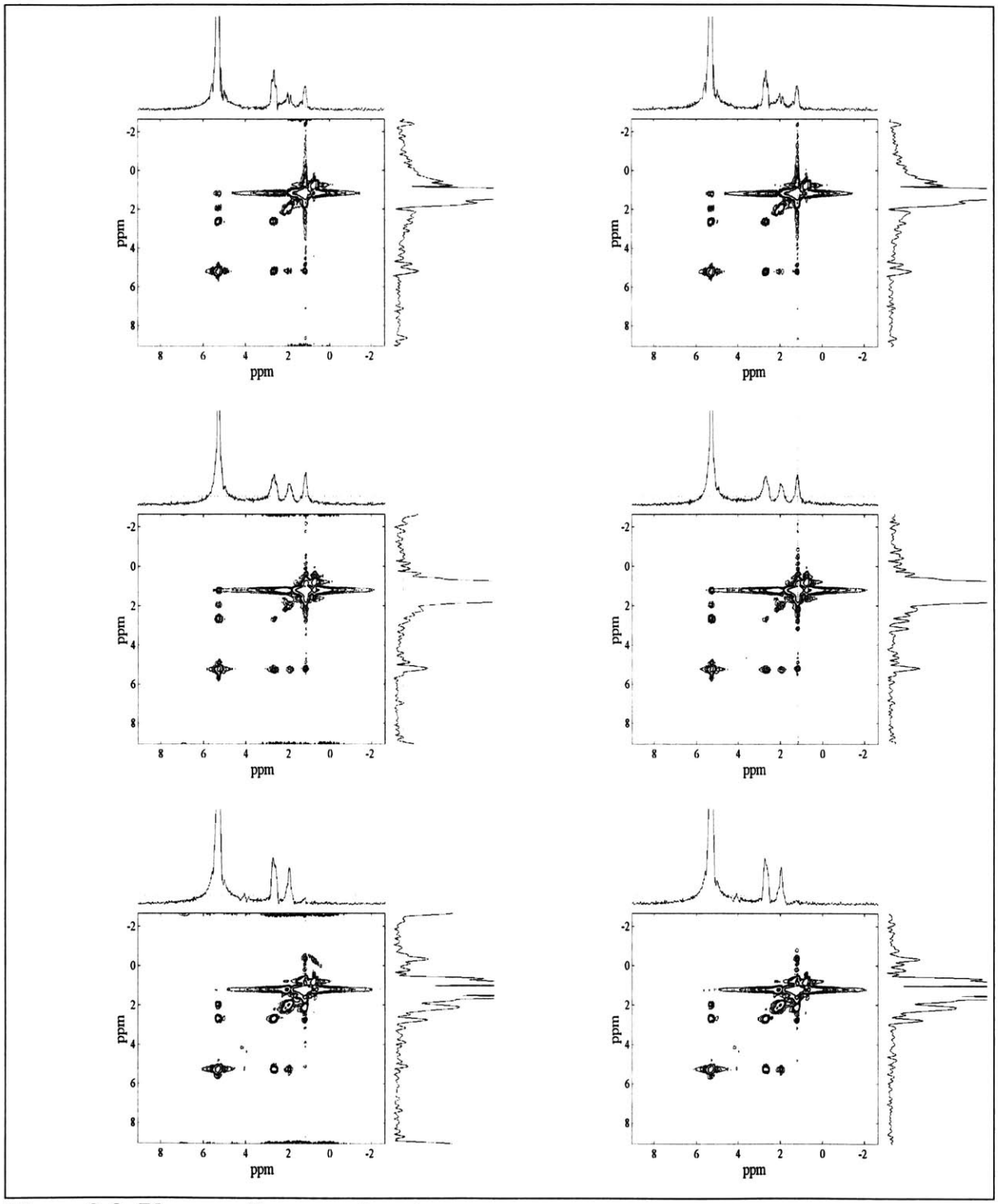

Figure 2-8: Phase cycling experiments.

Corn oil spectra were obtained with VOLT (top row), VOSY-HOHAHA(middle row), and VOSY-COSY (bottom row). The spectra displayed on the left were acquired without phase cycling. The spectra on the right were acquired with a two step phase cycle by alternating the phase of the first pulse and receiver by 180 degrees. The number of averages per t_1 increment is identical for each data set. All data sets have been weighted by a $\pi/8$ shifted sine squared bell in both dimensions, zero filled to 512 points, Fourier transformed, and magnitude displayed.

2.5.2 Human Bone Marrow Experiments

Human bone marrow is a good sample to test the sequences under *in vivo* conditions for two reasons. First, water suppression is not necessary because all of the experiments provide excellent volume localization. And second, the heterogeneity of the bone marrow results in severe line broadening due to magnetic susceptibility. Human bone marrow, therefore, is an excellent sample to illustrate the additional information provided by 2D spectra when severe line broadening is present. The location of the voxel of interest is chosen with respect to a gradient localizer image (Figure 2-9). For all human bone marrow experiments, a 10x10x20 millimeter voxel was prescribed. Measuring the FHWM of the projections (not shown) revealed that signal was detected from a 11.8x11.8x22.5 millimeter voxel. Bone marrow spectra obtained from the selected 3.1 mL voxel with VOLT, VOSY-HOHAHA, and VOSY-COSY are shown in Figure 2-10. The total acquisition time for each spectrum was 24 minutes.

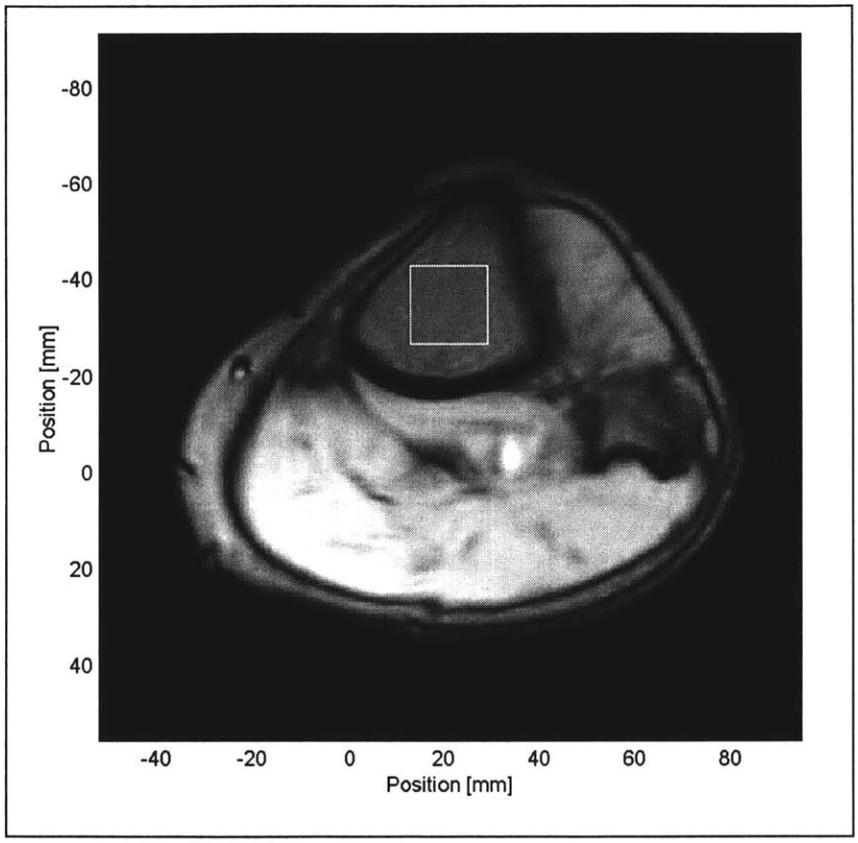

Figure 2-9: Gradient localizer image for bone marrow studies

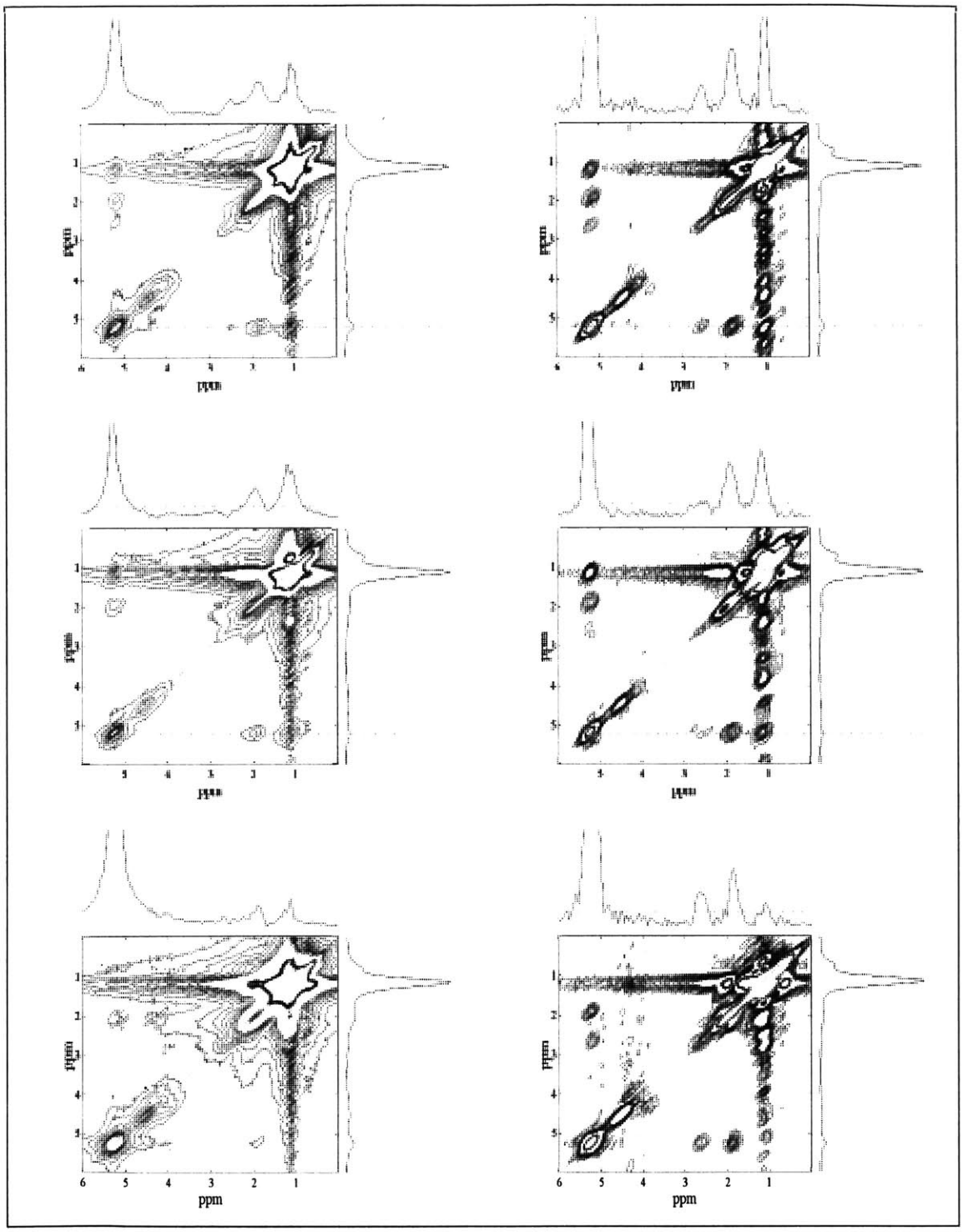

Figure 2-10: Tibial bone marrow spectra.
VOLT (top row), VOSY-HOHAHA (middle row), and VOSY-COSY (bottom row) 2D spectra of tibial bone marrow. The unweighted and weighted data are presented in the left and right column, respectively. Raw data was zero filled to 512 points prior to applying a 2D Fourier transform. The weighted spectra were processed with a $\pi/8$-degree shifted sine squared bell applied in both dimensions prior to zero filling.

The cross peak signal intensity for VOLT and VOSY-HOHAHA is slightly larger than that obtained with VOSY-COSY in the unweighted spectra. Large dispersive wings are present in all three experiments. In order to remove the dispersive component and obtain absorptive mode spectra, a $\pi/8$ degree shifted sine square bell was applied in both dimensions prior to zero filling to 512 points and Fourier transforming. The cross peaks in the VOSY-COSY data retain much more of their intensity than the isotropic mixing experiments. This is a result of applying a matched filter to the anti-phase cross peaks. The signal intensity of the VOSY-COSY data is comparable to the VOLT and VOSY-HOHAHA data as demonstrated by Brereton et. al. (8). Comparing chemical shift correlation patterns reveals that VOLT is superior in sensitivity when compared to VOSY-HOHAHA.

2.5.3 NAA Phantom Experiments

The NAA phantom was used to evaluate the water suppression in all three experiments. In order to evaluate the water suppression for a series of 2D experiments in a reasonable amount of time, the bandwidth in the indirect dimension was decreased to 125 Hz and only 16 t_1 increments were acquired. This shortened the acquisition time to approximately 3 minutes for each experiment while the last t_1 increment remained at 96 milliseconds. Decreasing the bandwidth in the indirect dimension resulted in aliasing along that direction. Taking a maximum intensity projection along the indirect dimension eliminated the effect of aliasing. This operation collapsed each 2D spectrum to a 1D Maximum Intensity (MI) spectrum. Spectra acquired with VOLT, VOSY-HOHAHA, and VOSY-COSY are shown in Figure 2-11 through Figure 2-13 respectively. These short acquisition time experiments were repeated with different phase cycling conditions and displayed as stacked spectra in each figure. The MI spectra are shown from front to back with phase cycling first and third $\pi/2$ pulse, phase cycling first $\pi/2$ pulse, phase cycling third $\pi/2$ pulse, and no phase cycling at all, respectively. In addition to phase cycling, the MI spectra were acquired with different coherence selection gradient durations: 2 millisecond (top row) and 6 millisecond (bottom row).

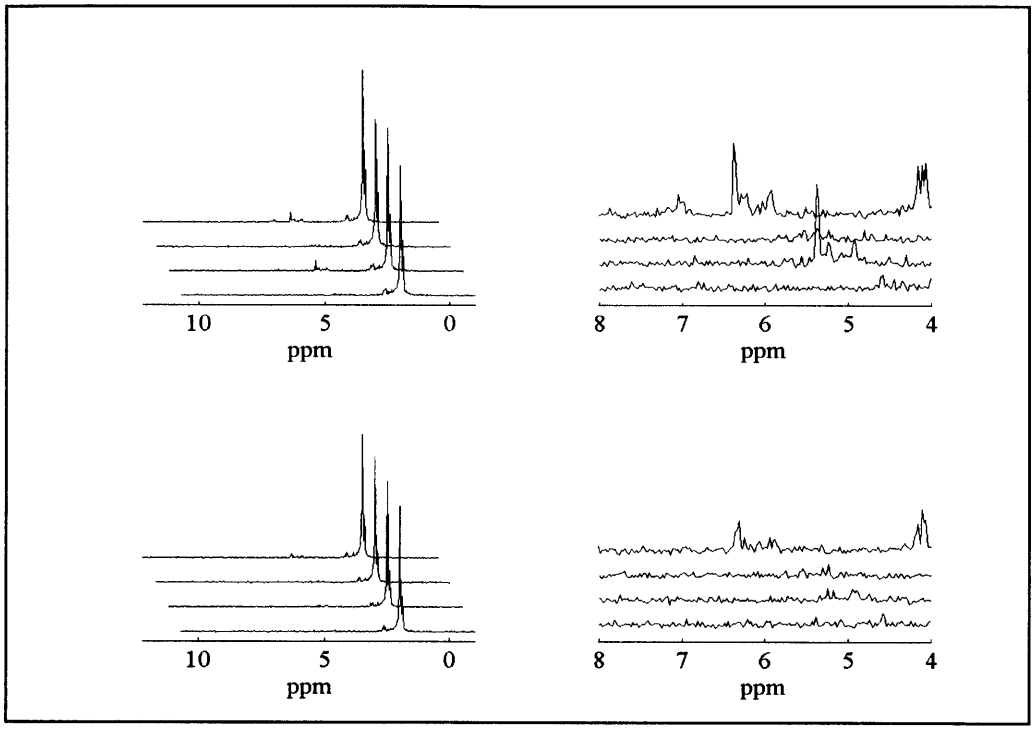

Figure 2-11: Phase cycling experiments with VOLT.
1D Maximum Intensity Projection spectra displayed in stacked plot format. Spectra were obtained with 2 millisecond coherence selection gradients (top row) and 6 millisecond coherence selection gradients (bottom row). Four different phase cycles were used when acquiring the spectra. From front to back: phase cycling first and third $\pi/2$ pulse, phase cycling first $\pi/2$ pulse, phase cycling third $\pi/2$ pulse, and no phase cycling at all. The right column displays the same spectra as the left column except focused around the water resonance.

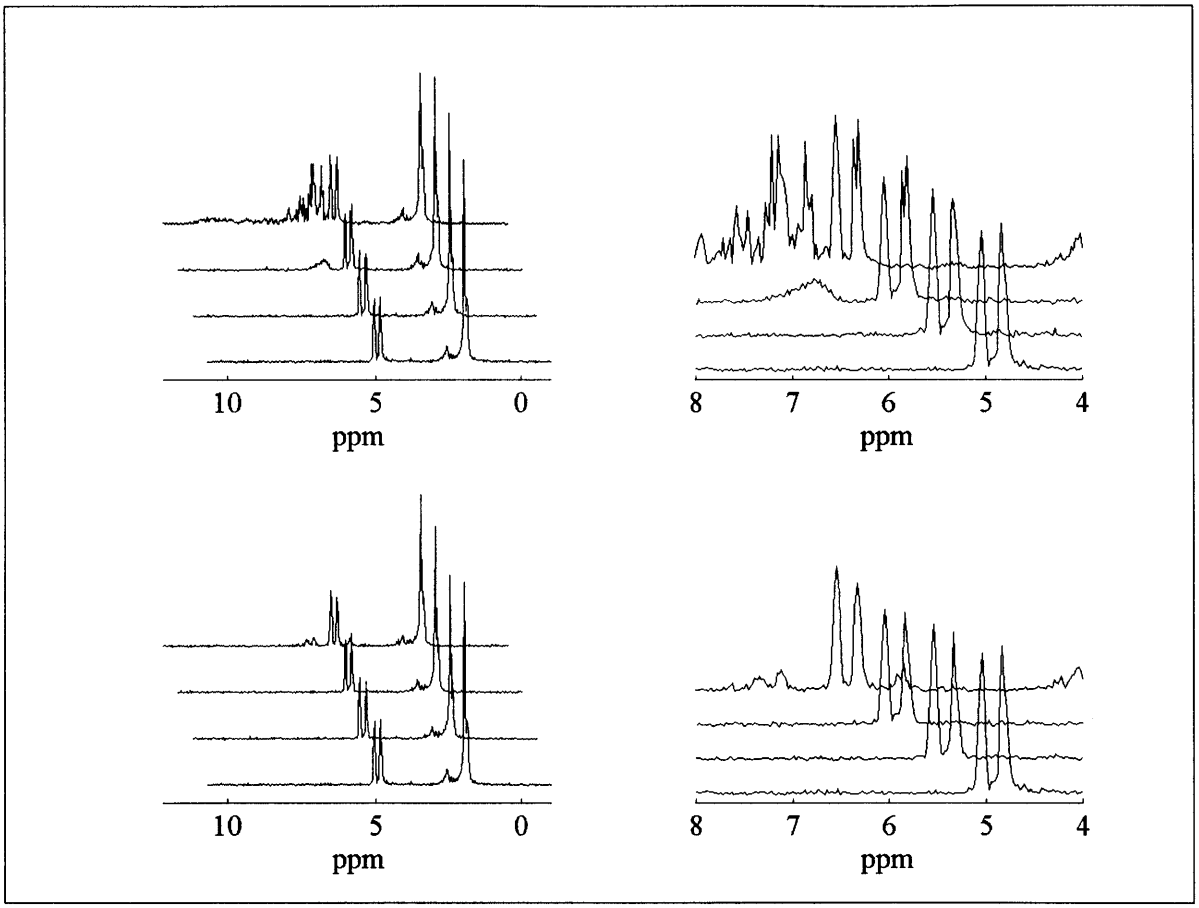

Figure 2-12: Phase cycling experiments with VOSY-HOHAHA.
1D Maximum Intensity Projection spectra displayed in stacked plot format. Spectra were obtained with 2 millisecond coherence selection gradients (top row) and 6 millisecond coherence selection gradients (bottom row). Four different phase cycles were used when acquiring the spectra. From front to back: phase cycling first and third $\pi/2$ pulse, phase cycling first $\pi/2$ pulse, phase cycling third $\pi/2$ pulse, and no phase cycling at all. The right column displays the same spectra as the left column except focused around the water resonance.

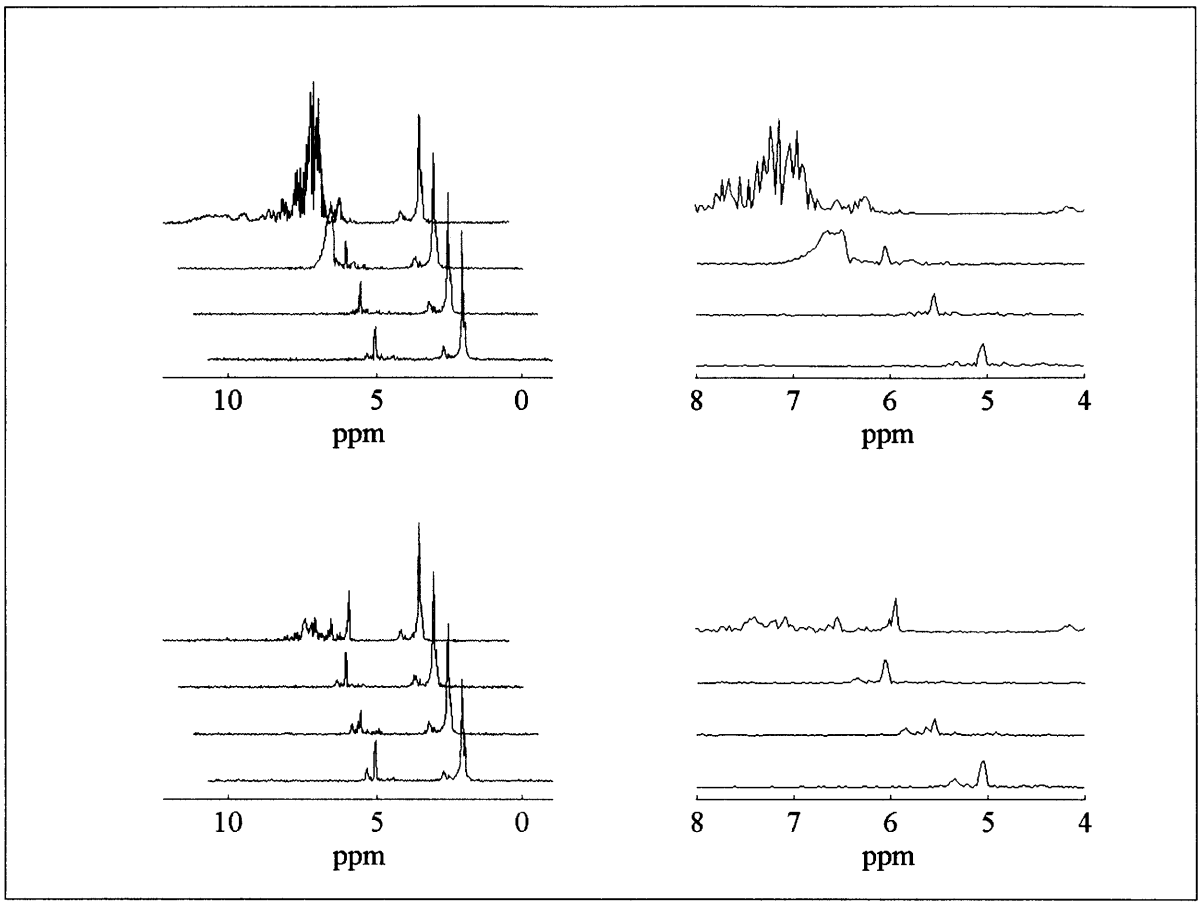

Figure 2-13: Phase cycling experiments with VOSY-COSY.
1D Maximum Intensity Projection spectra displayed in stacked plot format. Spectra were obtained with 2 millisecond coherence selection gradients (top row) and 6 millisecond coherence selection gradients (bottom row). Four different phase cycles were used when acquiring the spectra. From front to back: phase cycling first and third $\pi/2$ pulse, phase cycling first $\pi/2$ pulse, phase cycling third $\pi/2$ pulse, and no phase cycling at all. The right column displays the same spectra as the left column except focused around the water resonance.

Comparing the residual water signal acquired with VOLT, VOSY-HOHAHA, and VOSY-COSY reveals that VOLT has superior water suppression. Residual water signal may further be suppressed by phase cycling the first and third $\pi/2$ pulse. Increasing the coherence selection gradients from 2 milliseconds to 6 milliseconds helps to suppress the residual water signal in both VOSY experiments.

These experiments reveal that VOLT has superior water suppression compared to the VOSY experiments. VOLT's superior water suppression is due to the placement of the t_1 increment between the two CHESS packets. Locating the t_1 increment between the two CHESS packets improves the stability of the water because the time between the last CHESS and acquisition is constant. In addition, VOLT's superior water suppression is

demonstrated by the need for only 2 millisecond coherence selection gradients as opposed to 6 millisecond coherence selection gradients needed by the VOSY experiments.

Figure 2-14 shows the 2D spectra of the NAA phantom obtained with VOLT, VOSY-HOHAHA, and VOSY-COSY. Each spectrum was acquired with the optimum four-step phase cycle. The VOLT experiment used 2 ms crusher gradients while VOSY-HOHAHA and VOSY-COSY required 6 ms crusher gradients to adequately suppress the water signal. The need to use 6 millisecond crusher gradients *in vivo* for the VOSY experiments will be shown in the next section. The differences in the coherence transfer pathways between VOLT and VOSY-HOHAHA compared to VOSY-COSY are clearly seen by comparing cross peak patterns. The visible cross peaks in the NAA spectra show that the NAA phantom has degraded over a period of eight months. The cross peaks at 2.65 ppm in the indirect dimension and 4.0 ppm in the direct dimension are due to aspartate.

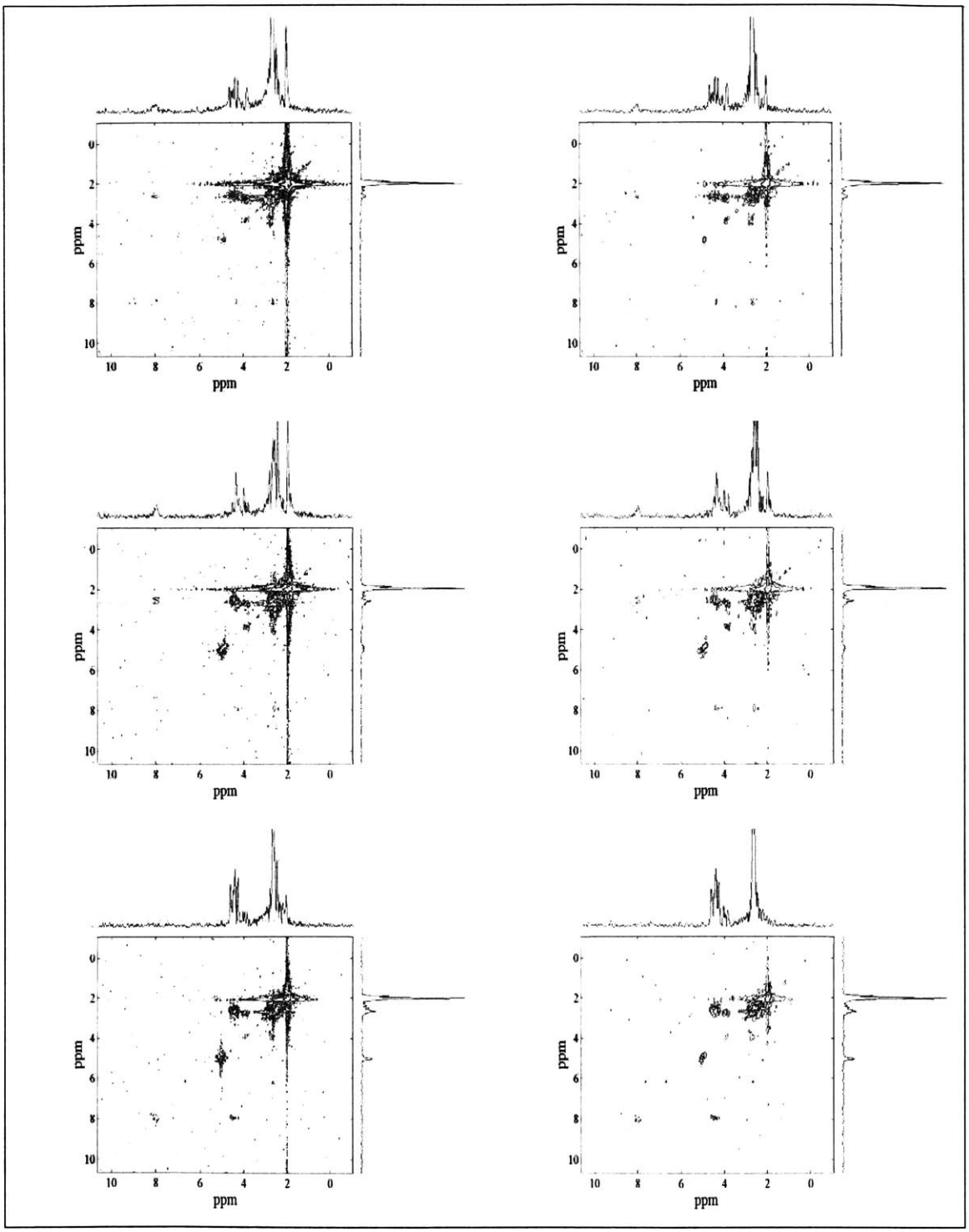

Figure 2-14: NAA spectra acquired with VOLT, VOSY-HOHAHA, VOSY-COSY
NAA spectra acquired with VOLT (top row), VOSY-HOHAHA (middle row), and VOSY-COSY (bottom row). VOLT spectra were acquired with 2 millisecond coherence selection gradients, while VOSY-HOHAHA and VOSY-COSY both used 6 millisecond coherence selection gradients. Unapodized and apodized spectra are displayed in the left and right columns, respectively. A $\pi/8$ shifted sine squared bell was used for the weighting function.

2.5.4 Human Brain Experiments

Brain spectroscopy is the ultimate test for 2D chemical shift correlation experiments. Water must be suppressed by five orders of magnitude, sensitivity per acquisition must be maximized to detect metabolites in millimolar concentrations, and RF power deposition must be within FDA guidelines. The typical setup time including volume selection, shimming, and optimizing the water suppression is 10 minutes. Figure 2-15 is a typical gradient localizer used for defining the voxel in human brain spectroscopy. The voxel of interest has been placed in the parietal lobe unless otherwise indicated.

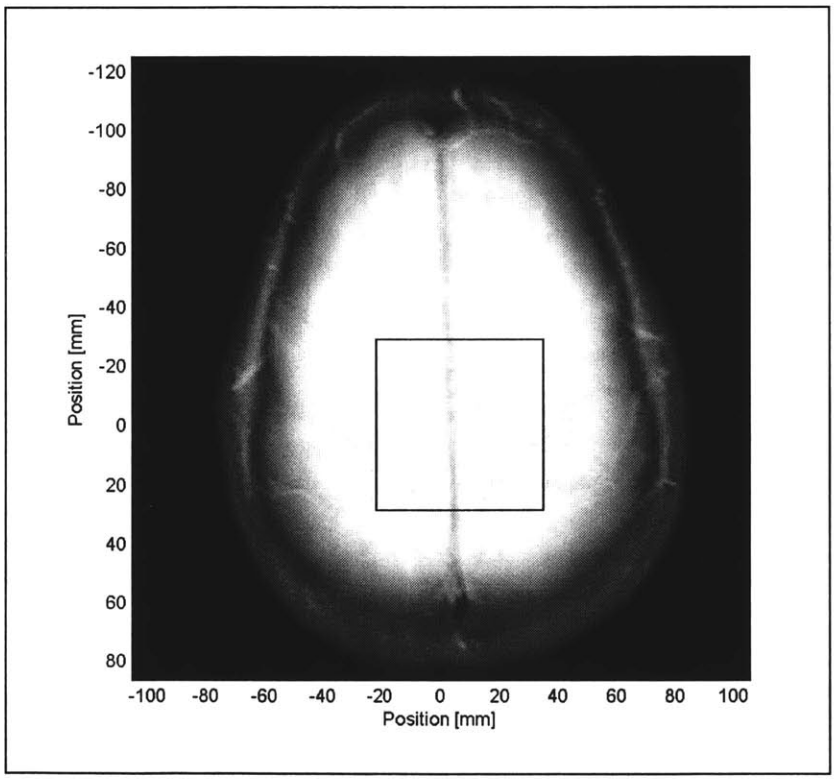

Figure 2-15: Gradient localizer for human brain spectroscopy.

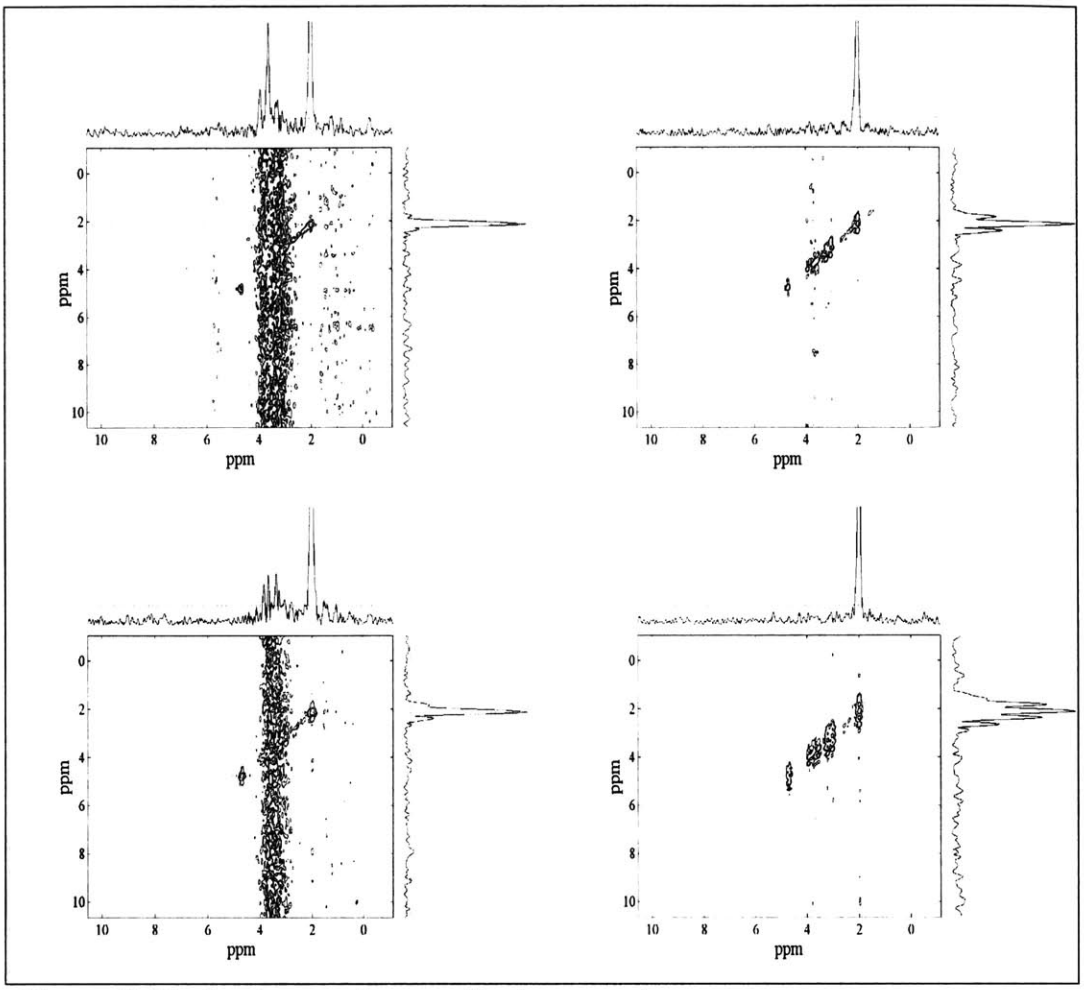

Figure 2-16: *In vivo* crusher gradient comparison

In vivo spectra were acquired from brain tissue with VOSY-HOHAHA (top row) and VOSY-COSY (bottom row). All spectra were weighted by a $\pi/8$ shifted sine squared bell. The coherence selection gradients were 2 milliseconds for the spectra in the left column and 6 milliseconds for the spectra in the right column. The horizontal and vertical traces were taken through the NAA methyl resonance.

To illustrate the need to use 6 millisecond coherence selection gradients for water suppression, *in vivo* human brain spectra were acquired with VOSY-COSY and VOSY-HOHAHA. 2D brain tissue spectra were obtained from a 59-mL voxel with the coherence selection gradients at 2ms and 6ms. The spectra were acquired with 96 t_1 increments with a 1.8-second repetition time. The optimum four-step phase cycle was used when acquiring the data, which resulted in a total acquisition time of 12 minutes per spectrum. Acquisition times were kept short since additional signal averaging would not have a drastic effect on the degree of water suppression. Figure 2-16 shows the spectra obtained with VOSY-HOHAHA and VOSY-COSY with a coherence selection gradient

duration at 2ms and 6ms.. The t_1 noise in the spectra acquired with 2ms coherence selection gradients is unacceptable for *in vivo* spectroscopy. The vertical traces reveal an artifact of unknown origin when the coherence selection gradients were increased to 6ms. This artifact also appeared in VOLT spectra when the coherence selection gradients were increased to 6 milliseconds (spectra not shown). The artifact may be due to eddy currents since it is universal across all three experiments at that gradient timing.

To determine the sensitivity of magnitude correlation experiments, *in vivo* human brain spectra were acquired from a 59 mL voxel with the coherence selection gradients at 2ms for VOLT and 6ms for VOSY-HOHAHA and VOSY-COSY. The optimum four-step phase cycle was used when acquiring the data. The spectra were acquired with 96 t_1 increments with a 1.8-second repetition time. Two phase cycles were averaged together for each t_1 increment, for a total of eight acquisitions per t_1 increment. Total acquisition time for each experiment was 23 minutes. Figure 2-17 shows spectra obtained with VOLT, VOSY-HOHAHA, and VOSY-COSY. As demonstrated earlier, VOLT has superior water suppression compared to both VOSY-HOHAHA and VOSY-COSY. However, the sensitivity of all three experiments fails to convincingly reveal expected correlations. This is due to the inclusion of the dispersive line shape in the unweighted spectra and sensitivity losses due to apodization in the apodized spectra.

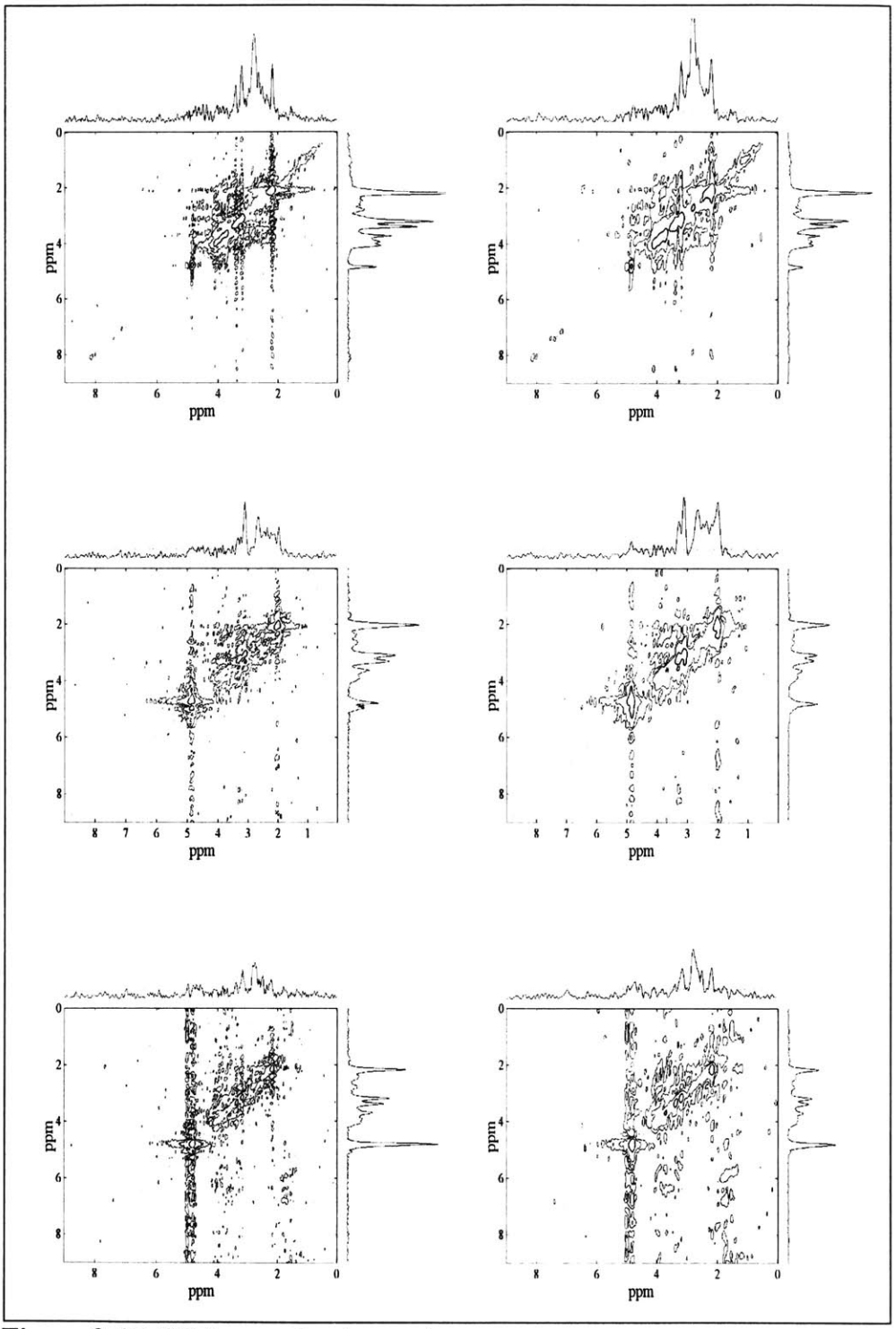

Figure 2-17: 2D human brain spectra

2D brain spectra obtained from a 59 mL voxel with VOLT (top row) , VOSY-HOHAHA (middle row), and VOSY-HOHAHA (bottom row). The unweighted and weighted spectra are displayed in the left and right columns, respectively. A $\pi/8$ shifted sine squared bell was used for the weighting function of all three pulse sequences.

2.6 Discussion

The improved sensitivity of the correlation peaks of VOSY-HOHAHA and VOLT compared to VOSY-COSY is apparent from inspection of the unweighted human bone marrow data in Figure 2-10. In the experimental design, the acquisition time in t_1 was deliberately kept at 128 ms, which is 1/J for a typical coupling value of 7.8 Hz. The mixing times of the VOLT and VOSY-HOHAHA experiments was held as close to 1/(2J) as possible, i.e. 64 and 72 ms respectively. The mixing times were not identical as WALTZ-4 and MLEV-17 were used due to the superior performance of these schemes for mixing of longitudinal polarization and transverse coherence, respectively. The difference in mixing times resulted from a desire for the RF field strength of both mixing schemes to be the same. Accounting for the different mixing times, the performance of VOLT, VOSY-COSY and VOSY-HOHAHA is comparable in terms of cross peak signal intensity prior to apodization when the mixing times are similar. The problem with mix mode line shape spectroscopy is the need to display the spectra in magnitude mode. Clearly, if the line shape could be displayed in absorptive mode without the use of severe apodization functions the sensitivity advantage of in-phase coherence transfer methods could be realized.

The ability of in-phase coherence transfer to drive maximum coherence, independent of the t_1 interval, allows for shorter acquisition times in t_1. The optimal resolution per t_1 acquisition time appears to be in the range of 48 to 64 t_1 increments for a spectral width of 750 Hz. This is clear in the corn oil and bone marrow data, but is less convincing in the brain spectra. This is simply due to the fact that the sensitivity of the methods is too poor to allow good quality brain spectra to be acquired in a reasonable amount of time on a reasonable volume size. In Chapter 3, a new method of obtaining absorptive mode spectra will be presented which obtains quality 2D spectra of the brain in under 24 minutes on similar volumes.

The form of VOLT allows for stable water suppression due to the placement of the evolution time prior to the final CHESS packet. This allows for consistent preparation of the z-component of the water prior to the final $\pi/2$ pulse in the sequence. This added stability is essential for the absorptive mode experiments.

The mixing of longitudinal polarization is known to be suboptimal under a WALTZ mixing scheme. Flip-flop based sequences such as FLOPSY-8 allow more efficient coherence transfer (29,30), but their rather long cycle times do not allow a reasonable comparison with MLEV-17 (50 ms vs. 36 or 72 ms). Despite this, the use of WALTZ was adequate for demonstration of the desirable features of in-phase coherence transfer using VOLT. A comparison of WALTZ to FLOPSY will be undertaken in Chapter 3.

The investigations of phase cycling and crusher gradient strength requirements reveal that a likely decrease in sensitivity of VOSY-COSY and VOSY-HOHAHA results from the 6 ms gradient crushing required for adequate water suppression stability. The lines shape disturbance at the longer crushing times are of uncertain origin. Artifacts induced by vibration are unlikely, since placement of the phantom upon a vibration isolation cantilever did not remove the artifact. The artifact may be due to eddy currents since it is universal across all three experiments at that gradient timing.

Chapter 3 : Absorptive Mode Spectroscopy

3.1 Introduction

In Chapter 2, in-phase coherence transfer methods were shown to have a sensitivity advantage over anti-phase coherence transfer methods. However, the use of coherence transfer selection gradients in VOLT, and the VOSY-based experiments introduces an unavoidable mixing of absorptive and dispersive line shape. The removal of the dispersive component by a severe apodization function negates the sensitivity advantage obtained with in-phase coherence transfer. To retain the sensitivity advantage of in-phase coherence transfer, the dispersive component must be removed from the spectra without the use of apodization functions; this may be accomplished if both coherence pathways are acquired.

As discussed by Brereton, et. al. (8), the VOSY-HOHAHA experiment is capable of acquiring both N and P type coherence pathways with some minor modifications. While possible, in light of VOLT's superior water suppression, the experiments developed in this chapter will mix longitudinal magnetization, allowing the variable t_1 increment to be placed between the two periods of water suppression. This approach yields the most stable and sensitive 2D chemical shift correlation experiment of all proposed methods.

The form of the experiment is that of a z-filtered TOCSY experiment followed by a PRESS sequence for volume localization. This approach allows both coherence pathways to be acquired in an amplitude-modulated data set. A second amplitude-modulated data set is acquired by shifting the phase of the first pulse by 90 degrees. Applying a hypercomplex Fourier Transform (FT) to these two amplitude-modulated data sets, as described by States, Haberkorn and Ruben (31), results in absorptive mode spectra. A side benefit of the z-filtered form of the experiment is the ability to suppress the water signal by at least four orders of magnitude. The z-filtered absorptive mode

experiment developed as part of this thesis obtains high quality 2D spectra from the human brain in 24 minutes from a 59 milliliter volume.

In the previous chapter, the isotropic mixing scheme, WALTZ-4, transferred coherence among coupled spins in the VOLT experiment. However, WALTZ-4 is not the optimal choice for longitudinal polarization transfer. Simulations and experimental data of **FL**ip-fl**OP** **S**pectrosco**Y** (FLOPSY) (29,30), a more efficient isotropic mixing scheme, will be presented in this chapter.

3.2 Experimental Design

A new pulse sequence capable of obtaining volume localized near absorptive line shape in both dimensions is shown in Figure 3-1. (The VOLT pulse sequence is reprinted in Figure 3-2 for the reader's convenience.) Following application of the first CHESS packet, a hard $\pi/2$ pulse excites the spins. These spins then evolve under their chemical shift and scalar coupling during the evolution period, t_1. The spins are then returned to the z-axis by the second hard $\pi/2$ pulse except for a small amount of orthogonal anti-phase coherence, which evolved during the evolution period. These orthogonal terms are purged by the z-filter (32). The resulting z-magnetization is amplitude modulated as a function of t_1. The central π pulse is of practical utility because of the unacceptable amount of first order phase error during the relatively long hard pulses (240 μs $\pi/2$ pulse). This π pulse refocuses the chemical shift during these delays allowing a true first $t_1=0$ increment. This pulse sequence has been named REVOLT, **RE**focused **VO**lume Localized **T**OCSY, to indicate the refocusing of the chemical shift.

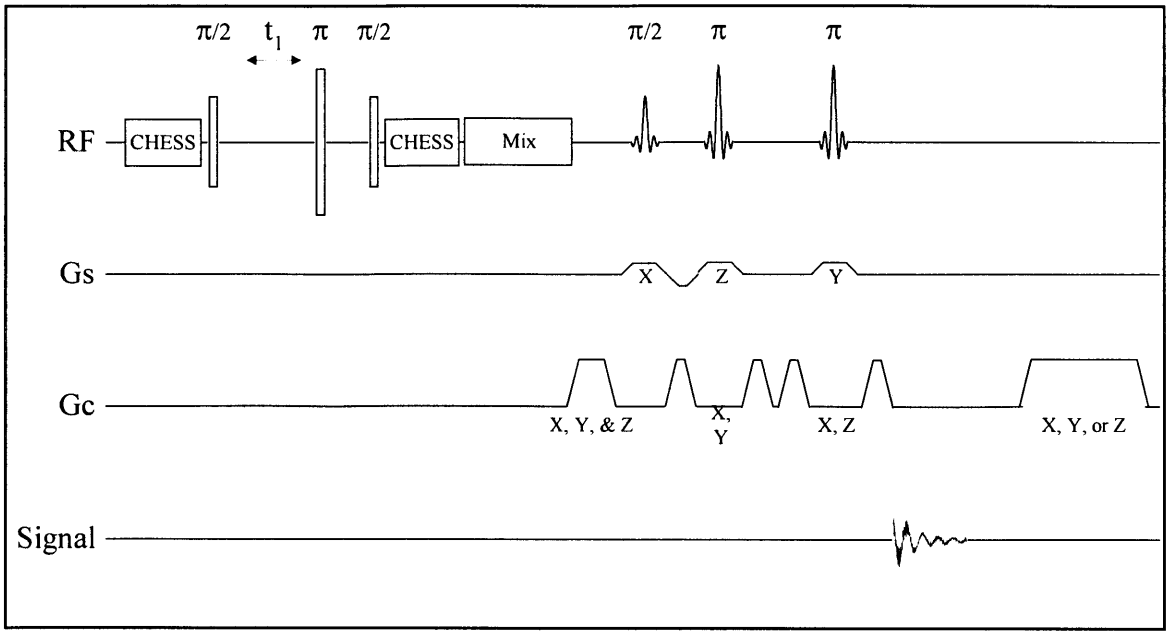

Figure Figure 3-1: REVOLT pulse diagram.

REVOLT is a modified VOLT experiment. The insertion of the π pulses allows both coherence pathways to be maintained throughout the experiment. This allows near absorptive mode spectra in both dimensions to be reconstructed using the States, Haberkorn, Rueben(31) method. Volume localization is achieved with a PRESS sequence after the isotropic mixing.

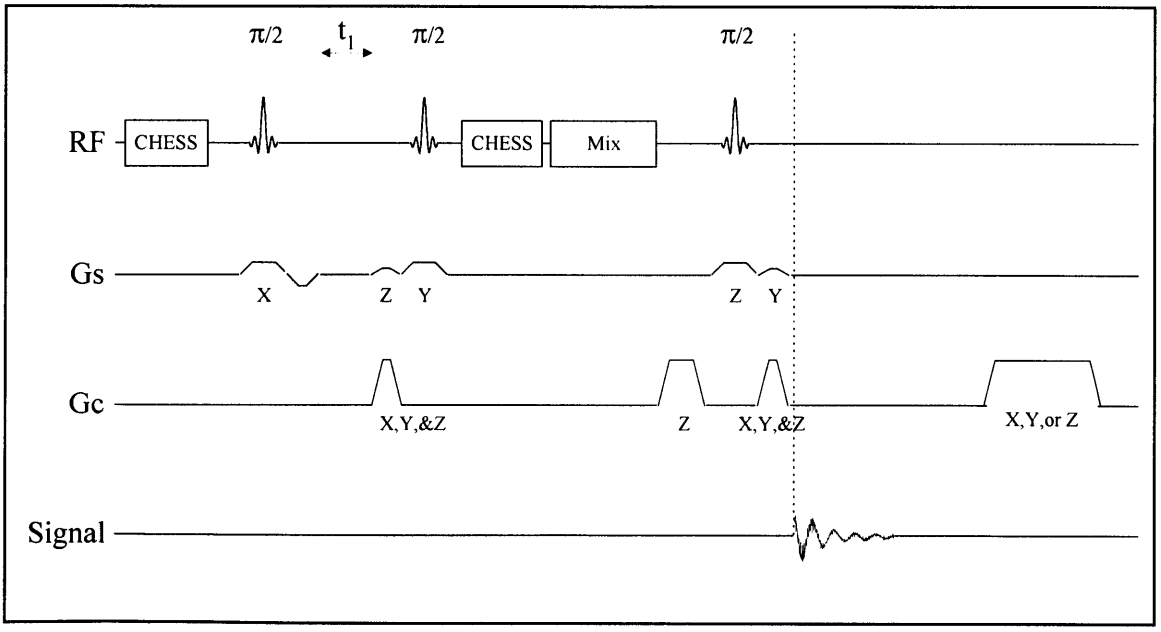

Figure 3-2: VOLT pulse diagram.

VOLT is a modified DRY-STEAM experiment. Coherence transfer is achieved by isotropic mixing after the second CHESS packet. The t_1 increment is located between the first and the second π/2 pulse. Slice select gradients are drawn on the Gs channel and their direction is as indicated. The slice select refocusing gradients of the second and third π/2 pulses require that the N-coherence pathway be selected. Gradients on the Gc channel crushes the outer volume signal. The last crusher gradient is rotated among the X,Y, and Z for each t_1 increment.

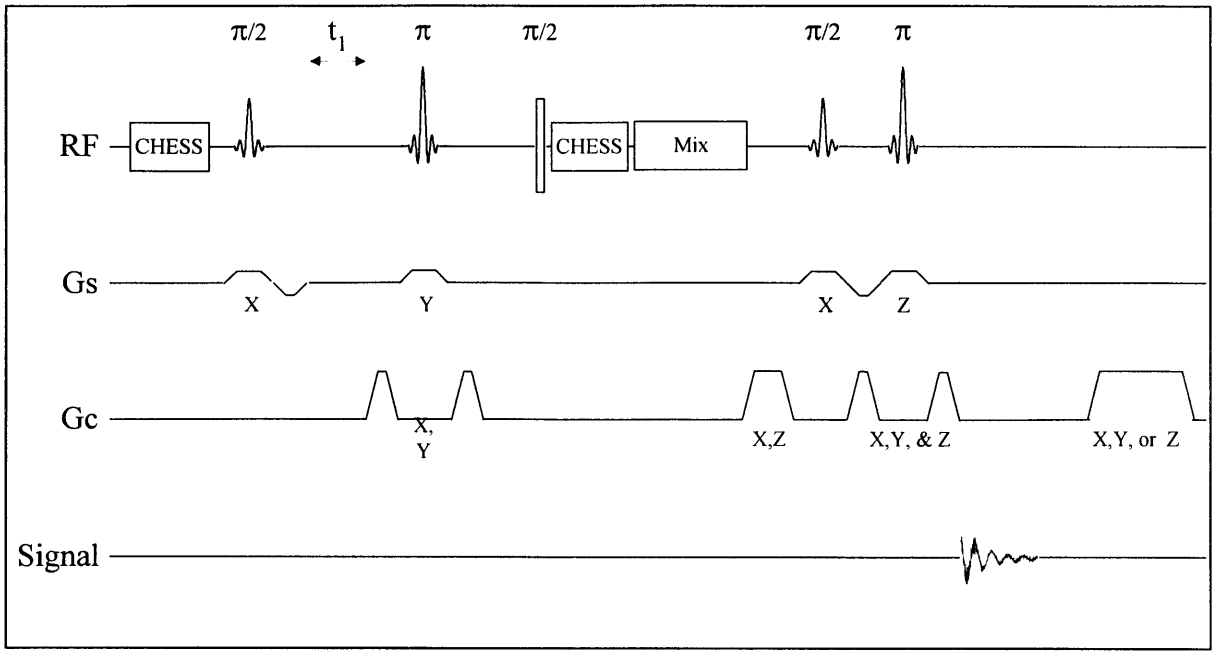

Figure 3-3: Q-REVOLT pulse diagram.
Q-REVOLT is a modified REVOLT experiment. The slice selective pulses on both sides of the isotropic mixing scheme achieve volume localization. Q-REVOLT reduces the phase distortions due to scalar coupling by minimizing the time between the third $\pi/2$ pulse and acquisition. Outer volume signal generated from the last spin echo is removed by phase alternation of the first $\pi/2$ pulse.

A modified REVOLT experiment is shown in Figure 3-3. To minimize phase errors due to scalar coupling, the time between the third $\pi/2$ pulse and acquisition is minimized. This is accomplished by performing volume localization both before and after the isotropic mixing scheme, thus eliminating the need for the last slice selective π pulse in the standard PRESS. This experiment has been dubbed Q-REVOLT for Quick REVOLT, since the time between the third $\pi/2$ pulse and acquisition is shorter than in REVOLT. The tradeoff is the unavoidable formation of a spin echo from the last two pulses, which excites outer volume signal. Phase cycling is necessary to remove the unwanted outer volume signal. As will be shown later in this chapter, single shot volume localization is necessary for *in vivo* spectroscopy. In addition, the increased delay time between the first and second $\pi/2$ pulse results in a loss of sensitivity due to T_2 relaxation. While Q-REVOLT is inferior to REVOLT, Q-REVOLT is included in this thesis because it demonstrates the instabilities introduced by non-single shot experiments.

An additional feature of the five experiments presented in this thesis (VOLT, VOSY-HOHAHA, VOSY-COSY, REVOLT, and Q-REVOLT) is the recovery of signal

from coupled resonances bleached by the water suppression. These resonances are recovered because coherence is transferred from spins that are unaffected by the water suppression to spins that are completely suppressed. The recovery of these bleached resonances is only possible if the water suppression occurs before the mixing pulse. These recovered resonances are only observable *in vivo* with REVOLT due to its absorptive mode line shape and improved sensitivity. Even though Q-REVOLT acquires absorptive mode spectra, it is unable to observe these recovered resonances because of inferior water suppression and t_1 noise.

3.3 Theory

REVOLT does not use coherence selection gradients to obtain frequency discrimination in the indirect dimension. The product operator analysis of VOLT in the previous chapter provided insight into VOLT's sensitivity and resolution limitations. A similar analysis is done for REVOLT, which is identical to VOLT except for the absence of coherence selection gradients. Therefore, the product operator analysis of VOLT may be reused for REVOLT with the area of the coherence selection gradients, G, set equal to zero:

$$\begin{aligned}\sigma_6 = & \frac{i}{4}\left(\frac{e^{-it_1\Omega_1}+e^{+it_1\Omega_1}}{2}\right)\cos(\pi J t_1)\left(1+\cos(2\pi J \tau_{mix})\right) I_{1+} \\ & - \frac{i}{4}\left(\frac{e^{-it_1\Omega_1}+e^{+it_1\Omega_1}}{2}\right)\cos(\pi J t_1)\left(1+\cos(2\pi J \tau_{mix})\right) I_{1-} \\ & + \frac{i}{4}\left(\frac{e^{-it_1\Omega_1}+e^{+it_1\Omega_1}}{2}\right)\cos(\pi J t_1)\left(1-\cos(2\pi J \tau_{mix})\right) I_{2+} \\ & - \frac{i}{4}\left(\frac{e^{-it_1\Omega_1}+e^{+it_1\Omega_1}}{2}\right)\cos(\pi J t_1)\left(1-\cos(2\pi J \tau_{mix})\right) I_{2-}\end{aligned} \qquad 3.1$$

The spins then evolve under their chemical shifts and scalar couplings during the detection period, t_2, yielding,

$$\sigma_6 = -\frac{i}{4}\left(\frac{e^{-it_1\Omega_1}+e^{+it_1\Omega_1}}{2}\right)\cos(\pi J t_1)(1+\cos(2\pi J \tau_{mix}))$$
$$\left(e^{-it_2\Omega_1}(\cos(\pi J t_2)I_{1-}+2\sin(\pi J t_2)I_{1-}I_{2z})\right) \qquad \textbf{3.2}$$
$$-\frac{i}{4}\left(\frac{e^{-it_1\Omega_1}+e^{+it_1\Omega_1}}{2}\right)\cos(\pi J t_1)(1-\cos(2\pi J \tau_{mix}))$$
$$\left(e^{-it_2\Omega_2}(\cos(\pi J t_2)I_{2-}+2\sin(\pi J t_2)I_{2-}I_{1z})\right).$$

Since both coherence pathways are maintained, the sensitivity is immediately improved by a square root of two for the t_1=0 increment. As the t_1 increment is increased on subsequent scans, the z-magnetization will acquire an amplitude modulation due to the chemical shift. The hypercomplex method of States, Haberkorn, and Ruben (31) uses two amplitude modulated data sets to recover the spins' precession frequencies in the indirect spectral dimension and achieve pure absorptive mode line shapes in both dimensions. This will be demonstrated for an uncoupled spin system (i.e. J = 0). Under this simplification Equation 3.2 reduces to,

$$s_c(t_1,t_2) = \frac{1}{2}\left(\frac{e^{-it_1\Omega_1}+e^{+it_1\Omega_1}}{2}\right)e^{-it_2\Omega_1}\,r(t_1,t_2)$$
$$= \frac{1}{2}\cos(t_1\Omega_1)e^{-it_2\Omega_1}\,r(t_1,t_2) \qquad , \qquad \textbf{3.3}$$

where $s(t_1,t_2)$ is the detected signal of an uncoupled spin, relaxation has been reintroduced with the decay function $r(t_1,t_2)$, and the phase of the receiver has been adjusted to remove a factor of -i. Taking the complex Fourier transform of the signal in both dimensions yields,

$$S(\omega_1,\omega_2) = \frac{1}{2}\left(A(\omega_1^+,\Omega_1)+iD(\omega_1^+,\Omega_1)-A(\omega_1^-,\Omega_1)-iD(\omega_1^-,\Omega_1)\right)$$
$$\left(A(\omega_2,\Omega_2)+iD(\omega_2,\Omega_2)\right) \qquad , \qquad \textbf{3.4}$$

where the superscripts indicate an inability to determine the sign of the resonant frequency in the indirect dimension. In addition, this 2D spectrum has phase twisted line shapes. In order to obtain pure absorptive lines in both dimensions, a second data set

phase shifted from the first by 90 degrees must be acquired and stored separately. This is accomplished by incrementing the phase of the first $\pi/2$ pulse by 90 degrees yielding a sine modulated data set,

$$\begin{aligned} s_s(t_1,t_2) &= \frac{1}{2}\left(\frac{e^{-it_1\Omega_1} - e^{+it_1\Omega_1}}{2i}\right)e^{-it_2\Omega_1}\, r(t_1,t_2) \\ &= \frac{1}{2}\sin s(t_1\,\Omega_1)e^{-it_2\Omega_1}\, r(t_1,t_2) \end{aligned} \qquad \textbf{3.5}$$

Taking the Fourier transform of Equations 3.3 and 3.5 with respect to t_2 results in two amplitude modulated data sets,

$$\begin{aligned} s_c(t_1,\omega_2) &= \frac{1}{2}\cos(t_1\,\Omega_1)r(t_1)(A_2 + i\,D_2), \\ s_s(t_1,\omega_2) &= \frac{1}{2}\sin(t_1\,\Omega_1)r(t_1)(A_2 + i\,D_2)\ . \end{aligned} \qquad \textbf{3.6}$$

Discarding the imaginary component from both signals and combining them yields,

$$\mathrm{Re}\{s_c(t_1,\omega_2) + is_s(t_1,\omega_2)\} = (\cos(t_1\,\Omega_1) + i\sin(t_1\,\Omega_1))r(t_1)(A_2) \qquad \textbf{3.7}$$

Finally, taking the Fourier transform in the indirect dimension and discarding the real component produces a pure absorptive line shape in both dimensions,

$$\begin{aligned} S(\omega_1,\omega_2) &= \mathrm{Im}\{(A_1 + i\,D_1)A_2\} \\ &= A_1A_2 \end{aligned} \qquad \textbf{3.8}$$

The advantage of retaining only the absorptive component is seen in Figure 3-4. The full width eighth maximum is 3 times larger when the dispersive component is included in the line shape.

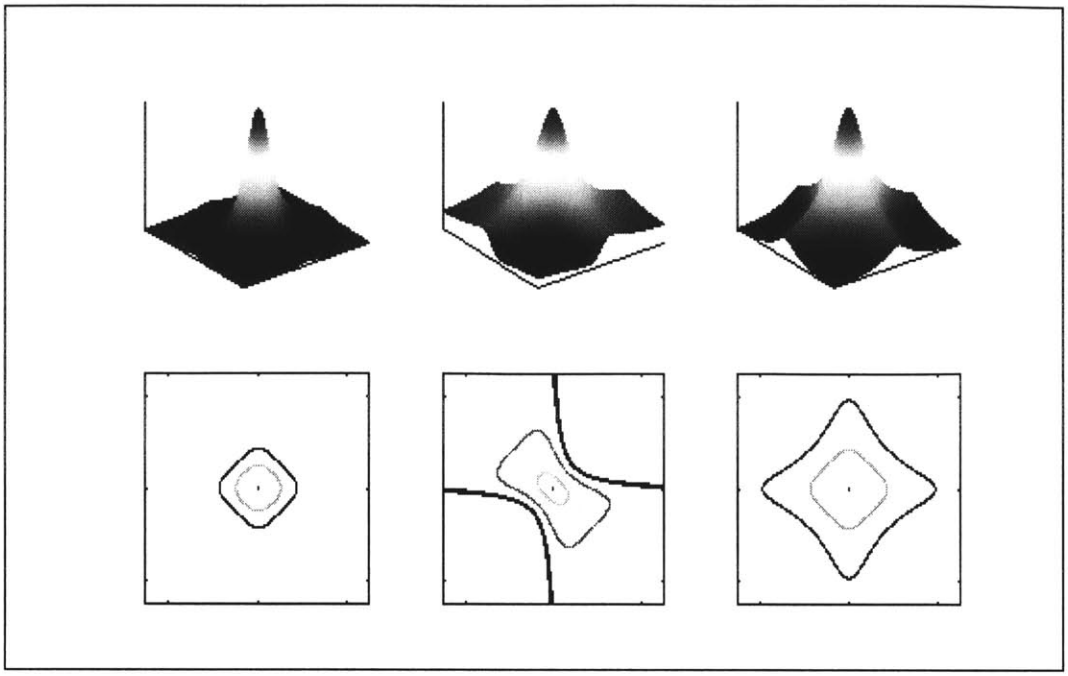

Figure 3-4: Two-Dimensional Line Shapes
Pure absorptive line shape in both dimensions (left column), pure dispersive line shape (middle column), and magnitude calculated line shape (right column). All contours are plotted at the same level in the positive contour plots.

3.4 Methods

Experiments were conducted under identical conditions as described in the Methods section of Chapter 2 with the exception of the isotropic mixing scheme. An isotropic mixing scheme based on WALTZ is not optimum for mixing longitudinal polarization. This will be shown experimentally by comparing the coherence transfer obtained with WALTZ-4 to FLOPSY-8. Both isotropic mixing schemes used a 463 Hz B_1 field, which resulted in a isotropic mixing time of 48.0 milliseconds and 50.9 milliseconds for WALTZ-4 and FLOPSY-8, respectively.

3.5 Results

3.5.1 Corn Oil Experiments

To confirm that spectra acquired with REVOLT and Q-REVOLT are not contaminated by outer volume signal, voxel projections were obtained from the corn oil phantom and are shown in Figure 3-5. Each projection was acquired with phase cycling and has been normalized to unity. The projections from the three pulse sequences were superimposed on each other along the corresponding read out directions. The superposition of these projections illustrates that all three pulse sequences are exciting the

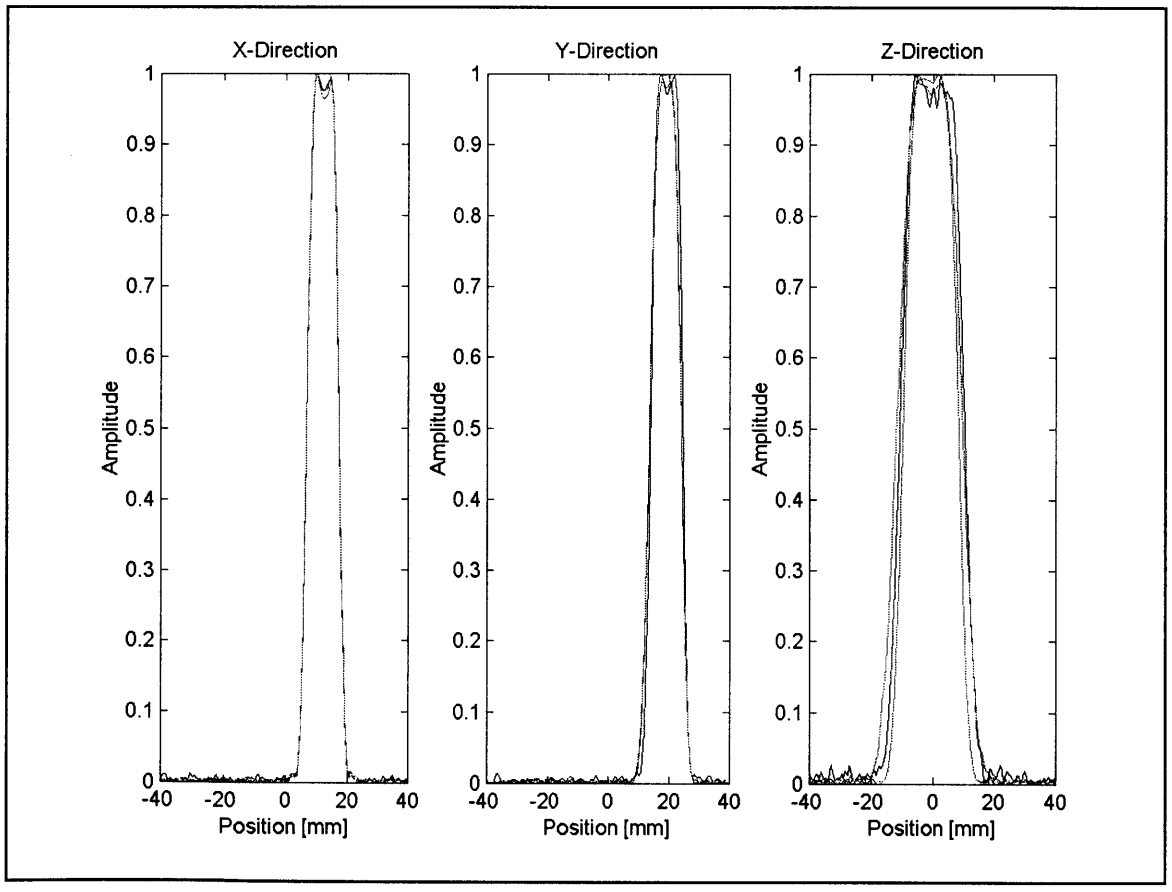

Figure 3-5: Overlapping normalized projections.
Voxel projections were obtained along X, Y, and Z directions for each pulse sequence with phase cycling of the first $\pi/2$ pulse by 180 degrees. The projections from VOLT, REVOLT, and Q-REVOLT have been overlayed to illustrate that all three sequences excite similar voxels.

same voxel of interest in both size and location. The width of each projection was determined by measuring it's Full Width Half Maximum (FWHM). The X and Y FHWM projections were measured at 11.8 millimeters and are identical for all three-pulse sequences. The width of Q-REVOLT at 19.6 millimeters is 2.9 millimeters less than either VOLT or REVOLT. These projections reveal that spectra acquired with all three pulse sequences are not contaminated with outer volume signal.

Plotting the projections separately reveals the potential sensitivity of VOLT, REVOLT, and Q-REVOLT (Figure 3-6). REVOLT projections have been normalized and are used as reference for each axis. The excitation profiles of VOLT are approximately half that of REVOLT. The VOLT experiment, since it is a modified DRY-STEAM experiment, only retains half of the available magnetization for t_1=0. Both REVOLT and Q-REVOLT refocus the lost magnetization, thereby, doubling the available signal contained in the voxel of interest. Q-REVOLT projection profiles are slightly less than that of REVOLT as a result of relaxation during the extra time between the first and second $\pi/2$ pulse.

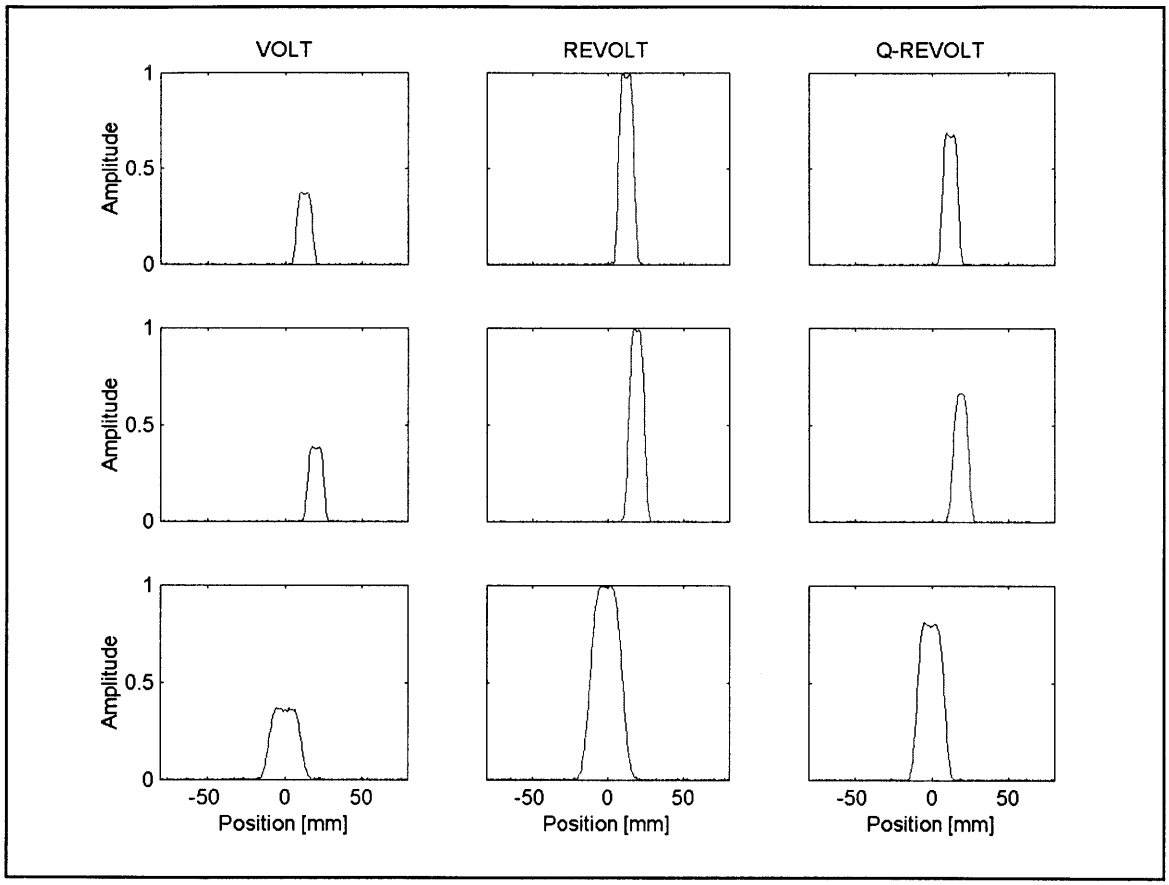

Figure 3-6: Voxel projections obtained with phase cycling.
These voxel projections are identical to 3-5 except for the normalization. The projections have been normalized to the REVOLT profile along a given direction. The X, Y, and Z direction are plotted along the first row, second row, and third row, respectively.

To determine if an experiment is compatible with single shot acquisition, the projections were acquired without phase cycling. The excitation profiles of VOLT and REVOLT are identical to their corresponding phase cycled projections, which is consistent with single shot volume localization. Q-REVOLT, however, does not obtain single shot volume localization. The last $\pi/2$ and π pulse form a spin echo with the outer volume signal along the Y direction. Other combinations of slice selection were investigated, but the choice of slice select gradient combination used for these studies gave the minimal amount of outer volume echo formation. The outer volume signal and the resulting distortion in the X and Z directions are effectively removed by phase cycling. As will be demonstrated later in the Q-REVOLT water suppression experiments,

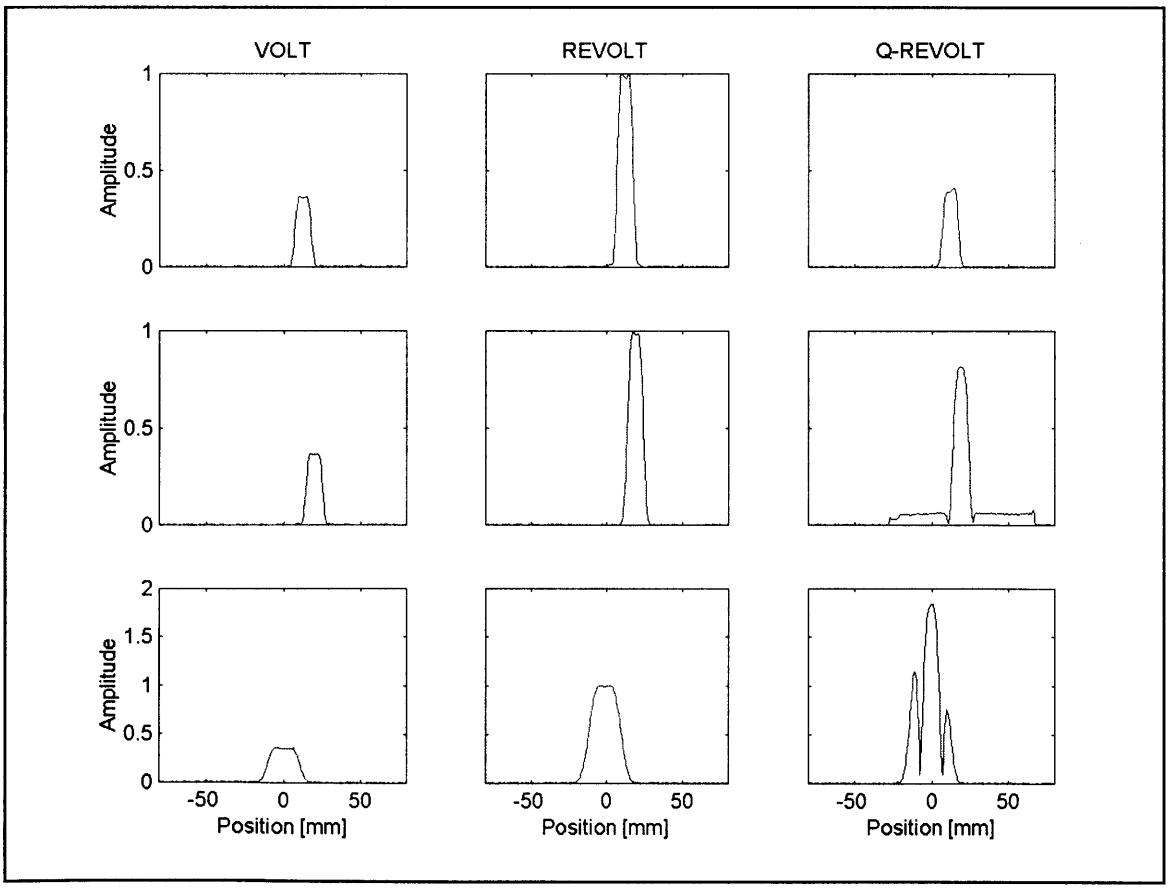

Figure 3-7: Voxel projections obtained without phase cycling.
Voxel projections obtained without phase cycling. The projections have been normalized to the REVOLT profile along a given direction. The X, Y, and Z direction are plotted along the first row, second row, and third row, respectively. The scaling of the amplitude along the Z-direction (third row) has been plotted from 0 to 2 to accommodate the outer volume signal obtained with Q-REVOLT.

single shot volume localization is essential for water suppression stability. The water suppression achieved with Q-REVOLT is unacceptable for *in vivo* applications, and therefore, such experiments were not performed.

Previous VOLT experiments used WALTZ-4 for coherence transfer. WALTZ-4 has been shown to be an inefficient method of coherence transfer for high field spectroscopy. Many alternative methods for isotropic mixing exist: WALTZ (33), MLEV (34), and FLOPSY (29,30). Among these, FLOPSY has been optimized to maximize longitudinal coherence transfer. Figure 3-8 plots the expected coherence transfer efficiency for WALTZ-4 and FLOPSY-8. The high field simulation shows that FLOPSY-8 obtains almost 100 percent coherence transfer at 70 ms. WALTZ-4 only obtains a maximum of 20 percent longitudinal coherence transfer. At low fields, the coherence transfer efficiency for a simple AX spin system becomes degenerate.

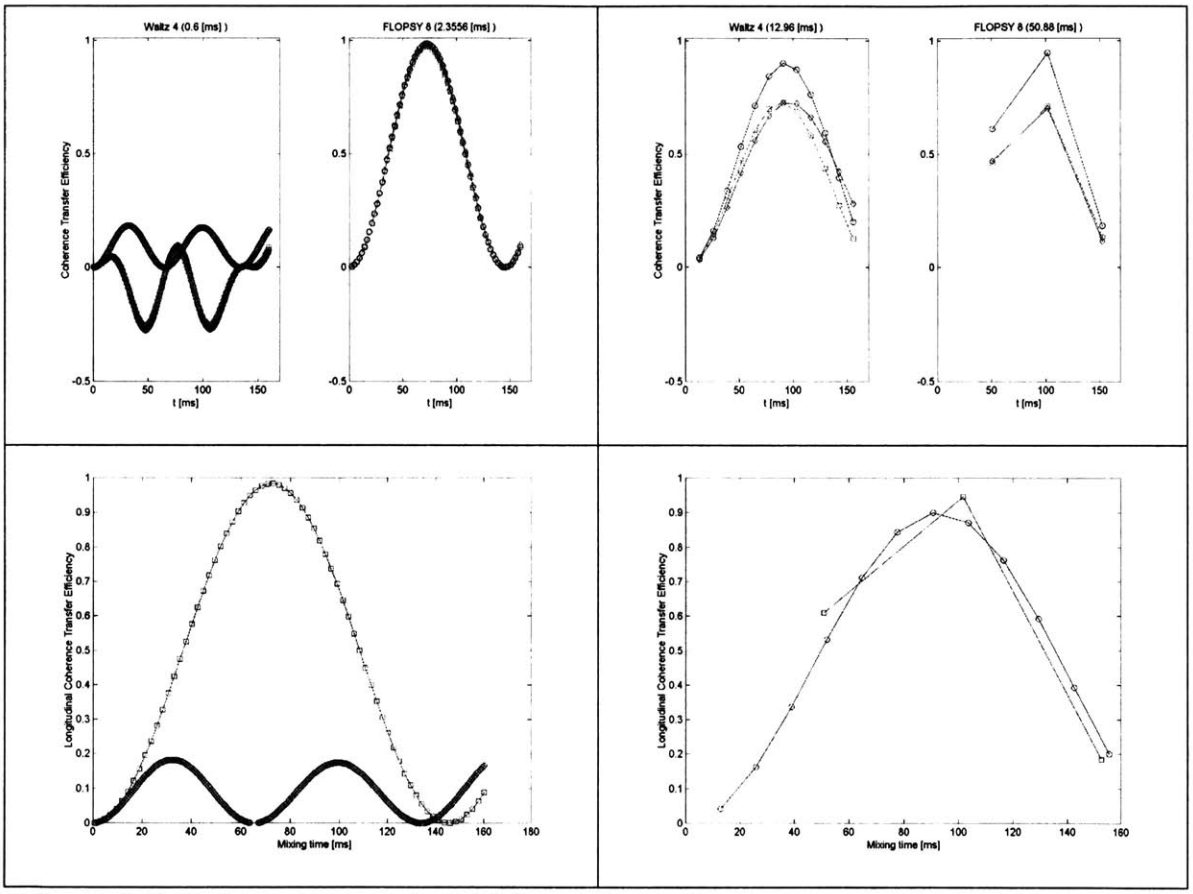

Figure 3-8: Coherence transfer efficiency simulation.

The WALTZ-4 and FLOPSY-8 isotropic mixing schemes were simulated for an 11 Tesla high field spectrometer (left column) and 1.5 Tesla low field clinical imaging magnet (right column). The B_1 field strength for the high field and low field simulations were 10kHz and 462 Hz, respectively. The I and S spin were assumed to be 3 ppm apart with a 7 Hertz J coupling. The transmitter was assumed to be located in between the two spins and relaxation was ignored. The coherence transfer efficiency of In to Sn is plotted in the top row as a function of the isotropic mixing time, where n may be either X (squares), Y(diamonds), or Z (circles). The bottom row is a comparison of WALTZ-4 (circles) and FLOPSY-8 (squares).

Isotropic mixing schemes like WALTZ and FLOPSY are a series of phase modulated hard pulses. These hard pulses act in combination with each other to increase the excitation bandwidth of the B_1 field and compensate for pulse imperfections. Because the number of hard pulses is fixed for a single isotropic mixing cycle, the isotropic mixing time is fixed for a given B_1 field strength. For example, the isotropic mixing time for a single cycle of WALTZ-4 and FLOPSY-8 with a B_1 field strength of 463 Hz is 12.96 ms and 50.88 ms, respectively. Isotropic mixing cycles may be concatenated together to increase the isotropic mixing time. For example, two, three, and four single cycles of WALTZ-4 would have an isotropic mixing time of 25.92ms, 38.88ms, and 51.84ms, respectively. This accounts for the poor time resolution of FLOPSY-8 in comparison to WALTZ-4, as seen in Figure 3-8. The low-field simulation of an AX spin system reveals that FLOPSY-8 does not provide a coherence transfer advantage over WALTZ-4. However, experience has shown that FLOPSY-8 does increase the coherence transfer efficiency for a variety of spin systems.

Figure 3-9 is a comparison of WALTZ-4 to FLOPSY-8 in corn oil. Sets of 2D spectra were acquired with VOLT for different isotropic mixing times using WALTZ-4 and FLOPSY-8. The amplitude of the diagonal vinyl peak, the a-d cross peak, and the a-f cross peaks are plotted as a function of the isotropic mixing time for WALTZ-4 and FLOPSY-8. The amplitude of the diagonal vinyl peak decreases monotonically as a function of isotropic mixing time. The coherence transfer into the a-d cross peak by either WALTZ-4 or FLOPSY-8 is essentially identical. The coherence transfer into the a-f cross peak reveals that FLOPSY-8 is approximately 100% superior to WALTZ-4 at 52 ms.

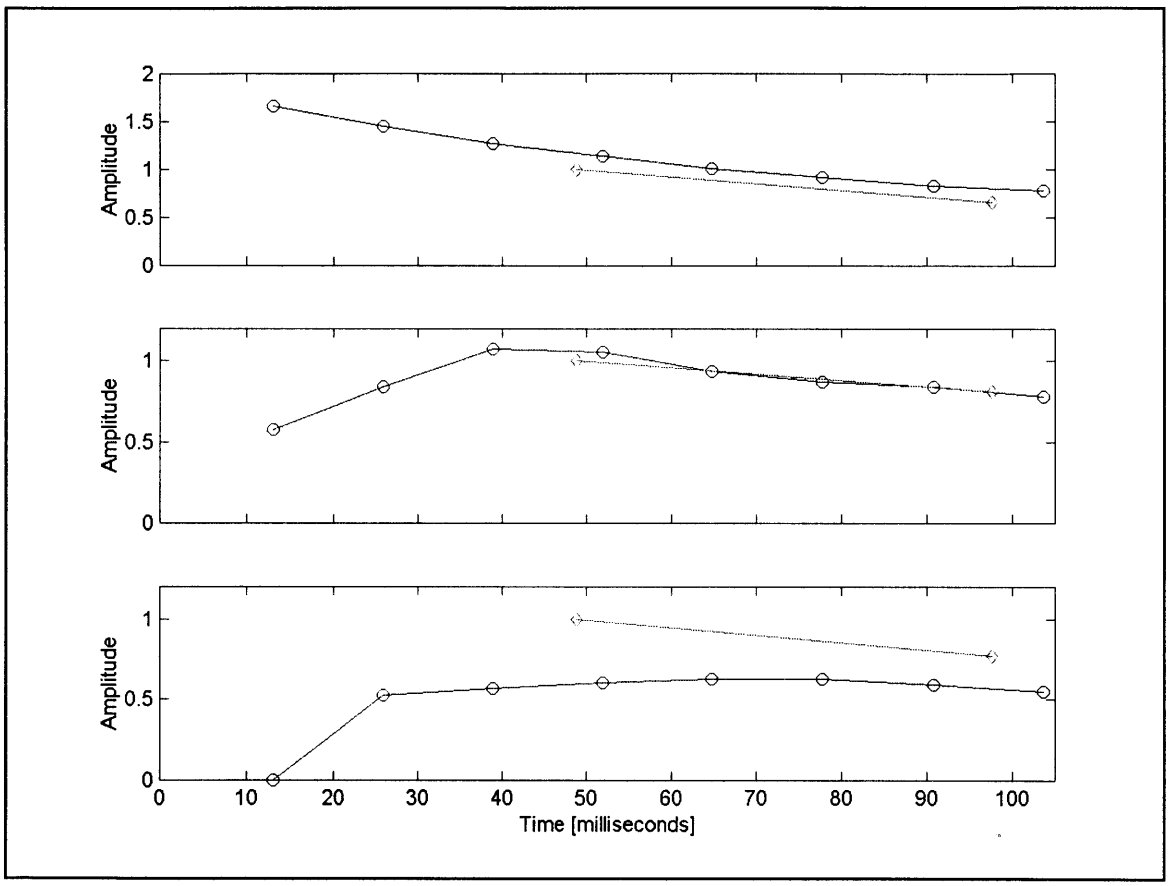

Figure 3-9: Coherence transfer efficiency of WALTZ-4 and FLOPSY-8.
Peak amplitudes of corn oil were plotted as a function of isotropic mixing time for WALTZ-4 (circles) and FLOPSY-8 (diamonds) . The vinyl diagonal peak is plotted in the top row, the a-d cross peak is plotted in the middle, and the a-f cross peak is plotted on the bottom.

For sensitivity and resolution comparisons, 2D corn oil spectra were obtained with VOLT, REVOLT, and Q-REVOLT and are displayed in Figure 3-10. The VOLT spectra are displayed in magnitude mode. Since REVOLT and Q-REVOLT maintain both N and P type coherence pathways, they are displayed in phase-sensitive absorptive mode. The contour levels for the unweighted spectra are identical in all three experiments. The contour levels for the apodized spectra are plotted at half the intensity of the unweighted spectra.

The advantages of absorptive mode line shape are clear from the unweighted spectra. The dispersive line shape contained in the VOLT spectra obscures the cross peaks of interest. These cross peaks are visible in the REVOLT and Q-REVOLT spectra. To remove the dispersive line shape in the VOLT spectra, a $\pi/8$ shifted sine square bell was applied in both dimensions. The removal of the dispersive, as was shown in the previous section, attenuates the cross peaks. The cross peak intensity of the apodized VOLT spectrum is approximately half the cross peak intensity of both REVOLT and Q-REVOLT apodized spectra. Since the dispersive line shape is not contained in the REVOLT or Q-REVOLT spectra, only mild apodization is necessary to enhance sensitivity.

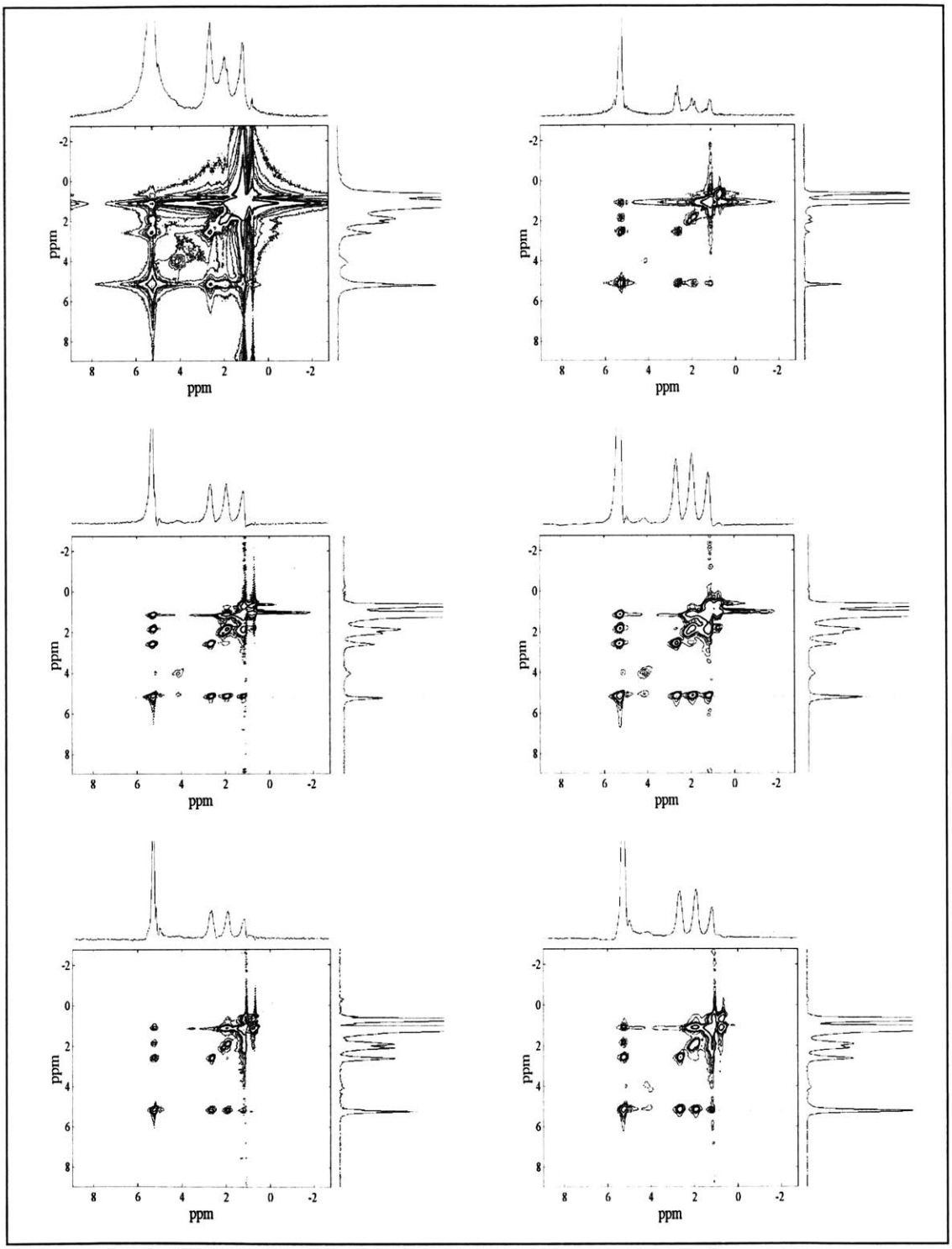

Figure 3-10: VOLT, REVOLT, & Q-REVOLT corn oil spectra.

VOLT (first row), REVOLT (second row), and Q-REVOLT (third row) corn oil spectra were obtained from a 3.1 mL voxel with phase cycling. The left column contains the unweighted spectra and the right column contains the apodized data. The VOLT spectrum was weighted with a $\pi/8$ degree shifted sine squared bell in both dimensions to remove the dispersive component. A Lorentz to Gauss apodization function (t_1:1,4; t_2:1,2) was applied to the REVOLT and Q-REVOLT spectra. The horizontal trace reveals the intensity of the vinyl cross peaks. The vertical trace shows the diagonal of each spectrum.

Axial peaks are minimized in volume localized 2D experiments by minimizing the time between the first excitation pulse and start of acquisition, and by using a single shot experiment. When a single shot experiment is not used, the axial peaks arise primarily from the unmodulated outer volume signal. To illustrate the importance of single shot volume localization for *in vivo* experiments, phase cycling experiments were conducted with VOLT, REVOLT, and Q-REVOLT. Two-dimensional spectra were obtained with and without phase cycling for each of the three pulse sequences. Figure 3-11 shows the weighted corn oil spectra without phase cycling (right column) and with phase cycling (left column). VOLT and REVOLT, since they are single shot volume localization experiments, have only small axial peaks contained at the edge of the spectra in the indirect dimension. The axial peaks of REVOLT are greater than the axial peaks of VOLT because REVOLT maintains both coherence pathways by having balanced gradients on both sides of the isotropic mixing scheme. Axial peaks generated by VOLT are effectively removed by the crusher gradient after the third $\pi/2$ pulse.

The signal at the edge of the spectrum, obtained with Q-REVOLT without phase cycling, contains both axial peaks and outer volume signal. Both of these contributions are easily removed with phase cycling. However, removing a large amount of signal with phase cycling is undesirable *in vivo*. Small instabilities, occurring between acquisitions, result in imperfect removal of the undesired signal. These instabilities are minor while acquiring spectra from a stationary phantom without water suppression. When phase cycling is required to remove the residual water signal from the outer volume, these instabilities result in t_1 noise, which obscure cross peaks.

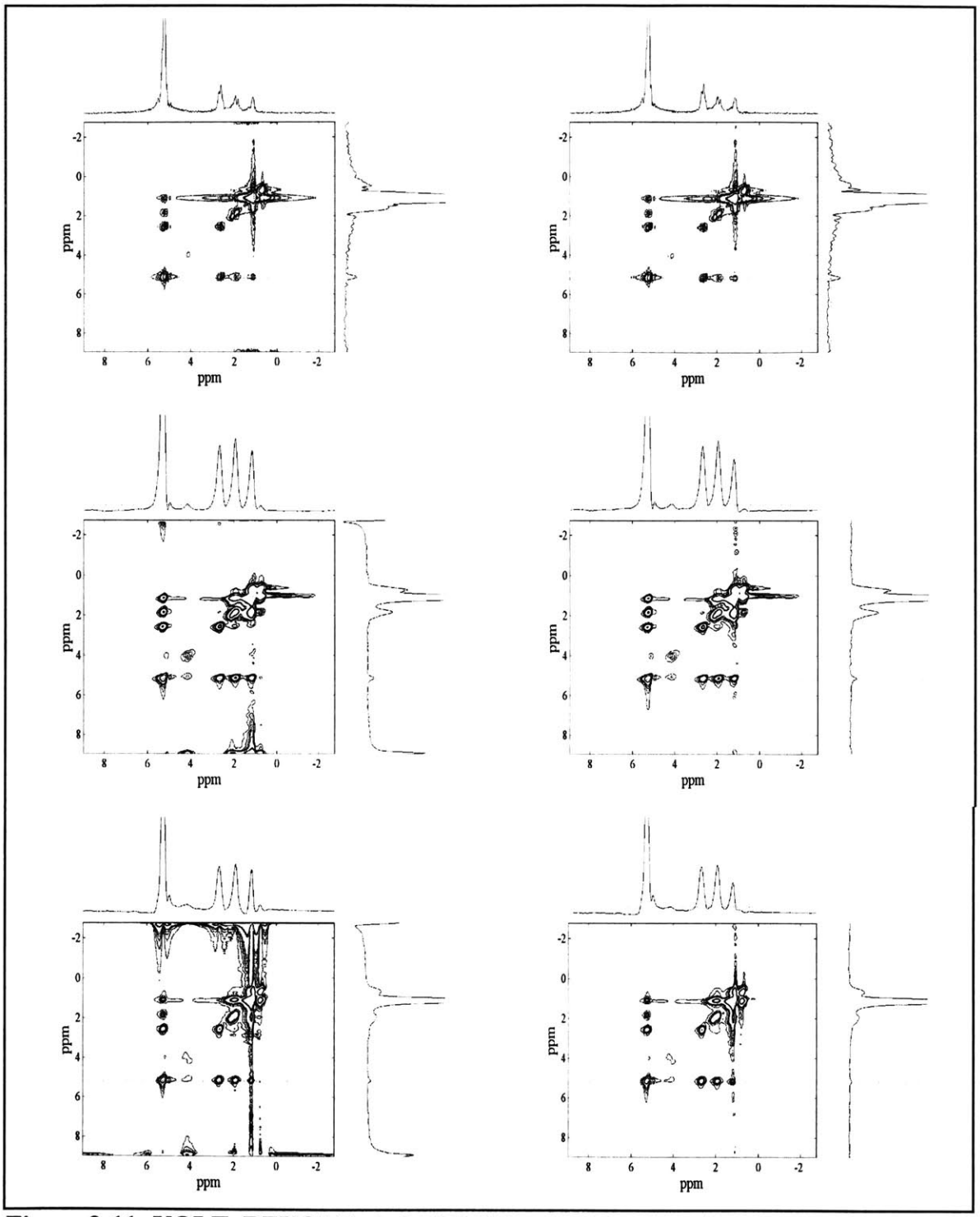

Figure 3-11: VOLT, REVOLT, & Q-REVOLT phase cycling experiments.
Phase cycling experiments were conducted with VOLT (top row), REVOLT (middle row), and Q-REVOLT (bottom row) on a corn oil phantom. Four acquisitions were acquired for each t_1 increment. The spectra in the left column were acquired without phase cycling. The spectra in the right column were acquired with a two step phase cycle of the first $\pi/2$ pulse. Identical weighting functions were applied to the data acquired with and without phase cycling. A shifted sine squared bell (t_1:$\pi i/8$; t_2:$\pi/8$) was applied to the VOLT spectra and a Lorentz to Gauss weighting function (t_1:1,5; t_2:1,2) was applied to the REVOLT and Q-REVOLT spectra.

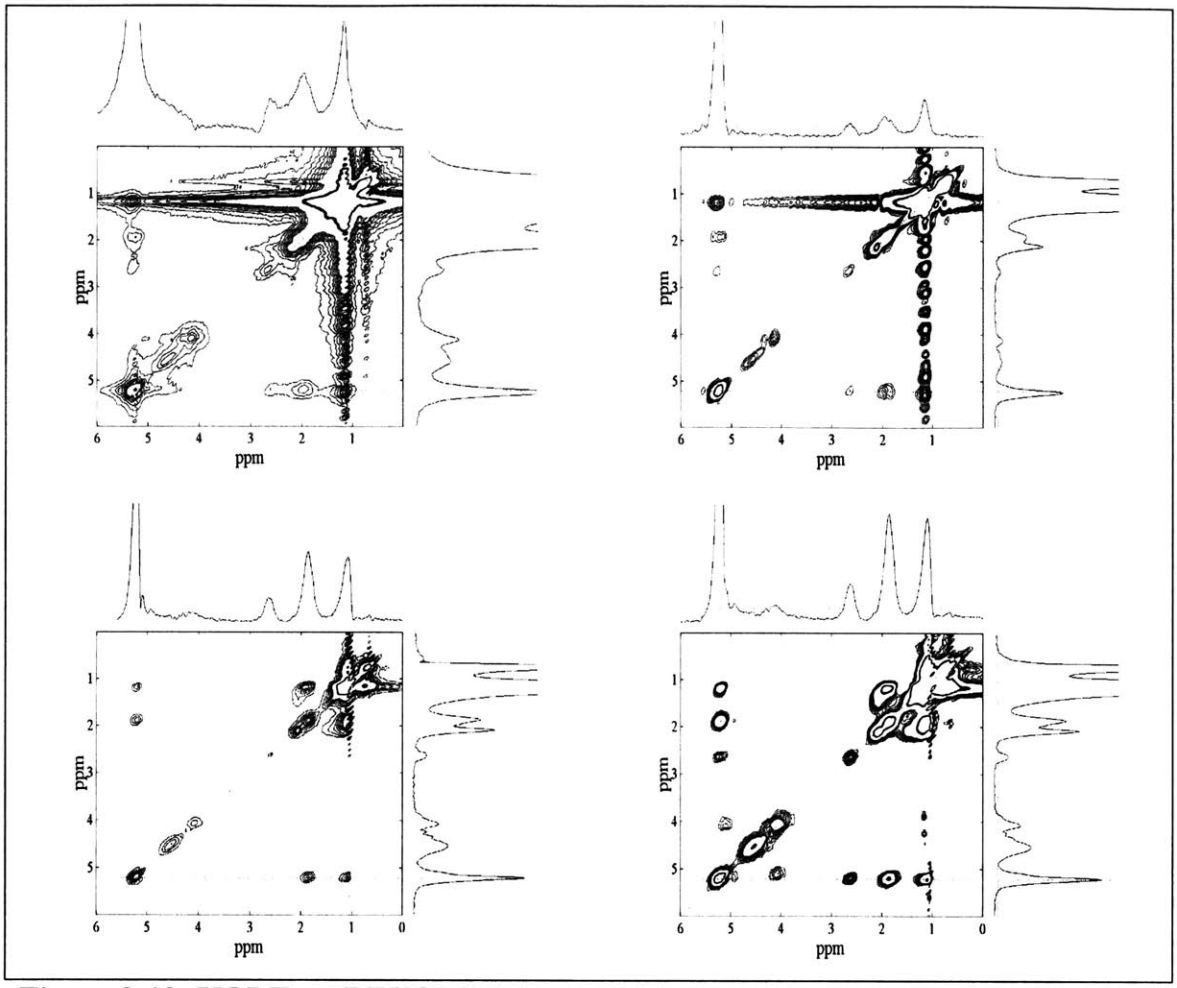

Figure 3-12: VOLT vs. REVOLT Bone Marrow spectra. (24 minutes; 3.1 ml.)
Bone marrow spectra obtained with VOLT (top row) and REVOLT (bottom row). The unweighted data is in the left column and the apodized data is in the right column. To remove the large dispersive component completely from the unweighted VOLT spectra, a $\pi/8$ degree shifted sine squared bell (t_1:$\pi/8$; t_2:$\pi/8$) was applied in both dimensions. A Lorentz to Gauss weighting function (t_1:1,9; t_2:1,6) was applied to the REVOLT data.

3.5.2 Human Bone Marrow Experiments

To compare the sensitivity and resolution of VOLT to REVOLT, human bone marrow spectra were acquired from a 3.1-mL voxel in 24 minutes (Figure 3-12). The number of averages per t_1 increment was the same for both experiments. The VOLT and REVOLT spectra are displayed in magnitude and absorptive mode respectively. Note the superior line shape and flatter baseline of the REVOLT spectrum. The dispersive wings contained in the VOLT spectra obscure the cross peaks at this contour level. The

dispersive line shape was partially removed at the expense of sensitivity by applying a $\pi/8$ shifted sine squared bell in both dimensions. Even after applying such a severe apodization function, the t_1 noise from the large methyl peak is still present and obscures one of the cross peaks into the vinyl protons. The REVOLT spectrum is superior to VOLT with respect to both resolution and sensitivity.

As an illustration of REVOLT's superior sensitivity, bone marrow spectra were acquired from a 1.4 mL voxel in 12 minutes (Figure 3-13). Only a two step phase cycle was used when acquiring these bone marrow spectra. The dispersive line shape in the unweighted spectrum obscures the cross peaks in VOLT. When the dispersive line shape is removed with the application of a shifted sine squared bell in both dimensions the cross peak intensities become almost imperceptible. The cross peaks in REVOLT are easily seen.

Truncating the current REVOLT data to only 48 t_1 increments simulated a REVOLT experiment acquired in 5 minutes 21 seconds. This truncated data set has been reconstructed in an identical fashion to the 96 t_1 increment REVOLT data. The resolution and intensities of the cross peaks show very little distortion. The truncation of the data set results in a truncation artifact off the methyl peak, which obscures a single cross peak. This simulated short acquisition time experiment reveals that truncation artifacts caused by insufficient sampling in the indirect dimension is currently a major limitation of REVOLT.

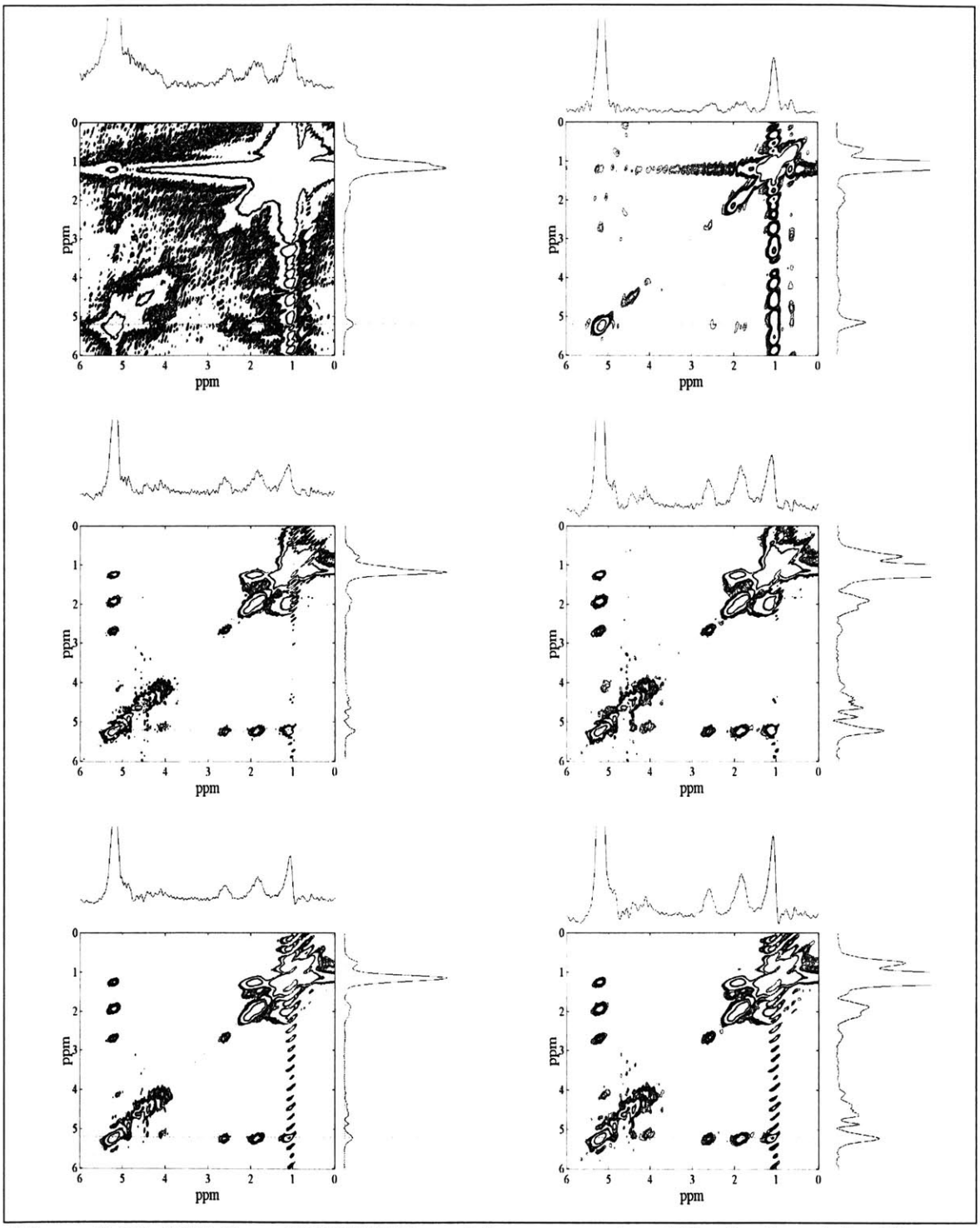

Figure 3-13: VOLT vs. REVOLT Bone Marrow spectra. (12 minutes; 1.4 ml.)
Bone marrow spectra acquired with 96 t_1 increments from a 1.4 mL voxel in 11 minutes 42 seconds. VOLT spectra are in the top row, REVOLT spectra are in the middle row, and a truncated REVOLT spectra are in the bottom row. The truncated REVOLT spectra has an equivalent acquisition time of 5 minutes, 21 seconds. A $\pi/8$ shifted sine squared bell (t1:$\pi/8$,t2:$\pi/8$) was applied to the VOLT data in both dimensions. A Lorentz to Gauss weighting function (t1:1,3;t2:1,2) was applied to the REVOLT data.

3.5.3 NAA Experiments

Phase cycling is necessary to maximize the degree of water suppression. To determine the optimum phase cycle needed to accompany water suppression for VOLT, REVOLT, and Q-REVOLT, a series of 2D experiments with different phase cycles was acquired. For each pulse sequence, four different phase cycles were tested. Phase cycling consisted of alternating the phase of the first and/or the third $\pi/2$ pulse by 180 degrees. A total of 4 acquisitions were averaged per t_1 increment regardless of the choice of phase cycle. Each 2D experiment was acquired with 16 t_1 increments and a spectral width of 125 Hz. This resulted in aliasing in the indirect dimension. This aliasing was effectively removed by taking a maximum intensity projection along the indirect dimension. Each 1D spectrum shown in Figure 3-14 through Figure 3-16 is a maximum intensity projection (MIP) of the limited spectral width experiments. These 1D spectra are plotted in a stacked plot format.

The 1D MIP spectra obtained with VOLT are plotted in Figure 3-14. Spurious water peaks at 5.5 ppm can be seen in the 1D MIP spectrum obtained without phase cycling. . These spurious peaks are effectively removed by all three methods of phase cycling. The degree of water suppression may be judged by comparing the remaining water signal to the NAA methyl peak.

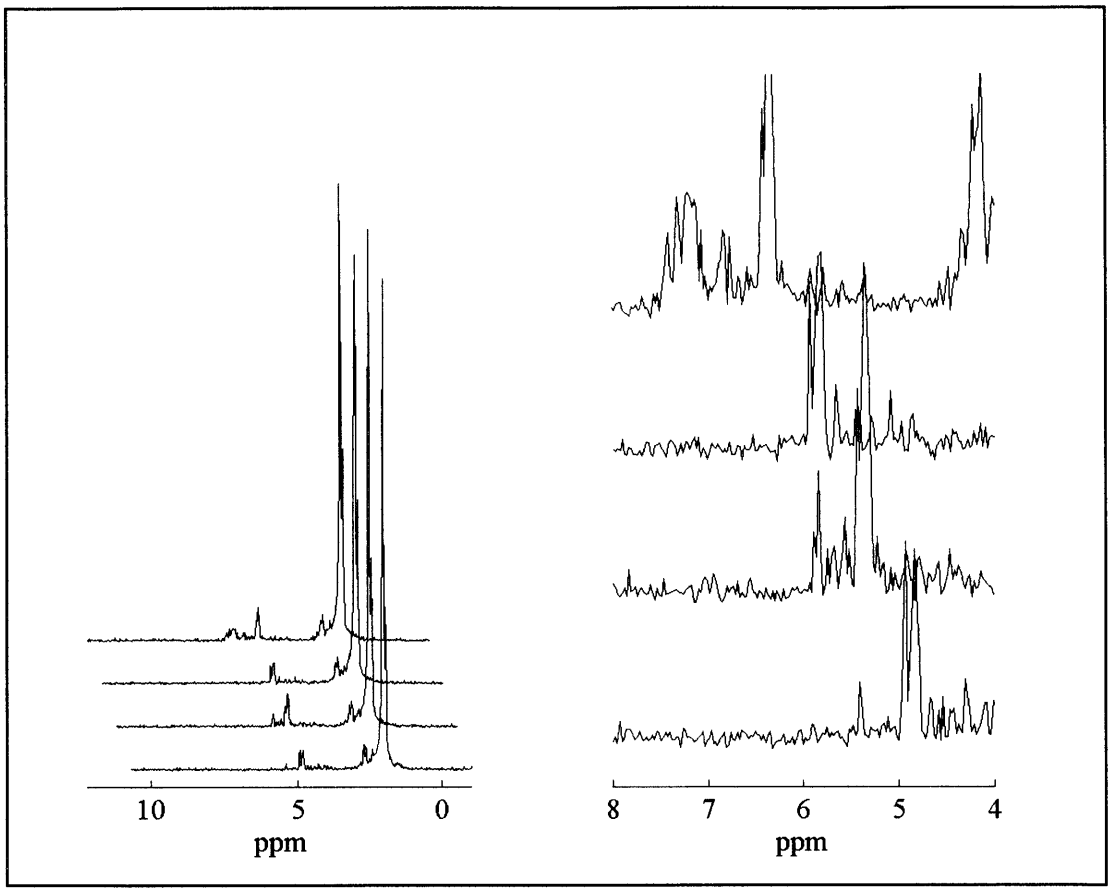

Figure 3-14: Phase cycling experiments with VOLT.
Maximum intensity projections of short 2D data sets are plotted as stacked plots. The spectra displayed were acquired with different phase cycling combinations, from front to back: phase cycling of the first and third $\pi/2$ pulse, phase cycling of the third $\pi/2$ pulse, phase cycling of the first $\pi/2$ pulse, and no phase cycling at all. Spectra on the left show the degree of water suppression obtained with respect to the NAA methyl peak. Spectra on the right are close up of spectra on the left to clearly illustrate the effects of phase cycling.

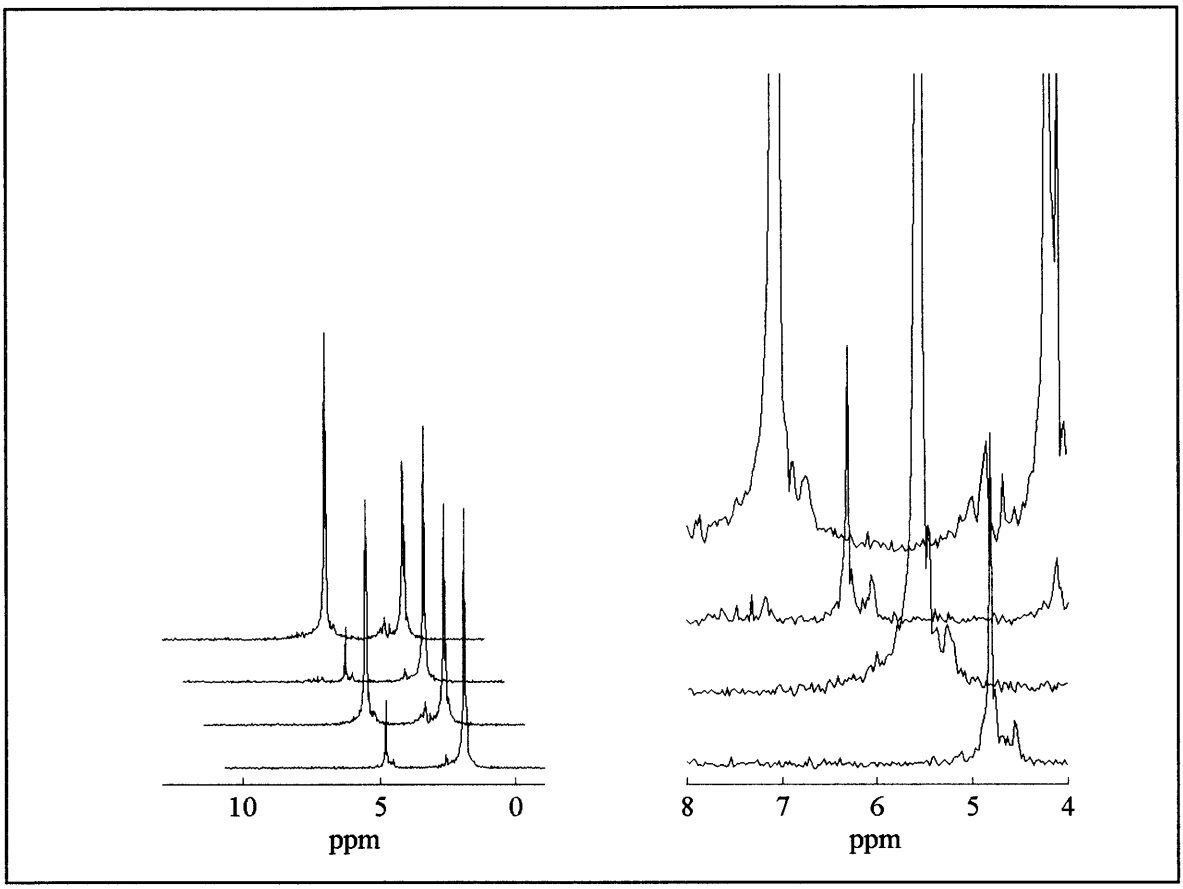

Figure 3-15: Phase cycling experiments with REVOLT.
Maximum intensity projections of short 2D data sets are plotted as stacked plots. The spectra displayed were acquired with different phase cycling combinations, from front to back: phase cycling of the first and third $\pi/2$ pulse, phase cycling of the third $\pi/2$ pulse, phase cycling of the first $\pi/2$ pulse, and no phase cycling at all. Spectra on the left show the degree of water suppression obtained with respect to the NAA methyl peak. Spectra on the right are close up of spectra on the left to clearly illustrate the effects of phase cycling.he phase cycling of the first $\pi/2$ pulse clearly removes the axial water peak from the spectrum. Small spurious water peaks are removed by phase cycling the third p/2 pulse by 180 degrees. These experiments show that a four step phase cycle is necessary to minimize artifacts in the spectrum when water suppression is required.

Figure 3-15 shows the identical experiment just described acquired with REVOLT instead of VOLT. The degree of water suppression obtained with REVOLT is less than that of VOLT. The residual water contained in the 1D MIP spectrum without phase cycling is equal to the NAA methyl peak. A substantial portion of this residual water signal is from axial peaks contained in the volume of interest. These axial peaks are removed by phase cycling the first $\pi/2$ pulse. This results in a decrease in the residual

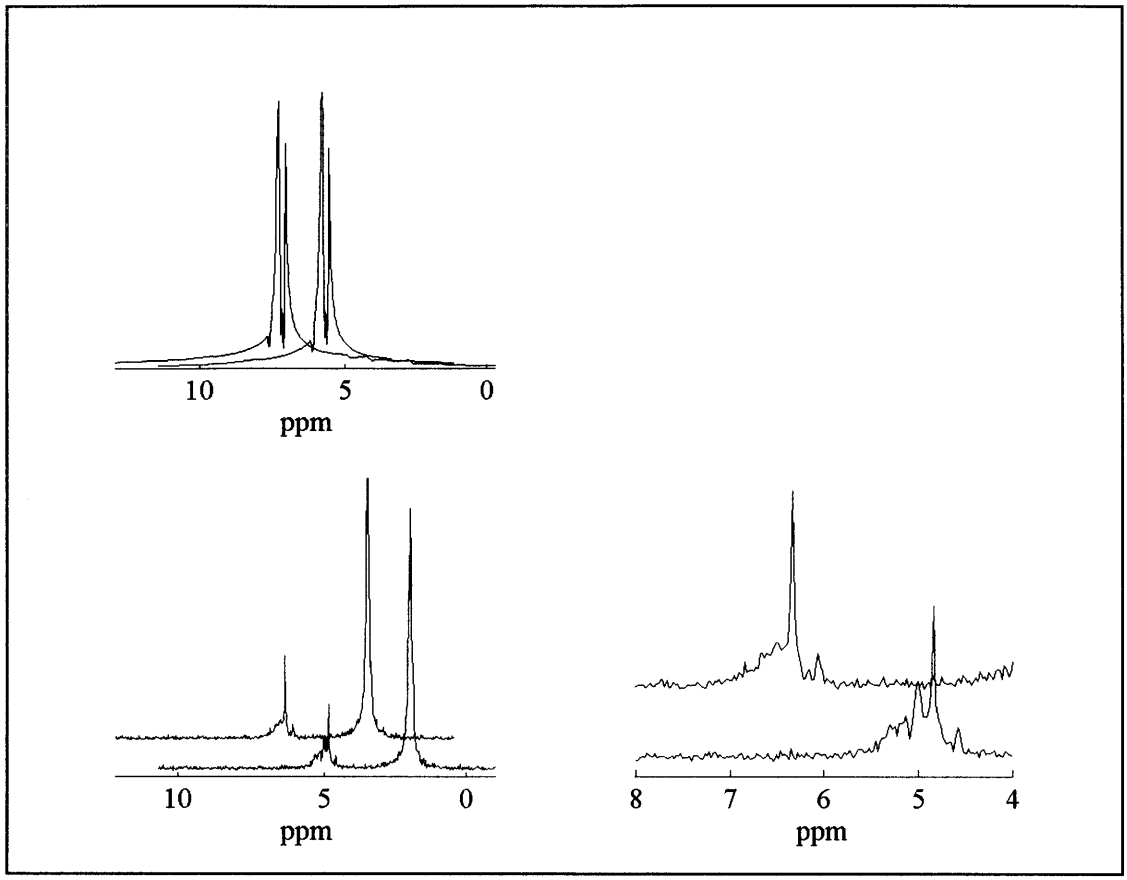

Figure 3-16: Phase cycling experiments with Q-REVOLT.
Maximum intensity projections of short 2D data sets are plotted as stacked plots. The spectra displayed were acquired with different phase cycling combinations. Spectra on the left show the degree of water suppression obtained with respect to the NAA methyl peak. Spectra on the right are close up of spectra on the left to clearly illustrate the effects of phase cycling.he upper left figure shows the spectrum acquired without phase cycling the first $\pi/2$ pulse. The front spectrum is a two step phase cycle with the third $\pi/2$ pulse and the back spectrum is acquired with no phase cycling. The residual water signal is so large that the NAA is not visible in either spectrum. The lower left from front to back shows the spectra obtained with the complete four step phase cycle and a two step phase cycle alternating the first $\pi/2$ pulse. The spectra on the right is a blow up of the spectra on the left around the water resonance at 4.75 ppm.

water signal by a factor of five. Small spurious water peaks downfield from the water resonances are removed by phase cycling the third $\pi/2$ pulse.

Figure 3-16 shows the 1D MIP spectra acquired with Q-REVOLT. A large water signal is present in the 1D MIP spectra when the first $\pi/2$ pulse is not phase cycled. The residual water signal is so large that the NAA resonances are imperceptible. This residual water signal is from the outer volume excited by the final spin echo combination. The stability of the Q-REVOLT experiment allows the residual water signal to be removed by

phase cycling the first $\pi/2$ pulse. Once the outer volume signal, in addition to the water axial peaks, is removed by phase cycling, the NAA resonances are visible.

Full 2D spectra were acquired from the NAA phantom using VOLT, REVOLT, and Q-REVOLT. The data are presented in Figure 3-17. The voxel size was measured from the voxel projections to be 59 mL. The spectral width in both dimensions was 750 Hz. The acquisition time in the indirect dimensions was 128 ms resulting in a total of 96 t_1 increments. Eight averages were acquired for each t_1 increment. All three pulse sequences used FLOPSY-8 for isotropic mixing. The VOLT spectrum has the greatest degree of water suppression. In addition, the lack of t_1 noise at the water resonance implies that water suppression is stable throughout the entire indirect acquisition time. Comparing the residual water peak in REVOLT to the NAA methyl peak shows that REVOLT is capable of suppressing the water by a factor of 6000. The degree of water suppression varies slightly for each t_1 increment resulting in t_1 noise along the indirect dimension. This t_1 noise is contained to the line width of the residual water signal. Removing a large water signal with phase cycling in Q-REVOLT results in a significant increase in the t_1 noise. The line width of the residual water signal in Q-REVOLT is an order of magnitude larger than either the residual water signal in VOLT or REVOLT because of incomplete removal of the outer volume water signal with phase cycling. This broad residual water signal and t_1 noise begins to obscure the cross peak resonances of NAA. The instabilities, which resulted in the t_1 noise, only become worse *in vivo*. For this reason Q-REVOLT was not used to acquire *in vivo* spectra.

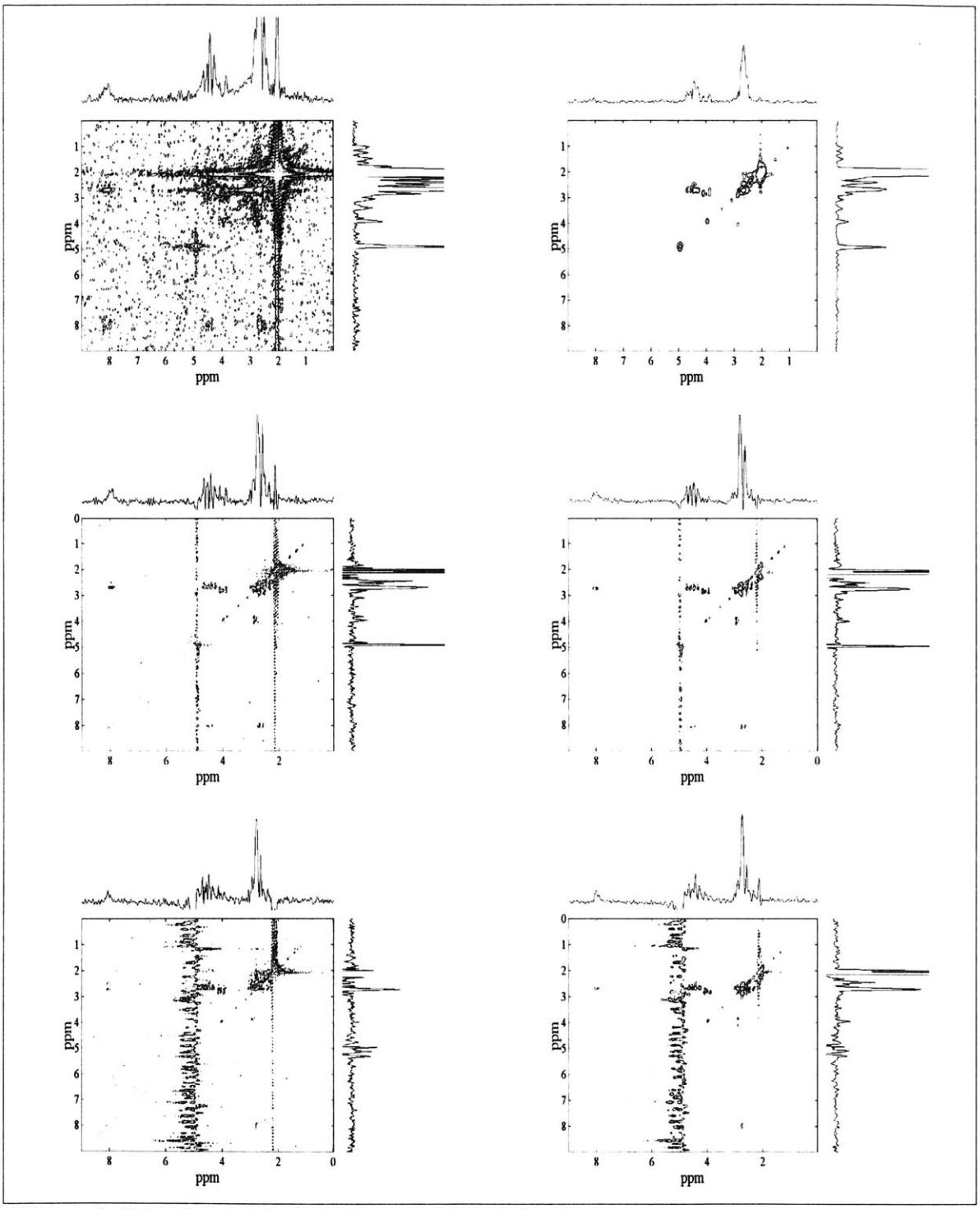

Figure 3-17: VOLT, REVOLT, & Q-REVOLT NAA spectra.

VOLT (first row), REVOLT (second row), and Q-REVOLT (third row) corn oil spectra were obtained from a 59 mL voxel with phase cycling. The left column contains the unweighted spectra and the right column contains the apodized data. The VOLT spectrum was weighted with a $\pi/8$ degree shifted sine squared bell to remove the dispersive component. A Lorentz to Gauss apodization function (t_1:1,9; t_2:1,6) was applied to the REVOLT and Q-REVOLT spectra. The horizontal trace reveals the intensity of the vinyl cross peaks. The vertical trace shows the diagonal of each spectrum.

The dispersive line shape of the VOLT spectra obscures the cross peaks at 4.5 ppm. The dispersive line shape was removed by a $\pi/8$ shifted sine squared bell apodization function. This severe apodization function obliterates the amino cross peak resonance, as well as attenuating the 4.5 ppm cross peaks. The REVOLT spectrum not only improves the resolution but also the sensitivity post-apodization. An additional cross peak is observed at 8 ppm in the indirect dimension and 4.5 ppm in the direct dimension. This low intensity cross peak is unable to survive the apodization function necessary to remove the dispersive line shape of VOLT.

This cross peak is not present in the Q-REVOLT experiment. The broad line shape of the amino cross peak at 4.2ppm in the indirect dimension (F1) and 8ppm in the direct dimension (F2) is an indication that it has a short transverse relaxation time. Q-REVOLT, as has already been discussed, has a longer transverse time between first excitation pulse and acquisition, which also leads to an increase in the amount of chemical exchange between the amino protons and the saturated water protons.

As in corn oil, FLOPSY-4, FLOPSY-8 and WALTZ-4 were compared with respect to the coherence transfer efficiency of the mixing scheme. Figure 3-18 shows the data from a series of 2D experiments in which the βCH_2–αCH and αCH-NH_2 cross peaks in the VOLT spectra were monitored with traces parallel to F_2. It is apparent that both of the FLOPSY schemes achieve more efficient coherence transfer into the αCH-NH_2 correlation, with essentially identical efficiency in the βCH_2–αCH cross peak. FLOPSY was used for the remaining studies due to its slight coherence transfer efficiency advantage.

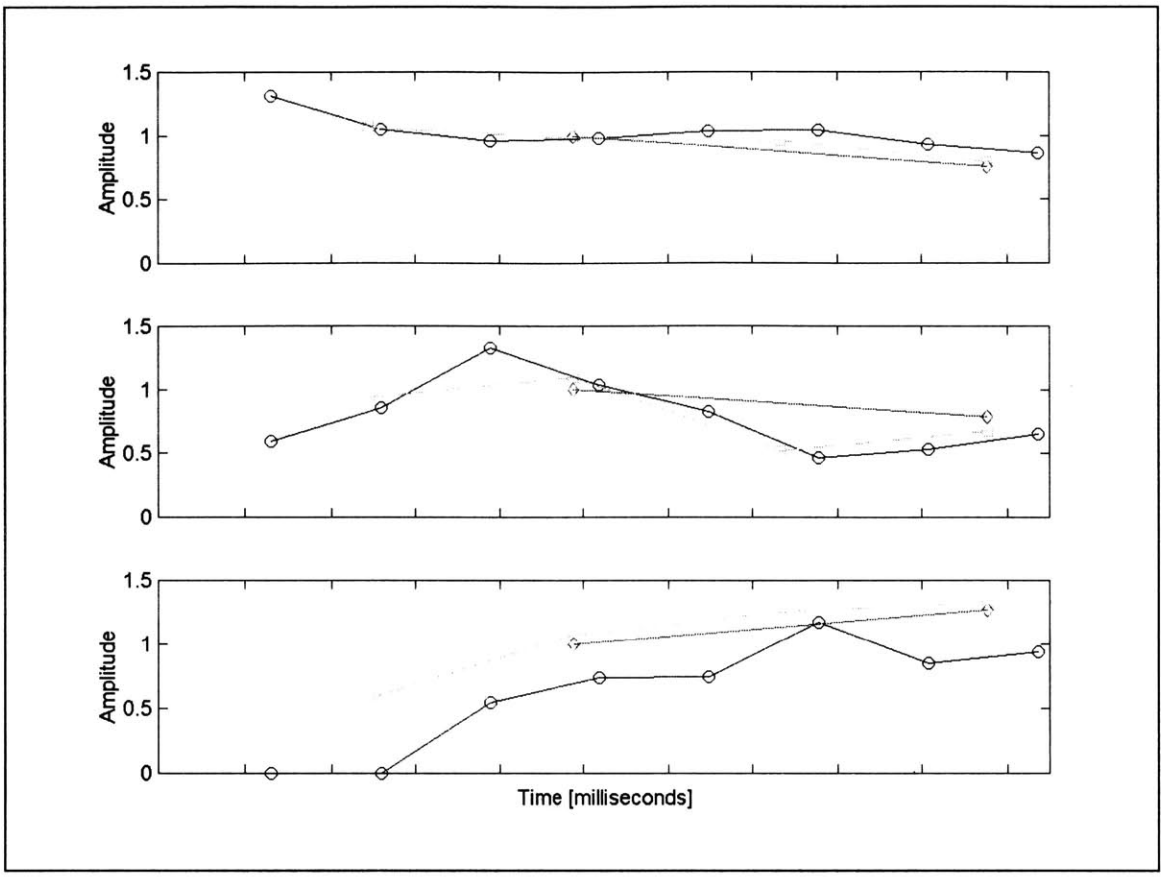

Figure 3-18: Coherence transfer efficiency of WALTZ-4, FLOPSY-4, FLOPSY-8.
Peak amplitudes of the NAA phantom were plotted as a function of isotropic mixing time for WALTZ-4 (circles), FLOPSY-4 (squares), and FLOPSY-8 (diamonds) . The diagonal peak is plotted in the top row, the βCH_2–αCH cross peak is plotted in the middle, and the αCH-NH_2 cross peak is plotted on the bottom.

3.5.4 Human Brain Experiments

Figure 3-19 compares spectra obtained in human brain using VOLT and REVOLT with identical volume sizes and the same total acquisition times. The volume size was 59 mL. FLOPSY-8 was used for isotropic mixing with an isotropic mixing time of 50.88 milliseconds. The optimum four step phase cycle was used to acquire each t_1 increment. Each phase cycle was averaged twice for a total of 8 averages per t_1 increment. 96 t_1 increments were acquired with a TR of 1.8 s resulting in a 23 minute acquisition time. The data was truncated to 192 data points in the direct dimension.

The F_2 trace is taken at the location of the NAA βCH_2 (Figure 3-20). Clearly, the REVOLT spectrum exhibits an increased sensitivity and resolution post-apodization.

The number of correlation peaks are also significantly increased. As expected, the stability of water suppression is superior in VOLT.

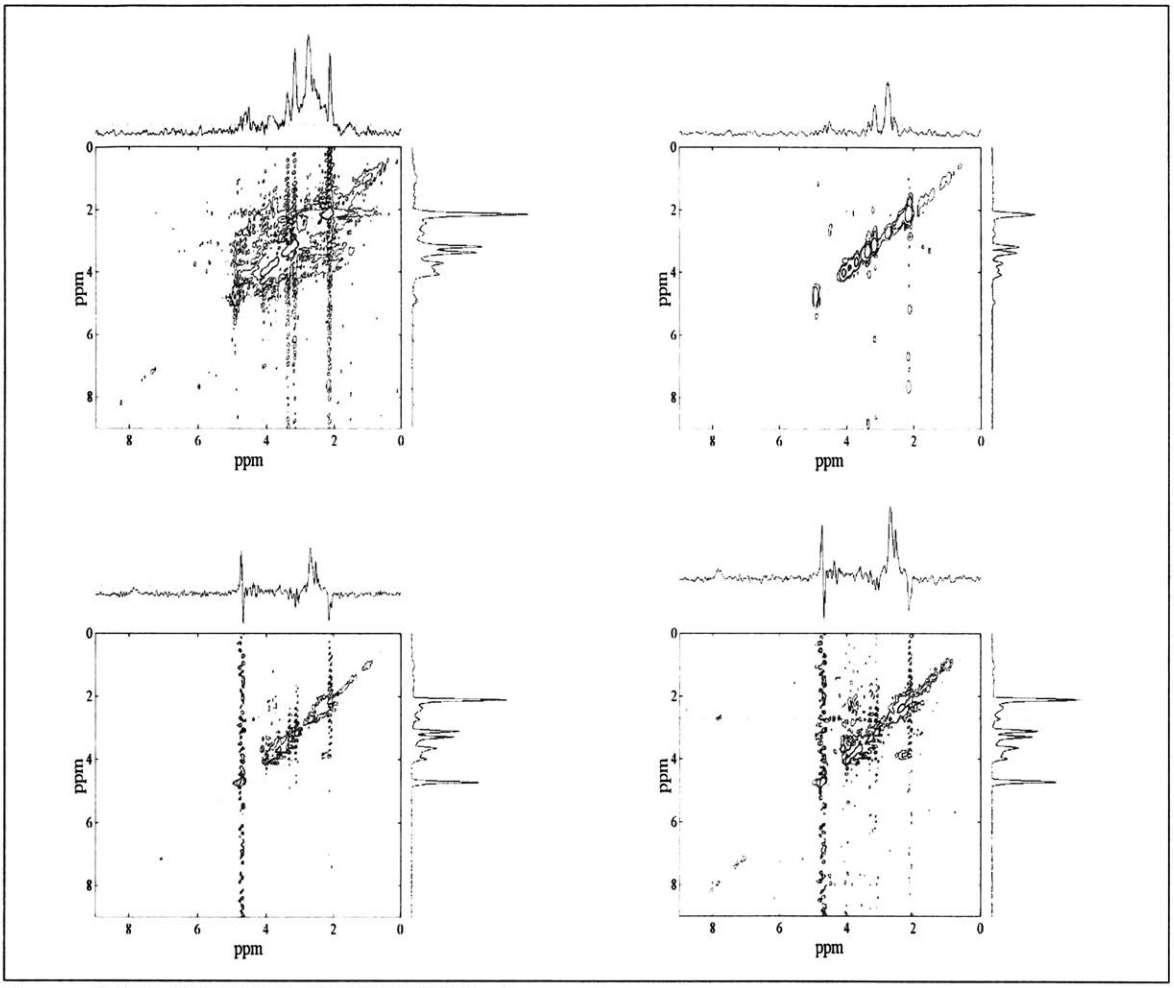

Figure 3-19: VOLT & REVOLT Brain spectra.

Human brain spectra obtained with VOLT (top row) and REVOLT (bottom row). The unweighted data is shown in the left column and the apodized data in the right column. To remove the large dispersive component from the unweighted VOLT spectra, a $\pi/8$ degree shifted sine squared bell (t_1:$\pi/8$; t_2:$\pi/8$) was applied in both dimensions. A Lorentz to Gauss weighting function (t_1:0.1,9; t_2:0.2,6) was applied to the REVOLT data.

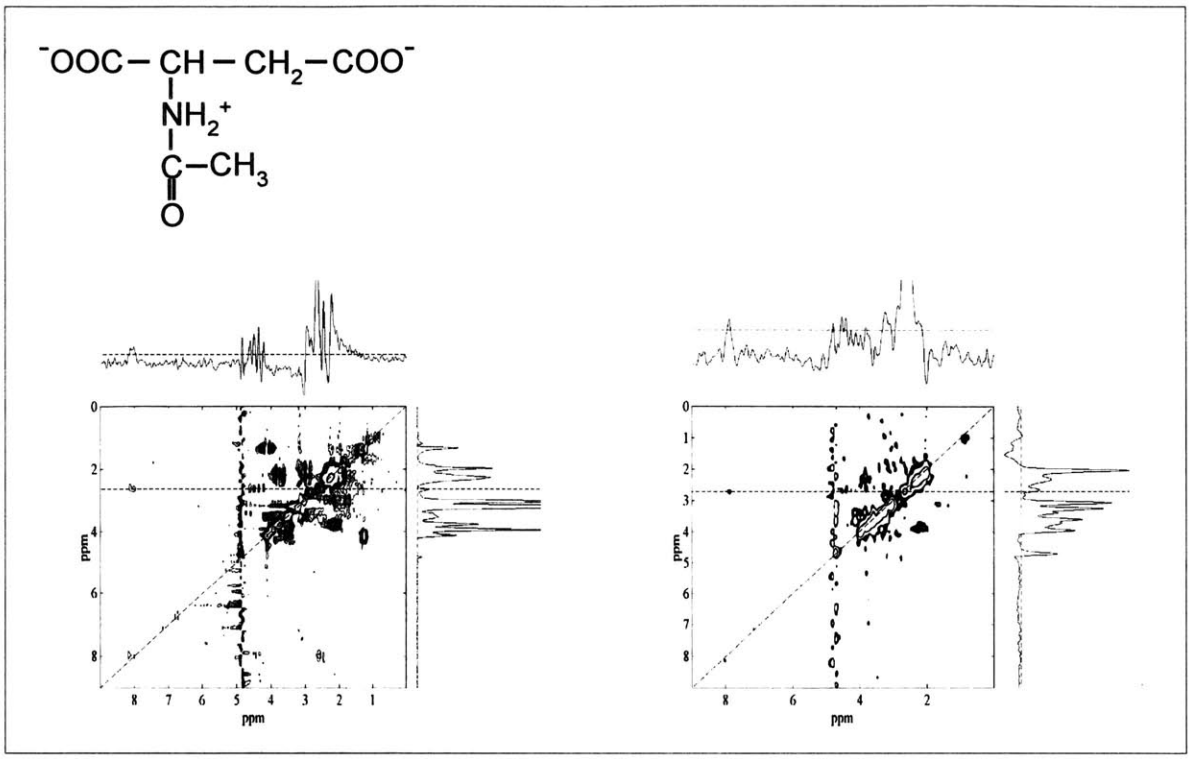

Figure 3-20: REVOLT NAA trace.

A schematic diagram of the NAA molecule is shown in the upper left. The spectrum on the left is a weighted spectrum of a brain phantom. The spectrum on the right is the REVOLT spectrum of human brain. A 1D horizontal trace through the NAA cross peaks at 2.6 ppm is plotted above each 2D spectrum. A Lorentz to Gauss apodization function (t_1:0.1,13; t_2:0.2,5) was applied to both spectra. The contour levels of each spectrum were drawn independent of each other to best illustrate the cross peaks of interest.

Figure 3-21 and Figure 3-22 show F_2 traces at the location of the glutamine/glutamate αCH proton, and the GABA γ–β cross peaks, respectively. Data are shown for both the *in vivo* brain spectrum and a REVOLT spectrum of a phantom containing the major brain metabolites at 17 mM concentration. Included in the phantom are NAA, glutamate, glutamine, choline, creatine, lactate, glucose and γ-aminobutyric acid (GABA).

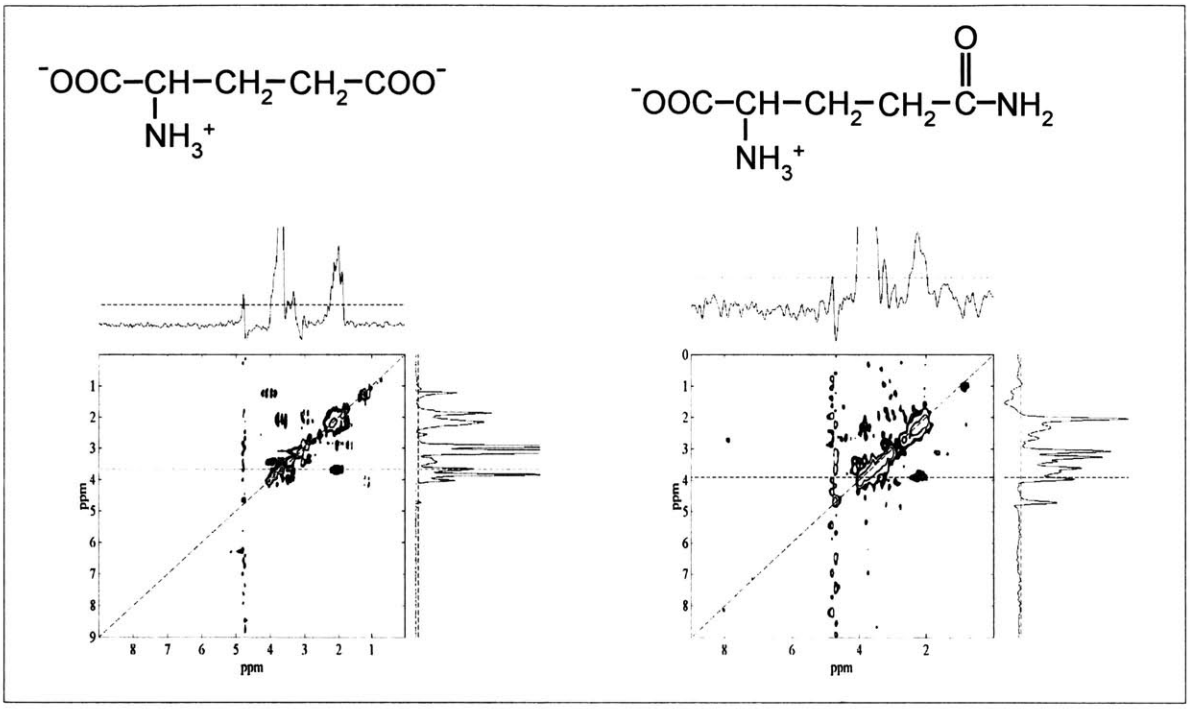

Figure 3-21: REVOLT Glu/Gln trace.

A schematic diagram of a Glutamate molecule (upper left) and a Glutamine molecule (upper right). The spectrum on the left is a weighted spectrum of a brain phantom. The spectrum on the right is the REVOLT spectrum of human brain. 1D F_2 horizontal traces through the Glu/Gln cross peaks at 3.7 ppm is plotted above each 2D spectrum. A Lorentz to Gauss apodization function (t_1:0.1,13; t_2:0.2,5) was applied to both spectra. The contour levels of each spectrum were drawn independent of each other to best illustrate the cross peaks of interest.

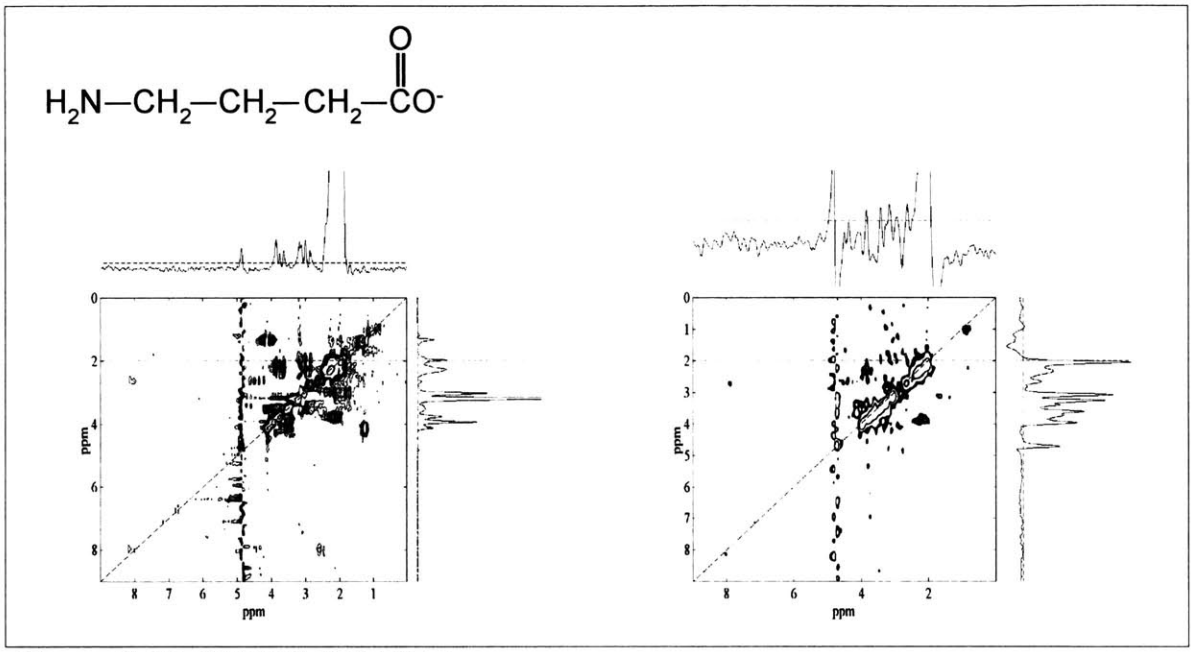

Figure 3-22: REVOLT GABA trace.

A schematic diagram of the GABA molecule is shown in the upper left. The spectrum on the left is a weighted spectrum of a brain phantom. The spectrum on the right is the REVOLT spectrum of human brain. A 1D horizontal traces through the GABA cross peaks at 3.0 ppm is plotted above each 2D spectrum. A Lorentz to Gauss apodization function (t_1:0.1,13; t_2:0.2,5) was applied to both spectra. The contour levels of each spectrum were drawn independent of each other to best illustrate the cross peaks of interest.

3.6 Discussion

REVOLT is the best method for obtaining chemical shift correlation spectra *in vivo* on a clinical scanner at 1.5 Tesla. The data acquired with REVOLT demonstrates that not only can 2D NMR spectroscopy be performed *in vivo*, but that it can be done in a reasonable amount of time on clinically useful volume sizes. The ability to extract flat baseline subspectra of lactate, Glu/Gln, and NAA demonstrates the utility of the method. If done in combination with non-Fourier analysis of the subspectra, a fully automated, unambiguous measurement of the major brain metabolites may be possible.

Potential for clinically relavant analysis is tremendous. For example, the presence of lactate is directly related to the grade of primary CNS neoplasms (35). Overlapping lipid or macromolecular resonances often obscures this peak. The ability to measure the intensity of the αCH cross peak should allow for an unambiguous method for the quantitation of this molecule.

Glutamine and glutamate have great importance to cerebral amine metabolism. The importance of monitoring the relative amounts of these metabolites, as well as their combined total, has particular relevance to the study of hepatic encephalopathy (36).

GABA levels have only recently been measured with 1D editing techniques (37). This inhibitory neurotransmitter plays a role in disorders as widely divergent as seizures (38) and depression (39,40). Its measurement is becoming important not only to the study of these disorders but in the evaluation of their pharmacological manipulation.

Although the raw data of VOLT exhibits a slight correlation peak sensitivity advantage, the superior line shape of the REVOLT spectra allows for much more spectral information to be derived following apodization. Indeed, the REVOLT spectra in bone marrow and brain are clearly superior in quality to the VOLT data presented.

The gradients utilized for these studies were operating at 0.9 G/cm. For this reason, moving to a system with higher gradient strength would reduce losses due to phase evolution during the PRESS section of REVOLT by reducing the required gradient lengths.

Extension of the basic REVOLT or VOLT sequence to heteronuclear applications is also possible. The excellent water suppression may allow indirect detection experiments, such as Heteronuclear Multiple Quantum Coherence (HMQC) (41), to be performed *in vivo*.

Finally, REVOLT functions well as a stable 1D single voxel experiment with recovery of the saturated resonances. The use of REVOLT in combination with spectral editing pulses might allow for clean editing of 1D spectra for detection of brain metabolites.

Chapter 4 : RF Power Deposition

4.1 Introduction

As shown, chemical shift correlation experiments that rely on in-phase coherence transfer are superior to those that rely on anti-phase coherence transfer. However, improvement in sensitivity with in-phase coherence transfer is accompanied by an increase in RF power deposition to the patient. While this increase is significant compared to other methods of *in vivo* spectroscopy, the amount of RF power deposited does not exceed the Food and Drug Administration (FDA) regulations.

These regulations are defined in terms of the Specific Absorption Rate (SAR), which is the amount of energy deposited into a kilogram of tissue per unit time. The FDA Center for Devices and Radiological Health (CDRH) has determined that if the SAR exceeds

4 Watts/kilogram averaged over the whole body for any period of 15 minutes; or

3 Watts/kilogram averaged over the head for any period of 10 minutes; or

8 Watts/kilogram in any gram of tissue in the head or torso, or 12 Watts/kilogram of tissue in the extremities, for any period of 5 minutes,

then that particular pulse sequence poses a significant risk with respect to RF power deposition (9). The safety of in-phase coherence transfer methods will be demonstrated theoretically and empirically according to the formalism of Bottomley et al.(42, 43). The SAR deposited by REVOLT will be derived for a sphere and a cylinder. A relationship relating the temperature increase to the SAR will also be derived. These theoretical calculations will be tested empirically by measuring the temperature increase in a spherical phantom. The amount of RF power deposited by REVOLT will be compared to a 2D Fast Spin Echo (FSE) sequence. This comparison will reveal that the SAR of REVOLT with 48 milliseconds of isotropic mixing is less than the SAR of FSE by 46 percent. This comparison is significant since FSE is routinely used for standard clinical imaging.

4.2 Theory

Theoretical estimates of the SAR for a homogenous sphere and cylinder of tissue were derived according to the formalism of Bottomley et al.(42,43) The sphere and cylinder are assumed to be oriented axially with a circularly polarized RF magnetic field. The RF power deposited in the tissue is assumed to arise solely from joule heating generated by the electric fields induced by an oscillating magnetic field. The peak specific absorption rate, SAR_{peak}, occurs at the surface of a sphere or a cylinder, with radius R, and is defined as

$$SAR_{peak} = \left|E_{rms}\right|^2 \Big/ (\rho \Omega s) \left[\frac{\text{Watts}}{\text{kilogram}}\right], \tag{4.1}$$

where E_{rms} is the amplitude of the electric field, ρ is the tissue density, Ω is the tissue resistivity, and s is the specific gravity of tissue. The electric field associated with an oscillating magnetic field may be calculated from Faraday's Law,

$$\oint \vec{E} \cdot d\vec{s} = -\frac{d\Phi_{B_{rf}}}{dt}, \tag{4.2}$$

where ds is the differential element of the contour to be integrated over, and Φ_B is the magnetic field flux. The magnetic field flux is defined in terms of the magnetic field,

$$\Phi_{B_{rf}}(t) = \oint \vec{B}_{rf}(t) \cdot d\vec{A}. \tag{4.3}$$

Here, B_{rf} is the oscillating magnetic field strength, and dA is a differential element of the surface area. Solving Equations 4.2 and 4.3 for the amplitude of the electric field given a current loop with radius, R, reveals that

$$E = -\frac{1}{2}\frac{dB_{rf}(t)}{dt} R. \tag{4.4}$$

The oscillating magnetic field strength may be rewritten in terms of an amplitude, B_{rf}, an amplitude modulation function, f(t), and a time dependent oscillating component.

The frequency selective pulses used in MRS require that an amplitude modulation function be included in SAR calculations. For a hard pulse, f(t) is unity for the duration

of the pulse. The oscillating magnetic field for a quadrature coil is a circularly polarized magnetic field. The time dependent oscillating magnetic field is

$$B_{rf}(t) = B_{rf}\, f(t) e^{(i\,2\pi\upsilon t)}. \tag{4.5}$$

The electric field induced by an oscillating magnetic field may be rewritten as,

$$\mathrm{E} = -\frac{1}{2} B_{rf} \left\{ i2\pi\upsilon f(t) e^{(i2\pi\upsilon t)} + f'(t) e^{(i2\pi\upsilon t)} \right\} R. \tag{4.6}$$

The root mean square (RMS) of the electric field for a single cycle is

$$E_{rms} = \left(\frac{1}{\upsilon} \int_0^{\frac{1}{\upsilon}} |E|^2 \, dt \right)^{\frac{1}{2}}. \tag{4.7}$$

The amplitude modulation function, f(t), complicates this calculation. To proceed with the calculation of E_{rms}, the amplitude modulation function, f(t), is assumed to be slow compared to the oscillating component, which is always true in NMR. With this assumption, the derivative of the amplitude modulation may be set to zero and f(t) may be extracted from the integrand when calculating the root mean square of the electric field over a single oscillation,

$$E_{rms} = \pi\upsilon B_{rf} R f(t). \tag{4.8}$$

Integrating Equation 4.12 with respect to time over the entire pulse width removes the time dependence of the envelope function, f(t). The time independent E_{rms} is

$$E_{rms} = \pi\upsilon B_{rf} R \left(\frac{1}{\tau} \int_0^{\frac{1}{\tau}} |f(t)|^2 \, dt \right)^{\frac{1}{2}}. \tag{4.9}$$

Substituting the amplitude of the electric field, E_{rms}, into the definition for SAR, results in

$$\mathrm{SAR}_{\mathrm{peak}} = \left(\frac{\pi^2}{\rho} \right) \left(\frac{\upsilon^2 B_{rf}^2 R^2}{\Omega s} \right) \left(\frac{\int_0^{\tau} f^2(t) dt}{\tau} \right). \tag{4.10}$$

For convenience, the B_1 field strength is better written in terms of the flip angle, θ, and pulse width, τ, of the RF pulse. For a quadrature coil, the B_1 field is equal to the B_{rf} field. The relationship between the flip angle, θ, and the B_1 field strength for an amplitude modulated RF pulse is

$$B_{rf} = B_1 = \frac{\theta}{2\pi\gamma \int_0^\tau f(t)\,dt}. \qquad \textbf{4.11}$$

Performing the appropriate substitutions and simplifying yields an expression for the peak SAR of an arbitrary amplitude modulated RF pulse,

$$\mathrm{SAR}_{\mathrm{peak}} = \left(\frac{1}{4\rho\gamma^2}\right)\left(\frac{\upsilon^2 R^2 \theta^2}{\Omega s \tau^2}\right)\left(\frac{\left(\frac{\int_0^\tau f^2(t)\,dt}{\tau}\right)}{\left(\frac{\int_0^\tau f(t)\,dt}{\tau}\right)^2}\right). \qquad \textbf{4.12}$$

The peak SAR in Equation 4.12 represents the RF power deposited by a single pulse. To determine the average SAR during a given T_R period, Equation 4.12 should be multiplied by the duty cycle, D,

$$\mathrm{SAR}_{\mathrm{peak}} = \left(\frac{1}{4\rho\gamma^2}\right)\left(\frac{\upsilon^2 R^2 \theta^2}{\Omega s \tau^2}\right)\left(\frac{\left(\frac{\int_0^\tau f^2(t)\,dt}{\tau}\right)}{\left(\frac{\int_0^\tau f(t)\,dt}{\tau}\right)^2}\right)\left(\frac{\tau}{T_R}\right) \qquad \textbf{4.13}$$

$$= \left(\frac{1}{4\rho\gamma^2}\right)\left(\frac{\upsilon^2 R^2 \theta^2}{\Omega s \tau}\right)\left(\frac{W_{\mathrm{eff}}}{A_{\mathrm{eff}}^2}\right) D$$

The integration over f(t) has been represented by W_{eff}, for the effective width, and A_{eff} for the effective area. Since Equation 4.13 is dependent upon the radius, repetition time, and tissue characteristics, comparing the RF power deposited by different pulse sequences can be cumbersome. Eliminating the dependence on external conditions would provide a convenient way to compare the RF power deposition among different pulse sequences.

A convenient method to calculate the SAR of a given pulse sequence is to convert all RF pulses to an equivalent number of standard pulses, N_{std}, where N_{std} is independent of external parameters. The total SAR can then be calculated from the SAR deposited by a standard pulse according to

$$SAR_{arb} = N_{std}\ SAR_{std}. \tag{4.14}$$

A standard pulse is defined as

$$N_{std} = \frac{SAR_{arb}}{SAR_{std}} = \frac{\left(\frac{1}{4\rho\gamma^2}\right)\left(\frac{\upsilon^2 R^2 \theta^2}{\Omega s \tau^2}\right)\left(\frac{W_{\text{eff}}}{A_{\text{eff}}^2}\right) D}{\left(\frac{1}{4\rho\gamma^2}\right)\left(\frac{\upsilon^2 R^2 \theta_{std}^2}{\Omega s \tau_{std}^2}\right)\left(\frac{W_{\text{eff,std}}}{A_{\text{eff,std}}^2}\right) D_{std}}$$

$$= \frac{\left(\frac{\theta^2}{\tau^2}\right)\left(\frac{W_{\text{eff}}}{A_{\text{eff}}^2}\right) D}{\left(\frac{\theta_{std}^2}{\tau_{std}^2}\right) D_{std}} \tag{4.15}$$

$$= \left(\frac{\tau_{std}}{\tau}\right)\left(\frac{\theta^2}{\theta_{std}^2}\right)\left(\frac{W_{\text{eff}}}{A_{\text{eff}}^2}\right) .$$

The total SAR deposited is equivalent to the SAR deposited by a standard hard pulse multiplied by the equivalent number of standard pulses in the sequence. A standard hard pulse is defined as a hard 1-millisecond π pulse. The amplitude modulation function, f(t), is unity for the duration of the standard pulse. The maximum SAR deposited by a standard hard pulse on a clinical 1.5 Tesla magnet (63.86 MHz) is

$$SAR_{peak,\ std} = \left(\frac{1}{4\rho\gamma^2}\right)\left(\frac{\upsilon^2\theta^2}{\Omega s\tau}\right)\left(\frac{R^2}{T_R}\right)$$

4.16

$$= 5.6\left(\frac{R^2}{T_R}\right) \quad .$$

The specific gravity and tissue resistivity was approximated as 1.0 and 1.0 Ohms per meter, respectively (42). Equation 4.16 is the peak SAR at radius R for a single standard pulse. The FDA guidelines are written in terms of an average SAR. To determine the average SAR deposited in a sphere or a cylinder, the peak SAR must be integrated over the respective volume. Both volumes are integrated in cylindrical coordinates. A cylindrical coordinate system was chosen because the B_1 field is constant for a given radius, R, and along a given length, z. Integrating Equation 4.16 over the volume of a sphere yields

$$SAR_{peak,\ sphere} = \frac{3}{4}\frac{1}{\pi R^3}\int_{-R}^{R}\int_{-\sqrt{R^2-z^2}}^{\sqrt{R^2-z^2}}\int_0^{2\pi} SAR_{peak}\, r\, d\phi\, d\theta\, dz$$

4.17

$$= \frac{2}{5}SAR_{peak} \quad ;$$

over the volume of a cylinder yields

$$SAR_{peak,\ cylinder} = \frac{1}{\pi R^2 L}\int_0^{L}\int_{-\sqrt{R^2-z^2}}^{\sqrt{R^2-z^2}}\int_0^{2\pi} SAR_{peak}\, r\, d\phi\, d\theta\, dz$$

4.18

$$= \frac{1}{2}SAR_{peak} \quad .$$

In order to empirically test the validity of Equations 4.16 through 4.18, an expression that relates temperature to SAR is needed. As RF power is deposited into a phantom, the phantom's temperature increases. The temperature of the phantom continues to increase until a steady state is achieved. A lumped system analysis approach was used to derive the relationship between temperature and the average SAR (44). A

lumped system analysis assumes that the temperature of the sphere is uniform. An energy balance equation may be written where the control volume is the surface of the phantom,

$$Q_{in} - Q_{out} = \rho c_p V \frac{dT(t)}{dt}, \tag{4.19}$$

where Q_{in} is the energy deposited into the phantom by RF, Q_{out} is the heat losses, ρ is the density of the fluid, c_p is the specific heat of the fluid, and V is the volume of the sphere. The phantom is assumed to lose all of its heat through convection to the surrounding air. Q_{out} may be expressed according to Newton's Law of Cooling as,

$$Q_{out} = Ah\left(T_o - T(t)\right), \tag{4.20}$$

where A is the surface area of the phantom, and h is the heat transfer coefficient. Solving the differential equation for temperature yields

$$T(t) = \frac{Q_{in}}{Ah}\left(1 - e^{-kt}\right) + T_o \tag{4.21}$$

where

$$k = \frac{Ah}{\rho c_p V} = \frac{3h}{\rho c_p R}.$$

At steady state the energy deposited into the phantom by RF and the heat lost through convection are equal to each other,

$$T(\infty) \equiv T_\infty = \frac{Q_{in}}{Ah}\left(1 - e^{-kt}\right) + T_o \tag{4.22}$$

therefore,

$$Q_{in} = Ah\left(T_\infty - T_o\right) \tag{4.23}$$

The average SAR_{avg} is equal to Q_{in} divided by the mass of the phantom,

$$SAR_{avg} = \frac{Q_{in}}{m} = \frac{Ah}{m}(T_{\infty} - T_o). \quad \textbf{4.24}$$

Equation 4.24 may be used to relate a change in the temperature of the phantom to the SAR if the heat transfer coefficient, h, is known.

4.3 Materials and Methods

To establish the safety of REVOLT, two experiments were conducted. The first experiment measured the RF power deposited by REVOLT and FSE, which allowed direct comparison of the two pulse sequences. Both pulse sequences were determined to be safe, since neither induced a significant temperature increase in a saline phantom. Because there was an insignificant temperature change in the first experiment, estimating the RF power deposited with Equation 4.24 is extremely inaccurate. Increasing the RF power deposited by REVOLT and repeating the experiment allowed for an accurate estimate of the RF power deposited.

A sphere with an outer diameter of 9 centimeters was used in all RF power deposition experiments. The sphere's wall thickness and thermal properties were ignored in all subsequent calculations. The sphere was filled with a 145 millimolar solution of NaCl. All temperature measurements were done with a single junction copper/constantan thermocouple and a battery powered thermocouple reader (Bailey Instruments, Clinton, NJ, model T-8). The phantom was placed inside a quadrature head coil. The position of the phantom with respect to the coil was not altered throughout the experiments. Temperature measurements were also made on a spherical control phantom filled with the same solution with a radius of 3.4 centimeters placed 0.45 meters from the front edge of the head coil. A smaller spherical phantom was used as the control because it was readily available. The position from the edge of the head coil was chosen such that the control would remain in the bore during the experiment but be far enough away from the coil to be unaffected by the RF pulses. The repetition time for all experiments was 1.8

seconds. The thermocouple was removed from the phantoms during irradiation to insure that the thermocouples would not interact with the RF, resulting in additional heating.

4.3.1 REVOLT and FSE Temperature Comparison

The phantom was placed in the bore of the magnet at the central imaging plane. The FSE sequence was calibrated with an automated prescan immediately after the phantom was placed inside the bore. This was done so that the RF power deposited during the calibration would not contribute to an increase in temperature. Temperature measurements were made on both phantoms every ten minutes by temporarily extracting the phantom from the bore. After the temperature measurements were made, the phantoms were returned to the bore. The phantoms remained in the bore for an hour before imaging began with FSE. FSE images of the phantom were acquired continuously for ten minutes. Temperature measurements were taken from the phantoms after the FSE sequence had completed. Immediately after the temperature was measured from both phantoms, they were returned to the bore and imaged again by the FSE. This process continued for a total of two hours.

After FSE temperature experiment was completed, the REVOLT sequence was calibrated. Temperature measurements were taken on the phantom every ten minutes for a total of thirty minutes with the B_1 field turned off. After the thirty minutes, spectra were acquired with REVOLT every 12 minutes from the saline phantom. Temperature measurements were obtained from both phantoms for a total of two hours in between REVOLT experiments.

4.3.2 RF Temperature measurements

Another experiment was conducted with REVOLT to corroborate Bottomley's theoretical derivation of the SAR for a sphere. Under the previous experimental conditions the average SAR predicted by Bottomley is 0.6 Watts per kilogram. Previous experiments have shown that the heat transfer coefficient in the bore is on the order of 5 Watts per C per meter squared. The predicted temperature increase is only 3.0 degrees C at steady state. Temperature fluctuations inside the bore of the magnet have been observed to vary between 2 to 3 degrees over several hours. To ensure that the

temperature increase in the phantom is due to RF power deposition and not fluctuations in the ambient bore temperature, the RF power deposited by the isotropic mixing scheme was increased 7.6 times. This was accomplished by increasing the B_1 field strength by a factor of two and increasing the length of the mixing scheme from 51 milliseconds for FLOPSY-8 to 97.2 milliseconds for WALTZ-4. Since each isotropic mixing scheme is a phase modulated hard pulse, the choice of isotropic mixing scheme is irrelevant with respect to RF power. Only the entire isotropic mixing scheme's pulse width and B_1 field strength contributes to the SAR. Doubling the isotropic mixing scheme's B_1 field strength and pulse width resulted in a REVOLT experiment with a SAR 6.5 times above normal. The expected temperature increase at a SAR of 3.4 Watts per kilogram is 19.5 degrees assuming the same heat transfer coefficient.

4.4 Results

4.4.1 Number of Standard Pulse Calculations

Table 4-1 calculates the number of standard pulses in REVOLT with a FLOPSY-8 isotropic mixing scheme. The CHESS pulses were assumed to be $\pi/2$ pulses for this calculation.

	N	A_{eff}	W_{eff}	θ [deg]	τ [ms]	Nstd	Total Nstd	%
CHESS Pulses	6	0.2398	0.20118	90	50.00	0.017	0.105	0.2%
Hard $\pi/2$ pulse	2	1	1	90	0.24	1.042	2.083	3.9%
Hard π pulse	1	1	1	180	0.48	2.083	2.083	3.9%
IsotropicMixing	1	1	1	8480	50.88	43.621	43.621	82.4%
Soft $\pi/2$ pulse	1	0.2398	0.1922	90	1.80	0.464	0.464	0.9%
Soft π pulse	2	0.1534	0.1411	180	2.60	2.306	4.612	8.7%
						Total =	52.97	100.0%

Table 4-1: Number of Standard Pulses in REVOLT.
The number of standard pulses contained in REVOLT with a 50.1 millisecond isotropic mixing scheme. The CHESS pulses were assumed to be $\pi/2$ even though the flip angle of the last CHESS pulse was adjusted to minimize the water signal. N is the number of occurrences of a particular pulse, Nstd is the number of standard pulses for a particular pulse, and Total Nstd is equal to N*Nstd. The remaining column headings match the definitions in the text.

The following calculations were based on T_R of 1.8 seconds and assumed that the average radius for a human head and torso is 0.092 meters and 0.17 meters respectively (42). Approximating the human head as a sphere, the $SAR_{peak,head}$ is 0.026 Watts per kilogram. Since REVOLT, with a single cycle of FLOPSY-8, has an equivalent of 52.97 standard pulses, the $SAR_{peak,head}$ is 1.4 Watts per kilogram and the $SAR_{avg,head}$ is 0.6 Watts per kilogram. A similar calculation for the human torso, approximating it as a cylinder, reveals that $SAR_{peak,\ torso}$ is 4.8 Watts per kilogram, and the $SAR_{avg,torso}$ is 1.9 Watts per kilogram.

Table 4-2 calculates the number of standard pulses for an FSE sequence with 32 echoes and 3 slices per T_R period.

	N	A_{eff}	W_{eff}	θ [deg]	τ [ms]	Nstd	Total Nstd	%
Soft $\pi/2$ pulse	3	0.251	0.201	90	3	0.266	0.799	1.0%
Soft π pulse	96	0.251	0.201	180	4	0.799	76.727	99.0%
						Total =	77.53	100.0%

Table 4-2: Number of Standard Pulses in 2D FSE.
The number of standard pulse is calculated for a 2D FSE sequence with 32 echoes and 3 slices per T_R period. N is the number of occurrences of a particular pulses, Nstd is the number of standard pulses for a particular pulse, and Total Nstd is equal to N*Nstd. The remaining column headings match the definitions in the text.

The total number of standard pulses for this FSE sequence is 77.5, which is equivalent to an average SAR of 0.77 Watts per kilogram. The standard REVOLT sequence, as calculated in the previous section, has 53.0 standard pulses. Thus, a typical FSE sequence deposits 46 percent more RF power into a patient than REVOLT. An experiment was conducted to confirm that both, FSE and REVOLT, with equivalent SARs, would increase the temperature of a spherical phantom by the same amount. The isotropic mixing scheme used in REVOLT was increased from 50.1 millisecond with FLOPSY-8 to 77.8 milliseconds with WALTZ-4. By increasing the isotropic mixing scheme, both REVOLT and FSE had a SAR of .77 Watts per kilogram.

4.4.2 REVOLT and FSE Temperature Comparison

Figure 4-1 plots the temperature versus time of both saline phantoms for FSE and REVOLT. The apparent temperature increase in both experiments is a result of a small increase in the bore temperature over four hours.

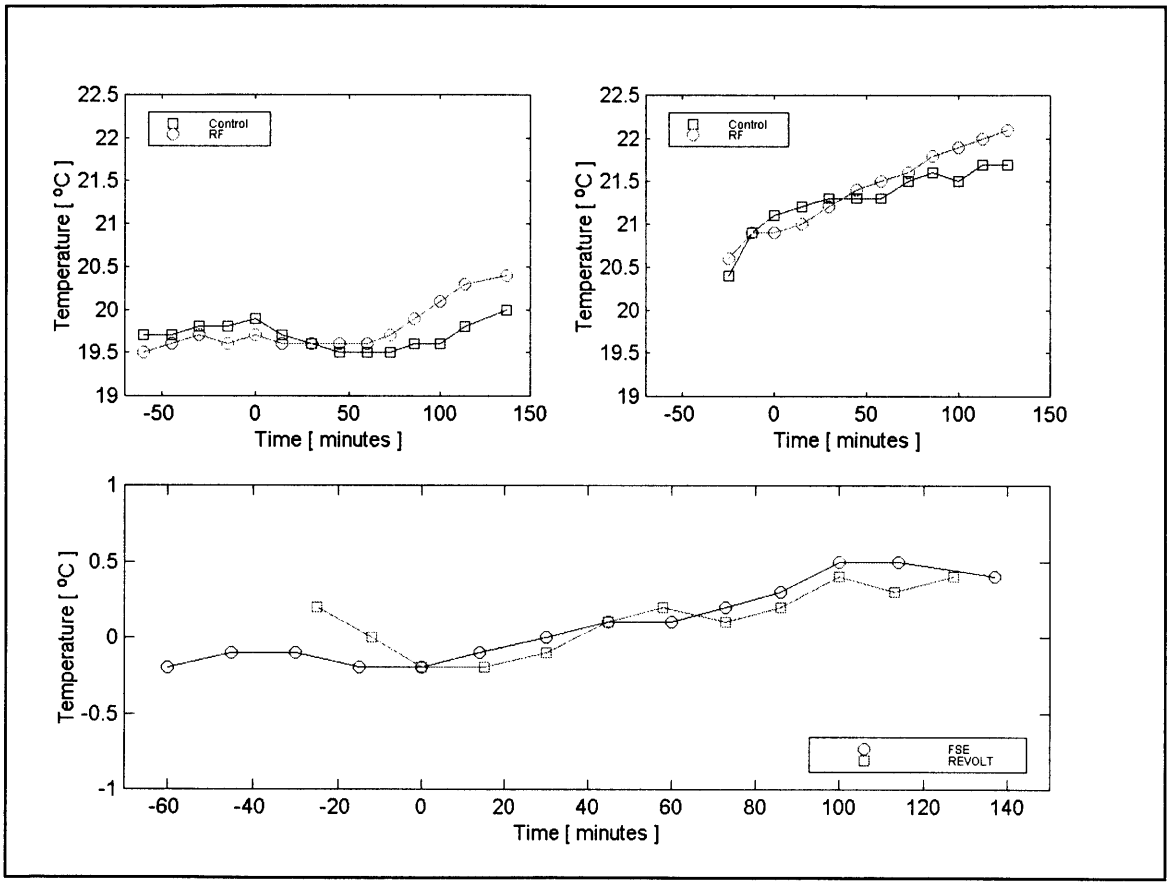

Figure 4-1: FSE vs. REVOLT Temperature Comparison.
Upper left, temperature vs. time plot of a spherical phantom exposed to RF generated by FSE (circles) and a control phantom (squares). Upper right, the corresponding plot for REVOLT. The temperature measurements made before and including 0 minutes was the time allowed for the phantoms to establish equilibrium. The plot in the bottom row is a time vs. temperature plot of FSE (circle) and REVOLT (square) with the corresponding control temperature subtracted from the temperature measurements. This plot reveals no significant increase in the temperatures of the phantom for either sequence.

4.4.3 RF Temperature measurements

The phantom was placed in the bore of the magnet and allowed to come to equilibrium for an hour and a half. Spectra were then collected from the phantom with REVOLT for 10 hours with temperature measurements taken from the phantom and the control every 15 minutes (Figure 4-2).

The temperature data for the phantom exposed to the RF was fitted to Equation 4.22 with a Levenberg-Marquardt algorithm (45) after the control temperature was subtracted. The ambient bore temperature, T_0, was 22 C, which was the the average bore

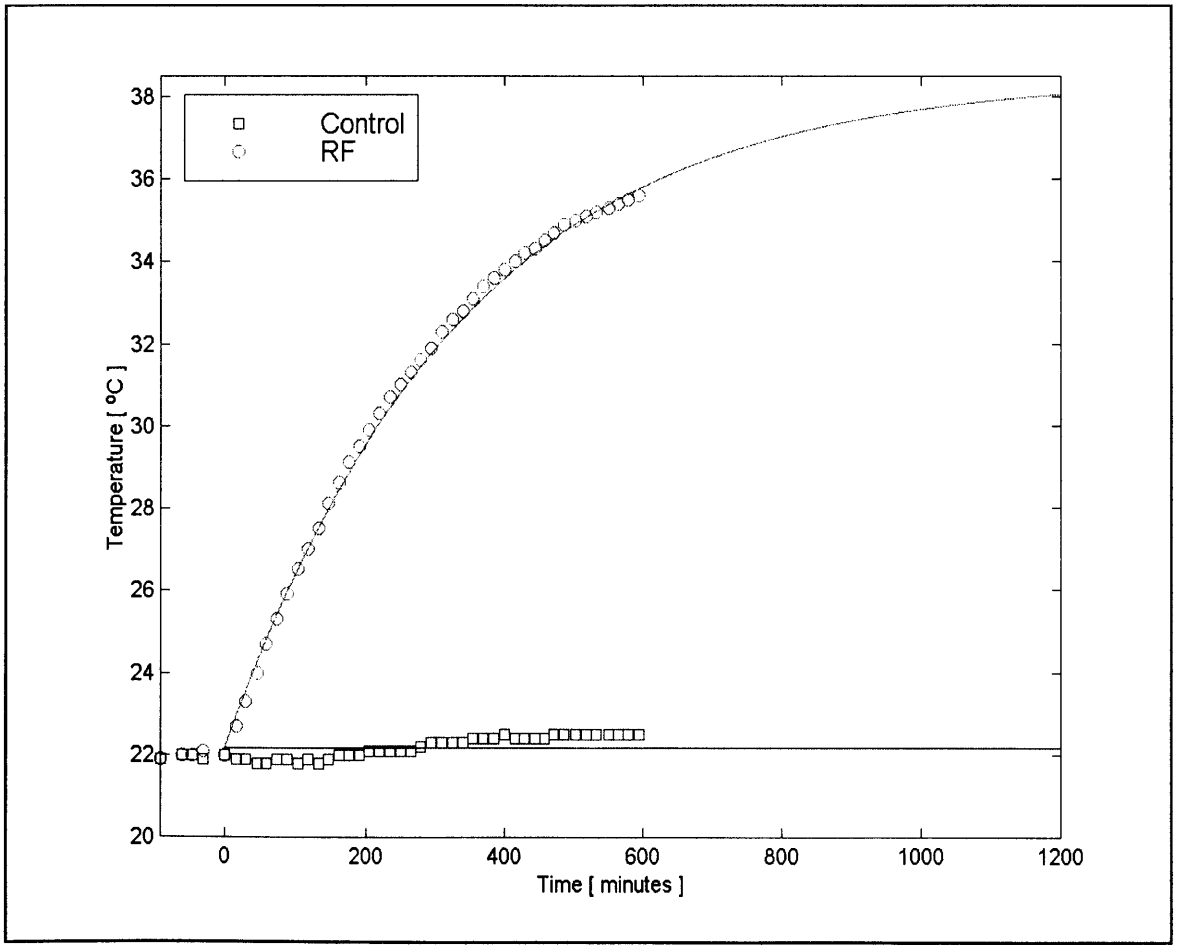

Figure 4-2: Steady State Temperature Measurements with REVOLT.
The temperature of two spherical phantoms was measured over a period of 11 hours. The flat solid line is the mean temperature of the control phantom over the entire 11 hours. The exponential growing curve was determined by non-linear fitting the data to Equation 4.13 with the initial temperature, T_0, being the average temperature of the control phantom.

temperature during the ten hour experiment. The nonlinear fitting of the temperature data revealed that the steady state temperature, T_{∞}, of the phantom is 38.5 ± 0.25 degrees Centigrade. The temperature rate constant is 3.0e-3 ± 1.0e-4 per second. This results in a heat transfer coefficient of 6.3 ± 0.02 watts per Centigrade per meter squared.

4.5 Discussion

The theoretical estimates for the SAR reveal some important insights into the safety of REVOLT. The SAR deposited into the head is 0.6 Watts per kilogram, which is 5 times lower than the current guidelines established by the FDA for RF exposure. The FDA guidelines assume that as a result of blood circulation, the RF power deposited is distributed evenly throughout the patient. To account for the body acting as a heat sink, the SAR is scaled by the ratio of the mass of the patient's head to the entire mass of the patient. This reduces the SAR 20 times for the average human. (The mass of the average human head body was assumed to be 3.5 kilograms and 70 kilograms, respectively). With this assumption the $SAR_{avg,head}$ is reduced to .03 Watts per kilogram, which is two orders of magnitude below the FDA's guidelines.

The torso SAR does not provide the same margin of safety. The length of the body coil contained in the GE Signa system is approximately 110 centimeters. The height of a standard human is 152 centimeters. The $SAR_{avg,torso}$ should be about 72% lower than was previously calculated or 1.4 Watts per kilogram. While this amount of RF power deposited into the patient is acceptable, it does not provide an adequate margin of safety. For this reason, we have restricted the use of the REVOLT sequence to the head coil and extremity coil configuration. This has significant implications in terms of sensitivity.

We have elected to use volume coil excitation instead of a surface coil to ensure uniform flip angles over the volume of interest and for easy volume localization. Volume coils, however, do not have the sensitivity that surface coils have when receiving the signal. The ideal coil configuration would be a volume coil excitation with a surface coil receive. The GE Signa is capable of achieving this hardware configuration using the body coil for excitation and a surface coil to receive the signal. Because of SAR

restrictions using the body coil for excitation, this coil configuration has not been used with REVOLT even though sensitivity improvements are expected.

Comparing REVOLT to a 2D FSE reveals that the SAR of REVOLT is less than the SAR of FSE. This comparison is compelling evidence that REVOLT is safe since FSE is a pulse sequence that is commonly used in standard clinical imaging. Figure 4-1 plots the temperature versus time of both saline phantoms for FSE and REVOLT. The apparent temperature increase in both experiments is a result of a small increase in the bore temperature.

To accurately determine the SAR deposited by REVOLT a similar experiment was conducted with a SAR 6.5 times greater than the current experiment. These empirical temperature measurements reveal a SAR_{avg} of 3.5 watts per kilogram. Bottomley's equation for the SAR of a sphere predicts a SAR of 3.6 watts per kilogram. The empirical average SAR and theoretical average SAR agree well. This agreement allows us to safely use Bottomley's equations to estimate the SAR.

4.6 Conclusion

The safety of REVOLT has been demonstrated both theoretically and empirically. Temperature measurements in a spherical phantom have shown the validity of Bottomley's SAR equations. These equations have revealed that REVOLT has an average SAR for a sphere of 0.6 Watts per kilogram, which is 46 percent less than a standard FSE imaging sequence. The average SAR deposited into a person with the quadrature head coil, accounting for the effective mass of the person, is two orders of magnitude below the guidelines established by the FDA. This margin of safety proves that REVOLT is not only safe for research but also for potential clinical applications when small volume coils are used for excitation.

Chapter 5 : Recommendations & Future Clinical Directions

5.1 Recommendations

Poor sensitivity, limited resolution, and resonance overlap restrict 1D *in vivo* NMR spectroscopy from quantitating all but the simplest resonances: NAA, choline, and creatine. Prior to REVOLT, 2D NMR experiments lacked the resolution and sensitivity necessary for clinical applications. With the development of REVOLT, sensitivity has been improved by a factor of 20 while removing the dispersive line shape. REVOLT is currently able to detect millimolar concentrations of GABA *in vivo* in 23 minutes from a 59-milliliter volume while adhering to FDA guidelines on RF power deposition. The resolution and sensitivity achieved by REVOLT, while unprecedented for 2D *in vivo* spectroscopy, are still insufficient for most clinical problems. This may change with improvements in hardware, volume localization, and post processing. With these improvements, REVOLT may move from a clinical novelty to a powerful diagnostic tool.

Increasing the magnetic field strength will improve the sensitivity. Theoretical calculations and empirical measurements reveal that REVOLT deposits one hundredth of the RF power allowed by the FDA. Since the RF power deposited scales as the square of the magnetic field strength, REVOLT may be used on a 3 Tesla scanner without violating RF power deposition guidelines. Assuming that the SNR is proportional to the ratio of magnetic field strengths raised to the 3/2 power (46), REVOLT's sensitivity would improve by a factor of 3. Higher field strength would not only improve sensitivity but would also increase the range of chemical shift dispersion. However, magnetic susceptibility line broadening depending on the tissue geometry is expected to increase with magnetic field strength, which would result in a loss in resolution. Only future experiments will reveal under what conditions and increase in the magnetic field strength is favorable for *in vivo* spectroscopy.

Volume coil excitation offers the greatest flip angle uniformity and flexibility in volume localization. The use of small volume coils, such as the head coil, also limit the

amount of RF power deposited in the patient. While volume coils have these advantages, they do not have the same sensitivity as surface coils when receiving the signal. The optimum coil configuration for all *in vivo* spectroscopy experiments is volume coil excitation with a surface coil receive. Imaging experiments using a surface coil to both transmit and receive showed that the SNR could be improved by a factor of 10 near the brain's surface (47) when compared to images acquired with a quadrature head coil. The sensitivity improvement decreased with depth, such that, at 9 centimeters from the coil, there was no improvement in the SNR. A weighted average reveals that the SNR would improve by a factor of 4.

Increasing the sensitivity may also be achieved by improving the method of volume localization. Currently, REVOLT achieves volume localization with PRESS. This restricts the volume of interest to a cube. In order to avoid partial volume effects, the cube must be contained entirely in the tissue or pathology of interest. A cubic volume severely limits the amount of potential signal. Incorporating methods for arbitrary volume localization, such as outer volume suppression (48-50), has the potential of improving sensitivity. For instance, let us assume that the pathology of interest has a spherical geometry. A cubic volume only acquires signal from 67 percent of the pathology. Acquiring signal from the spherical tumor would result in a 33 percent increase in the SNR.

REVOLT was developed on a standard 1.5 Tesla clinical scanner. The scanner was equipped with 1 Gauss per centimeter gradients with a maximum slew rate of 500 microseconds. In order to suppress unwanted signals adequately, each transverse crusher gradient had a total pulse width of 3 milliseconds. Doubling the maximum gradient strength while decreasing the slew rate by a factor of two would decrease the time between the third $\pi/2$ pulse and acquisition by 25 percent. A back of the envelope calculation predicts that a 25 percent reduction in the transverse time can lead to a 6 percent improvement in the SNR for metabolites with short T_2 (i.e. 100 ms).

Combining the sensitivity improvements achieved with improved gradients, a larger magnetic field, and outer volume suppression, the SNR could be improved up to a factor of 17, which would directly translate into an increase in detectability and improved quantitation. In addition, it may now be possible to see the α and β correlations of

glucose. However, while this sensitivity improvement is impressive and necessary, for REVOLT to be used in a clinical setting, further improvement in sensitivity and detectability can be obtained with post-processing.

Data processing methods that rely on the Fourier transform are not optimum for processing *in vivo* spectroscopy data since they do not bias the data based upon available prior knowledge. The interpretation of the human brain spectra incorporated prior knowledge by comparing the spectra to a phantom containing similar metabolites. This comparison helped to distinguish cross correlation peaks from t_1 noise and truncation artifacts. Incorporating this type of prior knowledge into the post-processing should offer significant sensitivity advantages over a simple 2D Fourier Transform data. Such methods are starting to appear in the 1D spectroscopy literature (51,52) with some success.

5.2 Future Clinical Directions

Proton NMR spectroscopy has long been applied to the study of human brain. The major metabolites such as GABA, glutamate, glutamine, lactate and NAA have all been utilized to study congenital and acquired diseases involving the mood, neoplasia, cerebrovascular disease and infection, just to name a few. Of the major brain metabolites, GABA has the widest role as a physiological modulator. This is due to its function as an inhibitory neurotransmitter. Alterations in its concentration have been implicated in the seizure disorders (38) and the pathogenesis of bipolar (manic) depression (39,40). Only recently have editing techniques been proposed to allow unambiguous measurement of GABA in the human brain (37).

5.2.1 Mood Disorders

It has long been hypothesized that GABA plays a role in the modulation of mood since GABA ergic tone inhibits metabolism of norepinephrine and serotonin (39), both of which are pharmacologically manipulated in conventional anti-depressive therapy. In addition, low plasma GABA levels have been shown to correlate with the presence of

bipolar disorder (38). It has been proposed that the measure of plasma GABA levels could form the basis of a screening test for populations at risk for mood disorder based on family history (53). One curiosity is the relative lack of change in plasma GABA levels when GABA agonists are used with success to treat mood disorders (54). Several avenues of investigation become apparent.

It would be quite valuable to measure the GABA concentration in human brain within populations at risk for, or suffering from, mood disorders. Correlation of brain and plasma levels in these patients would help to support or refute the hypotheses put forth regarding measurement of plasma GABA levels. As the successful pharmacologic therapy of mood disorders does not appear to normalize plasma GABA in most cases, it would be of great interest to follow the brain GABA levels in these patients. The ability to unambiguously measure GABA with the REVOLT experiment, simultaneously with the other major metabolites makes such studies now possible on widely available clinical imaging systems.

5.2.2 Seizure

As pointed out in a recent review, seizure is the most common complication of low-grade glioma (55). In addition, high levels of glycine, serine and ethanolamine have been identified in the periphery of cerebral cavernous angiomata (56). These are benign vascular lesions with a high rate of seizure. It has been shown that the seizure disorder abates following removal of the angiomata, and it has been postulated that the elevated levels of serine, glycine and ethanolamine may mediate the seizure due to NMDA receptor activation and/or alteration of the blood-brain barrier. In the non-neoplastic seizure, vigabatrin, a GABA analogue, has been shown to have a significant anti-epileptic effect in infants (57).

Due to the ability to assign the coupling networks of spin systems such as found in the amino acids, REVOLT would be a powerful tool for investigation of brain metabolite levels in the neoplastic or non-neoplastic setting. The ability to measure GABA within a low grade glioma might lead to support for therapy with vigabatrin in this population.

5.2.3 Osteomyelitis

Infection of the bone, or osteomyelitis, remains a common and difficult clinical problem among all ages (58), particularly in the diabetic population (59). The most common approach to diagnosis of this disorder is performance of radiographs, ^{99m}Tc-methylenediphosphante, ^{67}Ga and ^{99m} Tc-DTPA (diethylenetriamine pentaacetic acid) labeled white blood cell scintigraphy, or MRI (60). With such a battery of tests available, the correct diagnosis of osteomyelitis can remain difficult. This is due to the length of time required for radiographic evidence to develop (7-10 days), and the lack of specificity of increased radiopharmaceutical deposition in bone. While promising, the role of MRI is still debated. Recent clinical publications demonstrate that the presence of bone marrow edema, quite pronounced on inversion recovery images of infected bone, is also part and parcel of any abnormality of bone marrow (61). These include stress-related increases in blood flow due to soft tissue injury, fracture, abnormal weight bearing or neoplasm. In particular, the neuropathy of the diabetic foot, resulting in loss of sensation, allows repeated injury to the diabetic foot to go unnoticed by the patient. Such patients, also at high risk for osteomyelitis due to chronic hypoperfusion related skin ulcers, often present with a markedly abnormal radiograph due to healing fractures. These fractures mimic the radiographic findings of osteomyelitis: soft-tissue swelling, decreased bone mineralization and periosteal new bone formation.

The lack of specificity of these methods raises the possibility that MR spectroscopy could play a key role in diagnosis of osteomyelitis. To date, such a study has not been reported. There are, however, a few publications demonstrating the utility of MR spectroscopy in human brain abscesses *in vivo* (62-64). It has been shown that the PRESS and STEAM spectra of human brain abscesses demonstrate the presence of high levels of acetate both *in vivo* and *ex vivo*. In addition, one report showed that several amino acids could be identified in brain abscesses, not present in cystic neoplasms (65). The proof of the assignment of the 1.92 ppm methyl peak to acetate and the unusual amino acid resonances required the performance of 2D COSY experiments in this study.

Because of the apparent specificity of the spectral findings in brain abscesses, it seems reasonable to pursue the application of MR spectroscopy to the diagnosis of osteomyelitis. One of the imaging findings in osteomyelitis is the presence of an

enhancing soft tissue rind surrounding the osseous abscess cavity (66). This "penumbra sign" represents highly vascular granulation tissue surrounding the area of dead bone and abscess. The fact that a non-enhancing central area of fluid and necrotic bone is present histologically, allows the possibility of MR spectroscopic evaluation of this fluid for the characteristic infection related resonances. The use of REVOLT type experiments would allow the assignment of the amino acid resonances in an unambiguous manner, obviating the need for *ex vivo* spectroscopy.

References

1 J. Frahm, H. Bruhn, M.L. Gyngell, K.D. Merboldt, W. Hanicke, R. Sauter, "Localized proton NMR spectroscopy in different regions of the human brain: relaxation times and concentrations of cerebral metabolites." Magn Reson. Med. 11:47-63 (1989).

2 I.J. Cox, "Development and Applications of In Vivo Clinical Magnetic Resonance Spectroscopy". *Prog. Biophys. Molec. Bio.* **65**:45-81 (1996)

3 A.A Tzika, W.S. Ball, D.B. Vigneron, R.S. Dunn, D.R. Kirks, "Clinical Proton Spectroscopy of Neurodegenerative Disease in Childhood". *AJNR* **14**:1267-1281 (1993)

4 R.A. Zimmerman, J. Valk, Z. Wang, Commentary, "Clinical Proton MR Spectroscopy of Neurodegenerative Disease in Childhood". *AJNR* **14**:1282-1284 (1993).

5 O.W. Sorenson, M.H. Levitt, R.R Ernst, *J. Mag. Reson.* **55**:104 (1983)

6 J. Jeener, Ampere International Summer School, Basko Polje, Yugoslavia (1971), unpublished lecture.

7 J. Briand and R.R. Ernst, "Sensitivity Comparison of Two-Dimensional Correlation Spectroscopy in the Laboratory Frame and in the Rotating Frame". *J. Mag. Res. A* 104:54-62 (1993)

8 I. M. Brereton, G.J. Galloway, S.E. Rose, D.M. Doddrell, "Localized Two-Dimensional Shift Correlated Spectroscopy in Humans at 2 Tesla". *Magn. Reson. Med.* 32:251-257 (1994)

9 http://www.fda.gov/cdrh/ode/magdev.html. (10/31/98).

10 W.P. Aue, E. Bartholdi, R.R. Ernst, "Two-Dimensional Spectroscopy: Application to Nuclear Magnetic Resonance", *J. Chem. Phys.* **64**: 2229-2246 (1976).

11 A. Bax, R. Freeman, "Investigation of Complex Networks of Spin-Spin Coupling by Two-Dimensional NMR". *J. Magn. Reson.* 44, 542-561 (1981).

12 L. Braunscheweiler, R.R. Ernst, "Coherence Transfer by Isotropic Mixing: Application to Proton Correlation Spectroscopy". *J. Magn. Reson.* **53**:521-528 (1983)

13 D.G. Davis, A. Bax, "Assignment of Complex Proton Spectra via Two-Dimensional Homonuclear Hartmann-Hahn Spectroscopy". *J. Am. Chem. Soc.* **107**:2820-2821 (1985)

14 J. Briand, R.R. Ernst, "Sensitivity Comparison of Two-Dimensional Correlation Spectroscopy in the Laboratory Frame and in the Rotating Frame". *J. Magn. Reson. A.* **104**:54-62 (1993)

15 J. Frahm, H, Bruhn, M.L. Gnygell, K.D. Merbolt, W. Hanicke, R. Sauter, "Localized High-Resolution Proton NMR Spectroscopy using Stimulated Echoes: Initial Application to Human Brain In Vivo". *Magn. Reson. Med.* **9**:79-93 (1989)

16 C.T.W. Moonen, P.C.M van Zijl, "Highly Effective Water Suppression for in Vivo Proton NMR Spectroscopy (DRYSTEAM)". *J. Magn. Reson.* **88**:28-41 (1990).

17 R. E. Hurd "Gradient Enhanced Spectroscopy", *J. Magn. Reson.* **87**:422-428 (1990)

18 M. Rance, "Improved Techniques for Homonuclear Rotating-Frame and Isotropic Mixing Experiments". *J. Magn. Reson.* **74**:557-564 (1987).

19 R. Bazzo, I.D. Campbell, "Pure-Phase 2D Homonuclear Cross-Polarization Spectroscopy in Liquids". *J. Magn. Reson.* **76**:358-361 (1988).

20 A. Haase, J. Frahm, W. Haenicke, and D. Matthei, *Phys. Med. Bio.*. **30**: 341 (1985)

21 O.W. Sorensen, G.W. Eich, M.H. Levitt, G. Bodenhausen, R.R. Ernst, "Product Operator Formalism for the Description of NMR Pulse Experiments". *Progr. Nucl. Magn. Reson. Spectrosc.* **16**:163-192 (1983).

22 R.R. Ernst, G. Bodenhausen, A. Wokaun, "Principles of Nuclear Magnetic Resonance in One and Two Dimensions", Oxford Science Publications, Clarendon Press, 1987.

23 A.Bax, A.F. Mehlkopf, J.Smidt, *J. Magn. Reson.* **35**:373 (1979)

24 A.Bax, R.Freeman , G.A. Morris, *J. Magn Reson.* **43**:333 (1981).

25 A. Bax, "Two-Dimensional Nuclear Magnetic Resonance in Liquids", Reidel Press, London, 1982.

26 J.C. Hoch, A.S.Stern, "NMR Data Processing", Wiley-Liss Inc. (1996)

27 C.J. Turner, H.D.W. Hill, "Artifacts in Quadrature Detection", *J. Magn. Reson.* **66**:410-421 1986.

28 G. Brix, S. Heiland, M.E. Bellemann, T. Koch, W.J. Lorenz, "MR Imaging of Fat Containing Tissues: Valuation of Two Quantitative Imaging Techniques in Comparison with Localized Proton Spectroscopy". *Magn. Reson. Imaging* **11**:977-991 (1993).

29 A. Mohebbhi, A.J. Shaka. "Improvements in carbon-13 broadband homonuclear cross-polarization for 2D NMR". *Chem. Phys. Lett.* **178**:374-378, (1991)

30 M. Kadkhodaie, M. Tan, O. Rivas, A. Mohebbi, and A.J. Shaka. "Broadband Homonuclear Cross Polarization Using Flip-Flop Spectroscopy". *J. Magn. Reson.* **91**:437-443 (1991)
31 D.J. States, R.A. Haberkorn, D.J. Ruben. "A Two-Dimensional Nuclear Overhauser Experiment with Pure Absorption Phase in Four Quadrants". J. Magn. Reson. **48**:286-292 (1982)
32 S. Macura, Y. Huang, D. Sutter, R.R. Ernst. J. Magn. Reson. **43**:259 (1981)
33 A.J. Shaka, J. Keeler, R. Freeman, "Evaluation of a New Broadband Decoupling Sequence: WALTZ-16. *J. Magn. Reson.* **53**:313-340 (1983)".
34 A. Bax , D.G. Davis, "MLEV-17 Based Mixing for Homonuclear Hartmann-Hahn Spectroscopy. *J. Magn. Reson.* **63**:207 (1985)"
35 H Shimizu, T Kumabe, T Tominga, "Non-invasive Evaluation of Maligancy of Brain Tumors with MR spectroscopy". *AJNR* **17:**737-747 (1996).
36 K. Kanamori and B.D. Ross. "Glial Alkalinization Detected in vivo by ^{1}H-15N HMQC Transfer NMR in Severely Hyperammonemic Rat". *ISMRM Abstract* 537, (1997).
37 J. R. Keltner, L. L. Wald, J.D.Christensen, L.C. Maas, C.M. Moore, B.M. Cohen, P.F. Renshaw, A "Technique for Detecting GABA in the Human Brain with PRESS Localization and Optimized Refocusing Spectral Editing Radiofrequency Pulses". *Magn. Reson. Med.* **36**:458-461 (1996)
38 J.S. Duncan "Imaging and epilepsy". Brain **20**:339-377 (1997).
39 I.S. Shiah, L.N. Yatham. "GABA function in mood disorders: an update and critical review". Life Sci. **63**:1289-1303 (1998).
40 F. Petty, "GABA and mood disorders: a brief review and hypothesis. J. Affect. Disord. **34**:275-281(1995).
41 A Bax, R.H. Griffey, B.L. Hawkins. "Correlation of Proton and Nitrogen-15 Chemical Shifts by Multiple-Quantum NMR". J. Magn. Reson. 55: 301-315 (1983).
42 P.A. Bottomley, W.A. Edelstein "Power Deposition in Whole-Body Imaging". *Med. Phys.* **8**:510-512 (1981)
43 P.A. Bottomley, R.W. Redington, W.A. Edelstein, J.F. Schenck, "Estimating Radiofrequency Power Deposition in Body NMR Imaging". *Magn. Reson. Med.* **2**:336-349 (1985)
44 M.N. Ozisik, "Heat Transfer: A Basic Approach" McGraw-Hill Publishing Company. (1985)
45 Press, W.H., B.P. Flannery, S.A. Teukolsky, W.T. Vetterling, Numerical Recipes in C, the Art of Scientific Computing. Cambridge University Press. (1988)
46 E. Fukushima, S. B.W. Roeder, Experimental Pulse NMR: A Nuts and Bolts Approach. Addison-Wesley Publishing Company (1981)
47 S.E. Moyers, D.B. Vigneron, S.J. Nelson, "Surface Coil MR Imaging of the Human Brain with an Analytical Profile Correction". *JMRI* **5**:139-144 (1995)
48 S. Singh, B.K. Rutt, "Projection Presaturation: A Fast and Accurate Technique for Multidimensional Spatial Localization". *J. Magn. Reson.* **87**:567-583 (1990)
49 S. Singh, B.K. Rutt, S. Napel, "Projection Presaturation II: Single-Shot Localization of Multiple Regions of Interest". *J. Magn. Reson.* **90**:313-329 (1990)
50 S. Singh, W.R. Brody, "Projection Presaturation III: Accurate Selective Excitation or Presaturation of the Regions of Tailored Shape in the Presence of Short-T_1 Species". *J. Magn. Reson. B.* **101**:52-62 (1993)
51 H. Chen, S. van Huffel, D. van Ormondt, R. de Beer, "Parameter Estimation with Prior Knowledge of Known Signal Poles for the Quantification of NMR Spectroscopy Data in the Time Domain." *J. Magn. Reson. A.* **119**:225-234 (1991).
52 G.L. Bretthorst. "Lecture Note in Statistics: Bayesian Spectrum Analysis and Parameter Estimation", Vol. 48. Springer-Berlag. (1988)
53 F. Petty, "Plasma concentrations of gamma-aminobutyric acid (GABA) and mood disorders: a blood test for manic depressive disease?" *Clin. Chem.* **40**:296-302 (1994).
54 J. Prosser, C.W. Hughes, S. Sheikha, R.A. Kowatch. "Plasma GABA in children and adolescents with mood, behavior, and comorbid mood and behavior disorders: a preliminary study." *J. Child Adolesc. Psychopharmacol.* 7:181-199 (1997).
55 P.C. Warnke, A. Berlis, A. Weyerbrock, C. Ostertag. "Significant reduction of seizure incidence and increase of benzodiazepine receptor density after interstitial radiosurgery in low-grade gliomas." *Acta Neurochir. Suppl.* **68**:90-92 (1997).

56 J. Aicardi, J.P. Mumford, C. Dumas, S. Wood. "Vigabatrin as initial therapy for infantile spasms: a European retrospective survey." *Epilepsia* **37**:638-642 (1996).
57 C. von Essen, B. Rydenhag, B. Nystrom, R. Mozzi, N. van Gelder, A. Hamberger. "High levels of glycine and serine as a cause of the seizure symptoms of cavernous angiomas?" *J. Neurochem.* **67**:260-264 (1996).
58 M.P. Hauer, M. Uhl, K.H. Allmann, J. Laubenberger, L.B. Zimmerhackl, M. Langer. "Comparison of turbo inversion recovery magnitude (TIRM) with T2-weighted turbo spin-echo and T1-weighted spin-echo MR imaging in the early diagnosis of acute osteomyelitis in children." *Pediatr. Radiol.* **28**:846-850. (1998)
59 W.B. Morrison, M.F. Schweitzer, W.G. Batte, D.P. Radack, K.M. Russel. "Osteomyelitis of the foot: relative importance of primary and secondary MR imaging signs." *Radiology* **207**:625-632 (1998).
60 L.J. Abernethy, H. Carty. "Modern approach to the diagnosis of osteomyelitis in children." *Br. J. Hosp. Med.* **58**:464-468 (1997).
61 M. Wingen, G. Alzen, R.W. Gunther. "MR imaging fails to detect bone marrow oedema in osteomyelitis: report of two cases." *Pediatr. Radiol.* **28**:189-192 (1998).
62 M. Harada, M. Tanouchi, H. Miyoshi, H. Nishitani, S. Kannuki. "Brain abscess observed by localized proton magnetic resonance spectroscopy." *Magn. Reson. Imaging* **12**:1269-1274 (1994).
63 H. Poptani, R.K. Gupta, V.K. Jain, R. Roy, R. Pandey. "Cystic intracranial mass lesions: possible role of in vivo MR spectroscopy in its differential diagnosis." *Magn. Reson. Imaging* **13**:1019-1029 (1995).
64 I. Martinez-Perez, A. Moreno, J. Alonso, J. Aguas, G. Conesa, A. Capdevila, C. Arus. "Diagnosis of brain abscess by magnetic resonance spectroscopy. Report of two cases." *J. Neurosurg.* **86**:708-713 (1997).
65 C. Remy, S. Grand, E.S. Lai, V. Belle, D. Hoffmann, F. Berger, F. Esteve, A. Ziegler, J.F. Le Bas, A.L. Benabid. "1H MRS of human brain abscesses in vivo and in vitro." *Magn. Reson. Med.* **34**:508-514 (1995).
66 A.C. Grey, A.M. Davies, D.C. Mangham, R.J. Grimer, D.A. Ritchie. "The 'penumbra sign' on T1-weighted MR imaging in subacute osteomyelitis: frequency, cause and significance." *Clin. Radiol.* **53**:587-592 (1998).